A Comparison of the Planforms of Meandering Tidal and Fluvial Channels on the Ganges-Brahmaputra-Jamuna Delta, Bangladesh

A THESIS SUBMITTED TO THE
FACULTY OF THE UNIVERSITY OF MINNESOTA BY

Rachel Louise Bain

IN PARTIAL FULFILMENT OF THE REQUIREMENTS
FOR THE DEGREE OF MASTER OF SCIENCE

Advisor: Dr. Chris Paola

August 2014

Acknowledgements

I would like to express my sincere thanks to the following individuals, who provided the ideas and resources necessary for the completion of this thesis:

- To my research advisor Dr. Chris Paola, for insightful conversations about my project and for answering so many "silly" questions;
- To Dr. Justin Revenaugh and Dr. Vaughan Voller, for serving on my thesis committee;
- To Dr. Paola Passalacqua (University of Texas at Austin), Dr. Steve Goodbred (Vanderbilt University), Dr. Stefano Lanzoni (University of Padova, Italy), and Dr. Efi Foufoula-Georgiou, for extremely helpful discussions and insight into the ideas presented in this thesis;
- To the individuals at St. Anthony Falls Laboratory who listened to my ideas, made suggestions, and asked the hard questions (in alphabetical order): Antoinette Abeyta, Sarah Baumgardner, Dan Cazanacli, Nic Evans, Temilola Famakinwa, Dr. Brady Foreman, Dr. Vamsi Ganti, Jon Schwenk, Dr. Arvind Singh, and Dr. Wei Zhang;
- To Molly Wynia, University of Minnesota USpatial Center, for assistance with ArcGIS questions;
- To Dana Peterson, University of Minnesota Borchert Map Library, for locating obscure maps of Bangladesh for my research.

I also wish to express my personal gratitude to the following:

- To Dad, Mom, Tim, Rebekah, and David, for their love, support, and encouragement, and for never letting me take life too seriously;

- To Lynn, for her constant friendship and support in spite of my tendency to disappear into the deep recesses of research for months at a time. Who could have guessed that our childhood predictions about Bangladesh would turn out to be so accurate?

- To the faculty at the University of Wyoming, in particular my undergraduate advisor Dr. John Kaszuba, for encouraging me to pursue a graduate degree and giving me the academic skills necessary to do so.

Contents

List of Tables

List of Figures

Chapter 1

Introduction and literature review

Tidal environments are very often characterized by the presence of channels. Although these channels may display any of several forms–straight or meandering, isolated channels or complex networks (*e.g.*, Eisma, 1998)–they are unified by their interaction with bidirectional flow. As the process controlling their morphology is fundamentally different from that of an alluvial river, one might expect tidal channels to display a distinct geometry relative to their fluvial counterparts. Indeed, consider the following observations from previous studies:

> Intertidal channels are different from other types because they serve as both arteries and veins: guiding semidiurnal flood tidal flows onto the moist tidal flats, and channeling the receding waters during the ebb tide. Thus the student of natural channels appreciates the fact that results based on tidal flat channels will not have complete applicability to non-tidal channels developed on similar substrates (Bridges and Leeder, 1976).
>
> While the regularity of meandering channels might argue otherwise, there is no reason to expect that the same [wavelength] selection mechanism necessarily operates in all channels. Clearly, if bars are not present in the channel as in tidal marshes or mud flats, some mechanism other than bars must be operating (Whiting and Dietrich, 1993).
>
> Bidirectional flow is thus a unique characteristic of tidal channels distinct from terrestrial rivers (Fagherazzi *et al.*, 2004).

Yet we wonder, what, if anything, sets the geometry of tidal channels apart from the geometry of rivers? Although the controlling processes are different, is there anything truly distinct about a tidal channel's shape?

This is hardly a new question. In 1927, Campbell suggested that tidally-influenced rivers are "inert"; that is, the channel "has no inclination to form meanders and none to cut off meanders already formed" (p. 542). By Campbell's reasoning, the tidal prism behaves as a buffer that prevents the thalweg from contacting the banks and initiating the lateral erosion required for meandering. Meanders observed in tidal zones would therefore be evidence of relative sea-level rise along a previously non-tidal river. Barton (1928) disagreed with Campbell, citing the contemporary lateral migration of a tidally-influenced meander in the Brazos River, Texas. Johnson (1929) likewise disputed Campbell's claim based on questionable methods and vague terminology. Given the ninety-year time span since the inception of this question, coupled with the morphodynamics community's interest in the general question of meandering, it is surprising how few authors have quantitatively addressed the possible existence of differences in tidal and fluvial meander morphologies. In this chapter, we summarize the current state of knowledge regarding the general process of meandering. We then outline previous research comparing tidal and fluvial meanders, and address several other ways in which tidal and fluvial channels may differ.

1.1 General perspectives on meandering

The regular patterns displayed by meandering channels have long captured humankind's attention. Indeed, some of history's greatest thinkers—Leonardo da Vinci and Albert Einstein being two of the most famous—sought to address the question of why rivers meander (Baker, 2013). But despite existence of a large body of literature on the physics of meandering (see Camporeale *et al.*, 2007; Güneralp and Marston, 2012), the nuances of this problem are still actively being addressed as researchers seek to fully comprehend and predict the behavior of meandering channels.

Theoretical models of river meanders fall into two distinct categories: physical and geometrical. Physical models seek to predict meander form and evolution based on solutions to the equations governing open-channel flow and relevant sedimentary processes. In contrast, the goal of geometrical models is to reproduce the observed planform characteristics

of natural channels from either a deterministic or a stochastic perspective (Camporeale *et al.*, 2007; personal communication with E. Foufoula-Georgiou, March 2014). This does not imply that geometrical models are entirely decoupled from physical explanation; however, the relevant physical processes are considered only after successful reproduction of the observed geometrical properties of the channel.

1.1.1 Physical models of meandering

As summarized by Solari *et al.* (2002), research in stream hydraulics has put forth two theories regarding the physics of meander formation: bar theory and bend theory. Although the basic principles of bar theory can be traced back to field work by Matthes (1941) and experiments by Quraishy (1944) and Friedkin (1945; see also Leopold and Wolman, 1960, or Leopold *et al.*, 1964, p. 301-308), Solari *et al.* (2002) attribute the theory itself to the work of Leopold and Wolman (1957). These authors noted that straight river channels often contain a wandering thalweg that deposits alternating bank-attached bars similar to those found in meandering channels. This led to two key observations concerning straight channels: (1) the repeat distance between bars on the same bank of a straight channel is seven to fifteen times the width of the channel, the same as the straight-line (*i.e.*, Cartesian) wavelength of a meandering channel; and (2) straight channels can occur at the low bed slopes associated with meandering channels, whereas braided channels occur only at higher slopes. These two observations led to the conclusion that the mechanics of meandering also operates in straight channels. The idea that alternate bars in a straight channel are the precursors of meanders is still widely accepted (*e.g.*, Parker, 2004, Chapter 8).

Bend theory is rooted in the work of Ikeda *et al.* (1981) and has the basic assumption that meandering is a product of the steady flow perturbations resulting from channel curvature (Solari *et al.*, 2002). That is, whereas in bar theory the position of the alternating bars within the channel is not fixed, in bend theory the location of the bars is determined by the curvature of the channel (Ikeda *et al.*, 1981). Representing the channel as a function in

two-dimensional space, the authors give the equation of the channel centerline as

$$y = \varepsilon e^{\alpha_0 t} \cos(kx - \omega_0 t) \tag{1.1}$$

where x is distance along the valley centerline, y is perpendicular, signed distance from the valley centerline to the channel at time t, ε is the initial meander amplitude, k is the wavenumber, and ω_0 is the dimensionless migration frequency. The parameter α_0 is the dimensionless amplitude growth-rate, given by

$$\alpha_0 = \frac{2C_f^2(A + F^2)k^2 - k^4}{k^2 + 4C_f^2} \tag{1.2}$$

where C_f is an approximately constant friction factor, $A = 2.89$ is a parameter determined from field data, and F is the Frounde number. Noting that the meanders will grow in amplitude (*i.e.*, erosion will occur) if $\alpha > 0$, the authors conclude that the position of the channel is unstable for any wavenumber $k < \sqrt{2}C_f(A + F^2)^{1/2}$. Moreover, finding the value of k for which $\partial\alpha/\partial k = 0$ suggests that the dominant wavenumber for channel meandering is given by $k_{OM} = C_f F$.

Bar theory and bend theory predict meander wavelengths of the same order of magnitude (Ikeda *et al.*, 1981), suggesting that the two ideas may be interrelated. Indeed, Blondeaux and Seminara (1985) proposed a theory of meander formation integrating aspects of both the bar and the bend mechanisms. This new theory suggests that a meandering channel of given Shields parameter θ and nondimensional sediment diameter[1] d_s possesses a resonant frequency given by a critical wavenumber and width ratio. From the perspective of bend theory, the resonant frequency controls the curvature-driven erosion and deposition that leads to bend amplification, while a completely different mechanism, instability, controls the alternate-bar formation central to bar theory. However, the two are related in that the preferred wavelength of amplification is selected from the alternate-bar wavelengths. Simply stated, "the bend approach may be considered just a particular case of the bar approach"

[1]The nondimensional sediment diameter is given by $d_s = d_s^*/D_0^*$, where d_s^* is the characteristic sediment size and D_0^* is the average depth of the uniform unperturbed flow.

(Solari *et al.*, 2002, p. 206).

Following the development of bend theory, two models served as "key steps" (Camporeale *et al.*, 2007) towards the modern understanding of meander dynamics. The first is the model by Johannesson and Parker (1989). These authors improved on the work of Ikeda *et al.* (1981) by coupling the flow field, the bedload transport, and bed topography. Including an erodible bed in their model allowed Johannesson and Parker (1989) to simulate oversteepening phenomena, where the lateral bed slope upstream of a bend is much higher than predicted, and show that oversteepening is linked to the resonance observed by Blondeaux and Seminara (1985). The second key step towards modern meander theory is the model by Zolezzi and Seminara (2001), which addresses the behavior of bedforms and channel depth in sub- and super-resonant channel configurations. Whereas previous models suggest that a channel only "feels" the effect of a curvature downstream of the curved reach, these authors demonstrate that perturbations to bed topography resulting from channel curvature can propagate upstream under super-resonant conditions. The geomorphological implication of this result is that sub-resonant meanders should be downstream skewed, while super-resonant meanders should be upstream skewed. For further details on the progression of research that led to the development of modern meander theory, the reader is referred to the review articles by Camporeale *et al.* (2007), Güneralp and Marston (2012), and Güneralp *et al.* (2012).

Researchers now recognize that there are four key processes that must be incorporated into any physical model of meandering: flow-field hydrodynamics, sediment transport, bed morphodynamics, and bank erosion (Motta *et al.*, 2012b). Such modeling may be extremely complex and computationally intensive due to feedbacks between these processes. Consequently, many modern studies emphasize the role of a subset of these processes while making simplifying assumptions regarding the others. For example, Motta *et al.* (2012b) decouple hydrodynamics and sediment transport and ignore the effect of secondary flow on momentum, instead focusing on how episodic bank failure processes affect meander evolution. In a subsequent paper, the same authors address the effects of soil heterogeneity on meander planforms (Motta *et al.*, 2012a). The output from these models contrasts significantly with

the output from the model by Ikeda *et al.* (1981), which makes the simplifying assumption that the bank erosion rate is proportional to the local excess velocity. Another example is the work of Abad *et al.* (2013) in which the shape of the meanders was fixed (*i.e.*, no bank erosion) in order to emphasize the effect of bedform development on channel hydrodynamics.

1.1.2 Geometrical models of meandering

Early geometrical models of meanders sought to reproduce observed channel geometries from a deterministic perspective. The first such model is the sine-generated curve, which was introduced by Langbein and Leopold (1966; see also Leopold and Langbein, 1966). A sine-generated curve is a parametric curve in two-dimensional space defined by its direction function:

$$\theta = \omega \sin \frac{2\pi s}{L_f} \tag{1.3}$$

where θ is the angle the curve makes with the x-axis at an arc-length t along the meander, ω is the maximum angle of deviation from the x-axis, and L_f is the total arc-length of one meander. Alternatively, the curve may be defined in terms of its curvature function

$$\kappa(s) = \frac{d\theta}{ds} = \frac{2\pi\omega}{L_f} \cos \frac{2\pi s}{L_f}. \tag{1.4}$$

Sine-generated curves have the property of exhibiting the smallest total change in direction (*i.e.*, the smallest value of $\sum \frac{(\Delta\theta)^2}{\Delta s}$) compared to any other curve of the same arc-length L between the same two points[2]. Langbein and Leopold (1966) propose that this reflects a channel's "desire" to uniformly distribute energy losses over the entire reach. Physical explanation notwithstanding, the authors note several examples in which the sine-generated curve provides a very good approximation to the observed shape of natural meandering channels.

Symmetry is a fundamental property of the basic sine-generated curve (*e.g.*, see upper left frame of Figure 1.1). Indeed, each half-meander of a sine-generated curve is bilater-

[2]We discuss additional mathematical properties of the sine-generated curve in an appendix to this document.

ally symmetrical, and the full-meander possesses a twofold radial symmetry about its central inflection point. In contrast, many natural meanders are skewed in a systematic manner, suggesting that the always-symmetrical sine-generated curve may not be the best representation of their planform geometry. To compensate for a meander's natural asymmetry, subsequent geometric models adopt the use of the Kinoshita curve, which modifies the standard sine-generated curve by through the superimposition of higher-frequency direction changes. The Kinoshita equation (*e.g.*, Parker *et al.*, 1983; Marani *et al.*, 2002) may be expressed as

$$\kappa(s) = C_0 \left[\cos\left(\frac{2\pi s}{L_f}\right) - C_F \cos\left(3\frac{2\pi s}{L_f}\right) - C_S \sin\left(3\frac{2\pi s}{L_f}\right) \right] \tag{1.5}$$

where C_F and C_S are the fattening and skewness coefficients and C_0 is the maximum curvature if $C_F = C_S = 0$. Given the curvature, we can produce the channel's planform for varying values of C_F and C_S using the sine-generated curve properties discussed in the appendix. For a constant intrinsic meander length, increasing the fattening coefficient produces wider meanders with a smaller amplitude relative to the valley centerline, whereas increasing the skewness coefficient shifts the apex of each half-meander upstream (Figure 1.1).

In contrast to these purely deterministic models of meandering, other authors have turned to stochastic models as a means of producing meander geometries. Thakur and Scheidegger (1970) devised a creative analogue for addressing the stochastic meander problem: a commonplace necklace chain. The authors attached both ends of the chain to a flat board a fixed distance apart and then shook the board to produce multiple realizations of meander patterns for a fixed tortuosity. Ghosh and Scheidegger (1971) extended the results of that study in a later paper, with the conclusion that so-called "natural wiggly lines" are simply one realization of all possible lines of the same tortuosity between two set points.

A recent example of a stochastic model is Lazarus and Constantine's (2013) directed random walk model, which is capable of producing sinuous curves reminiscent of natural channel planforms. This model operates on a planar "landscape" represented by a rectangular grid with constant slope S. The user selects a positive parameter $\mathcal{R}$. At each grid cell, a random perturbation is selected from a continuous uniform distribution over $[0, \mathcal{R}]$, and

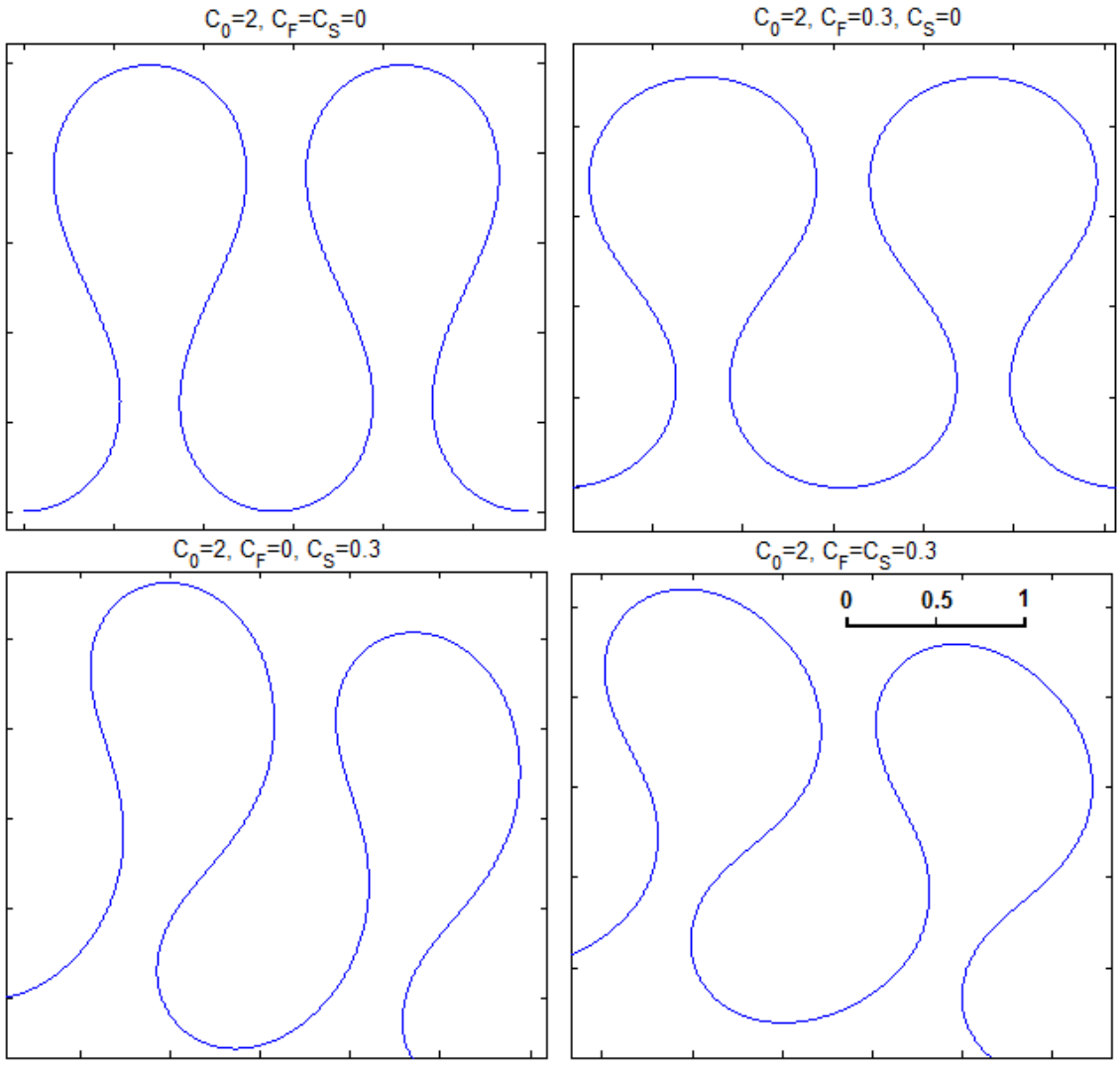

Figure 1.1: *Planform of "channels" produced by the Kinoshita curvature model with varying values of fattening and skewness coefficients. The intrinsic meander length is the same for each curve (i.e., 2π arbitrary length units). The scale is the same in each frame; each tic mark represents 0.5 arbitrary length units.*

added to the original elevation of the cell. Then, starting from the top of the slope, the "flow" walks across the landscape by selecting the adjacent cell with the lowest value of elevation normalized by distance[3]. After several iterations to adjust for "meander cutoffs" (*i.e.*, the elimination of loops where the curve intersects itself), the result is a sinuous path

[3]The distance is equal to $\sqrt{2}$ for the four adjacent diagonal cells and one otherwise. This correction is necessary because a rectangular grid lacks equidistant adjacent cells and could be eliminated if the model were run on a hexagonal grid.

across the domain. The authors observe that high values of the ratio $S/\mathcal{R}$ produce straighter paths, whereas smaller values of $S/\mathcal{R}$ produce highly sinuous paths. This is consistent with the observation that natural meandering channels only occur on low slopes. Moreover, the elevation perturbation scaled by $\mathcal{R}$ may be considered a proxy for natural floodplain variations in resistance to erosion due to heterogeneous sediment distribution, vegetation, *etc.*

1.1.3 Relationship between model output and natural channels

With the introduction of numerical models of meandering comes a need to compare model output to natural channels. Consequently, a number of studies have addressed how to best characterize a channel's planform. In the case of Thakur and Scheidegger's (1970) necklace meanders, the authors measured the "direction angle", or the angle between the horizontal axis and the normal to the channel at any given point, and the "deviation angle", or the difference in direction angle between two successive points. They then analyzed the probability distribution of the deviation angles, and the autocorrelation, power spectrum, and transition probability matrix of the direction angles. These calculations led to the conclusion that the necklace meanders were statistically similar to river meanders. A subsequent study introduced a "degree of wiggliness" parameter, which quantifies the extreme values of the deviation angles (Ghosh and Scheidegger, 1971).

Other authors have focused on developing sets of variables that fully characterize the shape of a channel. Howard and Hemberger (1991) developed a suite of 40 planform variables, of which 27 were non-redundant, and then applied discriminant analysis to demonstrate that existing numerical models (Ferguson, 1976; Ferguson, 1979; Howard and Knutson, 1984) did not adequately reproduce the geometry of natural channels. Frascati and Lanzoni (2009) performed a similar analysis based on 12 non-redundant variables to identify shortcomings in the models by Ikeda *et al.* (1981) and Zolezzi and Seminara (2001). This suite of variables is summarized in Table 1.1.

Table 1.1: Planform variables considered by Frascati and Lanzoni (2009)

Metric	Related non redundant variables	Description
L		Intrinsic length of half meander
L_f		Intrinsic length of full meander
ℓ	ℓ_{av}, ℓ_{var}, ℓ_{sk}, ℓ_{kr}	Cartesian length of half meander
ℓ_f		Cartesian length of full meander
$L^{(u)}$		Intrinsic length from half-meander apex to upstream inflection point
$L^{(d)}$		Intrinsic length from half-meander apex to downstream inflection point
ℓ_T		Cartesian distance from first to last inflection point of reach
$\sigma_T = \frac{\sum L_i}{\ell_T}$	σ_T	Tortuosity
$\sigma_H = \frac{1}{N}\sum \frac{L_i}{\ell_i}$	σ_H	Half-meander average sinuosity (N is the number of half meanders)
$\sigma_F = \frac{1}{M}\sum \frac{L_{f,i}}{\ell_{f,i}}$	σ_F	Full-meander average sinuosity (M is the number of full meanders)
κ	κ_{va} , κ_{kr}	κ refers to the curvature as a space-series along the reach. The average and skewness of curvature are not considered to prevent redundancy in the measurements.
$A = \frac{L^{(u)} - L^{(d)}}{L^{(u)} + L^{(d)}}$	A_{av} , A_{kr} , A_{60-90}	A is the half-meander asymmetry coefficient as defined by Howard and Hemberger (1991). $A_{60-90}$is defined as mean($\{A_i \vert A_{60} \leq A_i \leq A_{90}\}$), where A_{60} is the 60th percentile and A_{90} is the 90th percentile of the set of asymmetry coefficients $\{A_i\}$ along the reach (personal communication with S. Lanzoni, August 3, 2013).

As previously mentioned, spectral analysis is a commonly-used method for identifying periodicities in channel form. More recently, authors have started to apply wavelet analysis to channel measurements as a means of determining how the planform of a channel changes in space. For example, Gutierrez and Abad (2014) apply wavelet analysis to sixteen meandering rivers to identify the relationship among wavelength, amplitude, and the mean center of the channels. Zolezzi and Güneralp (in review) use the wavelet transform on direction data from the Red River, Texas, and the Rio Purus, Brazil, to demonstrate that meanders display a wide range of wavelengths, and that it is rare for a single meander to possess the dominant wavelength for the reach. Likewise, Gutierrez *et al.* (2014) use a wavelet transform to analyze the planform of channels near confluences; this research indicates that wavelength increases directly upstream of confluences and that the curvature maxima decrease downstream of confluences.

1.2 Meandering in tidal channels

As in the purely fluvial case, research regarding tidal meanders has resulted in a number of physical and geometrical models addressing the relevant natural processes or the observed channel planforms. However, there have been far fewer studies published relative to the fluvial case, and the models are not as well constrained by observational data. Additionally, the existing models of tidal systems often contradict each other due to an incomplete understanding of an inherently complex system (Vignoli, 2004, p. 9).

The inner banks of many tidal meanders display a distinctive cuspate shape. This has been attributed to the inertia of the flow displacing the flood current towards the landward edge of the channel, whereas the ebb current is displaced towards the seaward edge of the channel (Ahnert, 1960; Dalrymple *et al.*, 2012, p. 93; Hughes, 2012, p. 286). Physical models of tidal meanders based on bend theory suggest that the same process is responsible for inhibiting meander migration because it shifts the position of highest bed shear stress to the opposite bank when the flow reverses (Solari *et al.*, 2002).

Besides cuspate point bars, another common meander shape in tidal channels is the

"box-shaped" meander (Dalrymple *et al.*, 2012, p. 93); that is, a meander with two local curvature maxima that may resemble right-angle turns. Fagherazzi *et al.* (2004) noted that most of the meanders in their study area displayed this property, with the greater of the two curvature maxima being landward due to ebb-dominant flow. A proposed explanation for these right-angle turns is a positive feedback cycle in which flow separation at bends allows the flow to attack the bank and cause local erosion, resulting in further flow separation (Kleinhans *et al.*, 2009). Box-shaped meanders may be the origin of a difference between tidal and river meanders suggested by the geometrical model of Marani *et al.* (2002). These authors proposed that tidal meanders can be differentiated from fluvial meanders based on the presence of even curvature harmonics. Adapting the well-known Kinoshita equation, the authors represent a channel's curvature in the more general form

$$\kappa(s) = R_1 \cos\left(\frac{2\pi s}{L_f}\right) + I_1 \sin\left(\frac{2\pi s}{L_f}\right) + \varepsilon\left[R_2 \cos\left(2\frac{2\pi s}{L_f}\right) + I_2 \sin\left(2\frac{2\pi s}{L_f}\right) + R_3 \cos\left(3\frac{2\pi s}{L_f}\right) + I_3 \sin\left(3\frac{2\pi s}{L_f}\right)\right] \quad (1.6)$$

where R_1, I_1, R_2 I_2, R_3, and I_3 are coefficients of the same order of magnitude and $\varepsilon < 1$ is a parameter to ensure that the bracketed term remains small. In contrast to Equation 1.5, Equation 1.6 contains even harmonics. If R_1 is constant with $I_1 = 0$, increasing the value of R_2 results in unequal half-meander lengths alternating between short and long, where the longer half-meander may have two local curvature apices (the "box" shape); increasing the value of I_2 shifts the apex of the half-meander such that the curve becomes skewed (Figure 1.2). Because a sine wave is simply a phase-shifted cosine wave, increasing I_2 with I_1 constant and $R_1 = 0$ produces alternating short and long half-meanders, whereas increasing R_2 has a skewing effect. All else constant, changing R_3 or I_3 will have an effect similar to that shown in Figure 1.1. The study found that Equation 1.6 is a better model for the shape of tidal meanders because the Fourier transform of tidal channels' curvature returns a non-negligible second harmonic.

Several studies have provided values for one or more of the parameters identified by

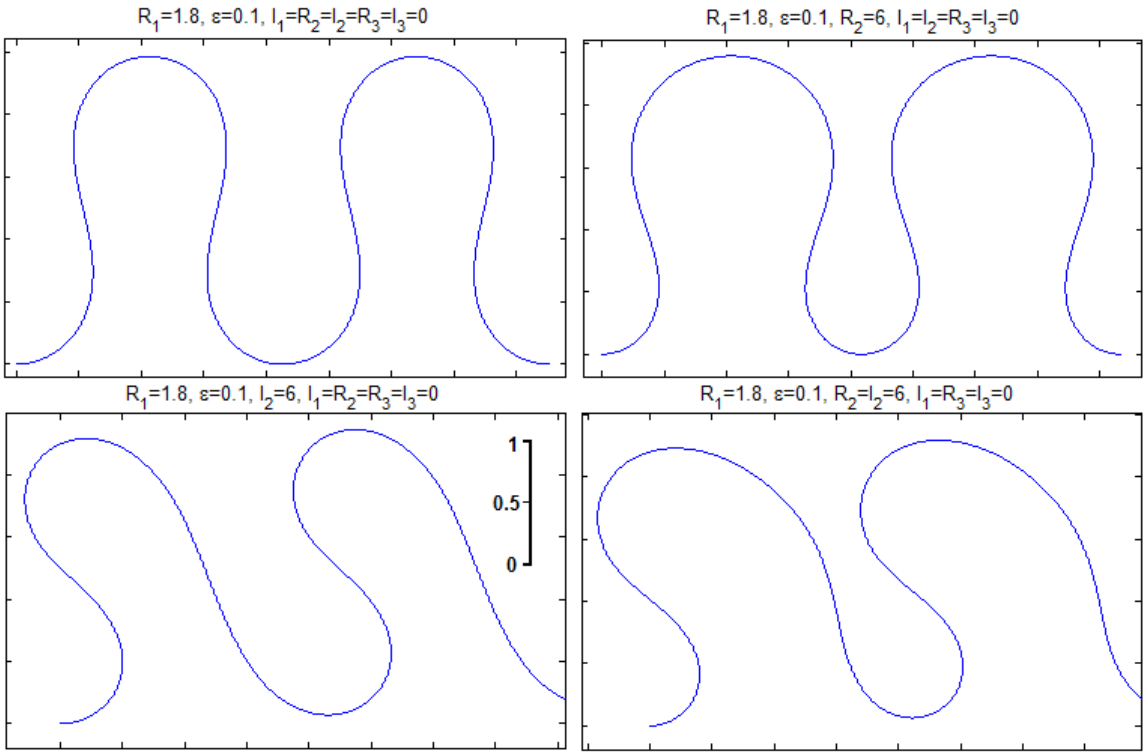

Figure 1.2: *Planform of "channels" with non-negligble second curvature harmonic. The intrinsic meander length is the same for each curve (i.e., 2π arbitrary length units). The scale is the same in each frame; each tic mark represents 0.5 arbitrary length units.*

Frascati and Lanzoni (2009; see Table 1.1). For example, Dury (1971) measured meander wavelengths for a two-limbed tidal channel in Florida and found that the width-normalized intrinsic meander length $\frac{L_f}{W}$ was 7.24 on the western channel limb and 13.63 on the eastern channel limb. Note that we expect these values to be slightly high due to Dury's method of placing the channel centerline at the outside of each bend. Bridges and Leeder (1976) also observed that meander wavelength was poorly correlated with the local width of the channel; the line of best fit to their data set suggests that $\frac{(\text{length})}{W} \approx 8$. However, these authors do not specify whether they measured the intrinsic length L_f or the Cartesian length ℓ_f. Solari *et al.* (2002) report an observed value of $\frac{L_f}{W}$ between 10 and 15, noting that bend theory predicts that the ratio should be larger than what is observed in nature. In contrast, Marani *et al.* (2002) observed slightly larger values of $\frac{L_f}{W}$ between 10 and 20.

Half-meander asymmetry is another important parameter in meander studies. The

commonly used equation for asymmetry is

$$A = \frac{L^{(u)} - L^{(d)}}{L^{(u)} + L^{(d)}} \tag{1.7}$$

(see Table 1.1). Alternatively, Marani *et al.* (2002) derived a shape parameter based on Equation 1.6:

$$\chi = \frac{R_2^* - (2I_2^* + 4I_3^*)}{R_2^* + (2I_2^* + 4I_3^*)} \tag{1.8}$$

where the asterisk indicates that Equation 1.6 has been phase shifted such that $I_1 = 0$. If $\chi > 1$, the meander is downstream skewed, and if $\chi < 1$, the meander is upstream skewed. After computing χ using the Fourier coefficients of measured channel curvature, these authors found that tidal meanders in the Venice Lagoon; Barnstable Marsh, Massachusetts; and Petaluma Bay, California did not display a preferred skewness direction, whereas meanders from Italy's Livenza River were consistently upstream skewed. In contrast, Fagherazzi *et al.* (2004) observed that 64% of the tidal meanders in China Camp Marsh, San Francisco, were upstream skewed; however, these channels experience higher velocities during ebb flow than during flood flow. Burningham (2008) observed that some tidal meanders in the Loughros Estuary, Ireland, balance the asymmetry of the previous meander by being skewed in the opposite direction, although overall the meanders are downstream skewed; this is attributed to flood dominance in the channels.

A number of authors have commented on the sinuosity of tidal channels, but their observations differ greatly. Classifying tidal channels after Strahler (1952), Pestrong (1965) found that high-order channels were more sinuous than low-order channels; only third-, fourth-, and fifth-order tidal channels exceeded a sinuosity of 1.5. Eisma (1998, p. 327), in contrast, noted that straight channels are often the largest channels in the system. In another study based on observation of tidal channels in the Solway Firth, Scotland, Bridges and Leeder (1976) reported that both high and low sinuosity values were possible, but that low sinuosity was more common. With no further definition of the qualitative terms *low* and *high*, it is difficult to compare this to Marani *et al.*'s (2002) measured sinuosity values of $1.3 < \frac{L_f}{\ell_f} < 2.2$ or

Kleinhans *et al.*'s (2009) reported values of $\frac{L_f}{\ell_f} \approx 1.2$ when the channel slope is gentle and $\frac{L_f}{\ell_f} \approx 1.7$ when the slope is steep. We do note that the accepted boundary between "sinuous" and "meandering" river channels is a sinuosity of 1.5, although this number was arbitrarily chosen and is not based on physical differences between the channels (Charlton, 2008, p. 138).

The "straight-meandering-straight" pattern observed in tidally-dominated estuaries (Dalrymple *et al.*, 1992) may elucidate any discrepancies in observed tidal channel sinuosity. These authors found that the outer, flood-dominated portion of tidal estuaries has a low sinuosity; the inner, river-dominated, tidally-influenced reach of the estuary is similarly fairly straight. Between these two straight reaches is a highly sinuous, low-energy reach that corresponds to the bedload convergence zone (Dalrymple *et al.*, 1992; Dalrymple *et al.*, 2012). Indeed, the channel in Figure 2 of Solari *et al.* (2002) displays a reach with sinuosity near one, followed by a reach with sinuosities between two and three, and ends in a reach where the sinuosity is again near one. Thus one would expect very different sinuosity values depending on the portion of the reach in which one measures a tidal channel's sinuosity. At the same time, one must consider the observation that the straight-meandering-straight pattern does not occur in tide-dominated deltas, including the Ganges-Brahmaputra Delta[4]; instead, the channels become less sinuous with distance downstream (Dalrymple and Choi, 2007).

1.3 Width trends at tidal channel mouths

A well known difference between tidal and river channels is that tidal channels widen exponentially in the downstream direction. Indeed, experiments with excavated prismatic, dead-end canals in Indonesia (Savenije, 2005) indicate that parallel banks are not morphologically stable in a tidal environment. This is attributed to erosion at the mouth oversteepening the banks, resulting in bank collapse and widening, while low flow velocities upstream re-

[4]The classification of the Ganges-Brahmaputra Delta as a "delta" is perplexing given that Dalrymple and Choi (2007) also make the following statement: "[T]he abandoned portions of delta plains that are undergoing transgression (*i.e.*, the 'destructive phase' of the delta cycle) are here considered to be estuaries." As the western portion of the Ganges-Brahmaputra-Jamuna Delta is abandoned and regressing (*e.g.*, Allison, 1998b; Rahman *et al.*, 2011), one would expect it to fall within the "estuarine" classification.

sult in sediment deposition and narrowing. Numerical modelling (Fagherazzi and Furbish, 2001) suggests that two factors contribute to the observed widening at tidal channel mouths. First, at the onset of channel development, sediment deposition is high relative to the scour afforded by the intermittent, high-velocity spring tides, producing channels that are wide rather than deep at the mouth. Second, autocompaction of the deposited sediment produces an erosion-resistant layer below the channel, so erosion occurs laterally rather than vertically.

Interest in describing the geometry of tidal channel mouths dates back at least to the publication in which Pillsbury (1939, p. 230; see also Langbein, 1963) formulates an equation for an ideal estuary (that is, an estuary in which the expected depth increase due to funnelling is balanced by the loss of velocity due to friction such that the tidal range, depth, and current are constant along the full length of the channel) as follows:

$$W(s) = W_0 e^{-\frac{as}{\sqrt{gD}}\cot\phi} \tag{1.9}$$

where a is the mean angular speed of the tidal current, D is the constant mean depth at mean tide, and ϕ is the angular lag of the tidal current. However, very few studies address this topic by presenting geometric measurements of natural channels.

A notable exception to this lack of data is the paper by Davies and Woodroffe (2010). These authors analyze the width profiles of 30 tidal estuaries in northern Australia, modeling the shape of the channel as

$$W(s) = W_0 e^{-s/L_b} \tag{1.10}$$

where L_b is the "width convergence length" or e-folding length (*e.g.*, Marani *et al.*, 2002). The results indicate that there is little (if any) correlation between the mouth width and e-folding length, but that the channels with wider mouths are more strongly funnel-shaped than those with narrow mouths. Additionally, estuaries with a higher fluvial discharge have a greater e-folding length. In another study of a natural tidal channel, Ensign *et al.* (2013) estimated that the cross-sectional area at the mouth of the Newport River, North Carolina, is three times greater than it would be in the absence of tidal influence. Assuming that this

greater area does not involve a significant change in depth of the channel (*e.g.*, Savenije, 2005, Section 1.4.1), this suggests a threefold increase in the width of tidal channel mouths relative to the mouth of a non-tidal river with otherwise similar hydraulic properties. Many studies (Friedrichs and Aubrey, 1994; Lanzoni and Seminara, 1998; Marani *et al.*, 2002; Fagherazzi *et al.*, 2004) provide e-folding length values for tidal channels, but it is difficult to compare their results because they are not normalized and the channel mouth widths are not provided.

Before concluding this section, we note that it is common practice in the literature to assume that the width of a tidal channel approaches zero with distance upstream, as in Equation 1.10. However, in certain cases this assumption does not hold. For example, estuaries that receive a non-negligible freshwater discharge from rivers may not decay to zero width until reaching the headwaters hundreds or thousands of kilometers upstream. In such cases, it may be more appropriate to model the shape of the channel as (Vignoli, 2004, p. 16)

$$W(s) = W_\infty + (W_0 - W_\infty)e^{-s/L_b} \tag{1.11}$$

where W_∞ is a positive constant representing the upstream width of the channel.

1.4 Additional differences between tidal channels and river channels

With regards to the planform morphology of individual tidal channels, the two primary differences are the shape of the meanders and the shape of the channel mouth. At the same time, authors have identified a number of differences between tidal and fluvial *networks*. Although this thesis will not emphasize ideas from network theory, we include these observations here for completeness.

Whereas river networks tend to possess a dendritic or tree-like structure, tidal networks are commonly characterized by loops. This implies that multiple, non-unique paths exist between the mouth of the network and a point upstream. Fagherazzi (2008) attributes the presence of loops to the different roles of bed slope in tidal versus fluvial networks. This

is supported by Coco *et al.* (2013), who explain that in river networks, flow is driven by topographic gradients, whereas in the tidal case the flow is driven by water surface gradients.

Scale invariance is a well-known property of fluvial systems at both the meander and the network scale. For example, Leopold and Wolman's (1960) classic figure displays meanders from the 8-foot-wide Duck Creek, Wyoming, the 60-foot-wide New Fork River, Wyoming, and the 3400-foot-wide Mississippi River, Louisiana, all at the width of the page. Without a scale bar, it is impossible to ascertain any difference in the width of the channels. In contrast, Hughes (2012) notes that smaller tidal channels are not generally scaled versions of larger tidal channels, likely the result of different formative processes at the two scales. From a network perspective, tributary fluvial systems at many scales are characterized by Hack's (1957) law: $\mathcal{L} \propto \mathcal{A}^{0.57\pm0.03}$, where $\mathcal{A}$ is the area of the river basin and $\mathcal{L}$ is the mainstream length of the channel. Additionally, the basin area $\mathcal{A}$ is nearly proportional to the discharge Q, which can be estimated from the width of the channel (Rinaldo *et al.*, 1999). Studies report that these relationships do not hold for tidal channels; to quote Rinaldo *et al.* (1999, p. 3905): "[these] analyses reveal a complete lack of such tendencies in tidal channel systems". Cleveringa and Oost (1999) found that channel branching patterns were statistically self-similar above the 500-m scale, but not below. Likewise, Angeles *et al.* (2004) reported that tidal channels were self-similar only at certain scales.

At the same time, some publications suggest that tidal networks and river networks may share certain network properties. For instance, river networks have been shown to be topologically random[5] (*e.g.*, Shreve, 1974). In their study of the North Inlet Estuary, South Carolina, Novakowski *et al.* (2004) tested the topologically random hypothesis for tidal networks and were unable to reject the hypothesis that tidal networks were also topologically random. A second example is Fagherazzi's (2008) observation that tidal channel networks exist in a state of self-organized criticality as a consequence of the system redistributing the tidal prism such that all channels are near the threshold for infilling. The author states that

[5] As explained by Shreve (1974), "A *topologically random* population of channel networks is one in which all topologically distinct networks of the same magnitude are equinumerous." Networks are considered *topologically distinct* if one cannot be continuously deformed to become identical to the other. The classic example of a lack of topological distinction is, of course, the continuous deformation of a doughnut into a coffee mug.

systems at criticality tend to be scale free, contradicting previous observations that tidal channel networks are not scale-invariant.

1.5 Summary

Meandering in alluvial channels is a highly complex process controlled by the interplay of flow hydrodynamics, sediment transport, bed morphodynamics, and bank erosion. Fluvial meanders have captured the attention of researchers for centuries, with significant progress towards a modern understanding of meander evolution beginning with the development of bar theory (Leopold and Wolman, 1957) and bend theory (Ikeda *et al.*, 1981). Authors have addressed the question of meander formation from both a physical and a geometrical perspective, but recent studies (*e.g.*, Frascati and Lanzoni, 2009) indicate that meander models still fall short of fully capturing the planform of natural meandering channels. Despite the strong interest in meanders among the morphodynamics community, a limited number of publications address meandering in tidal channels and whether bidirectional flow produces a meander pattern that is fundamentally distinct from the purely fluvial case. Previous authors have commented on the common shapes exhibited by meanders, including the possibility of a non-negligible second curvature harmonic relative to Kinoshita's curvature model. Several studies have also provided empirical values for tidal channel meander wavelengths, asymmetry, and sinuosity, although there is a great deal of variability in the measured values.

Tidal channels also differ from river channels in that the channels widen exponentially at the mouth in the presence of strong tidal influence. The parameter most commonly used to quantify this exponential shape is the e-folding length, the along-channel distance required for the channel width to decrease by a factor of e relative to the width at the mouth. While several studies have provided values for the e-folding length, only one of these publications (Davies and Woodroffe, 2010) normalizes the e-folding length such that it can be easily compared with values from other channels. Moreover, most studies neglect the fact that not all tidal channel widths decay to zero within the study area, although Vignoli (2004) provides an equation describing this phenomenon.

A number of authors have identified differences between tidal and fluvial channels in the context of network theory. These include the presence of loop structures and a lack of scale invariance in tidal channel networks. However, some recent studies have indicated certain similarities between tidal and fluvial networks that may contradict previous observations concerning scale invariance.

In subsequent chapters, we address the question of whether tidal channels and river channels possess meander- to reach-scale differences in planform based on a study of satellite imagery of the Ganges-Brahmaputra-Jamuna Delta in Bangladesh. Specifically, Chapter Two presents this study in the format of a scientific paper, while Chapter Three elaborates on the methods that we developed for this research. We also include two Appendices; one details the mathematical properties of the sine-generated curve, as discussed above, while the other summarizes our data in tabular format.

Chapter 2

A comparison of the planforms of meandering tidal and fluvial channels on the Ganges-Brahmaputra-Jamuna Delta

Abstract: The planform geometry of tidal channels is controlled by bidirectional flow, a fundamentally different process from that controlling the shape of meandering river channels. However, prior studies do not reach any consensus on how channel planforms differ in these two environments. We use Google Earth imagery to digitize 130 meandering channels on the Ganges-Brahmaputra-Jamuna Delta in Bangladesh, from which we produce a data set of meander and channel width statistics for tidal and fluvial channels. Our data indicate that the tidal meanders are more symmetrical than the river meanders, which are both downstream and upstream skewed. The fluvial meanders are also more sinuous than the tidal meanders. We observe some evidence of longer intrinsic and Cartesian meander wavelengths in the tidal environment, although this could be a consequence of anthropogenic modifications to the fluvial channels. Despite these differences, we find that the relative strength of the first through third curvature harmonics is the same for the tidal and fluvial meanders. Our data set also provides insight into the funnel-shaped geometry of tidal channel mouths; we find that there is a positive correlation between channel mouth width and e-folding length. For those channels with a fluvial connection upstream, there is also a positive correlation between mouth width and upstream width. We propose several causes for the observed trends in our data, but future study will be necessary to test these hypotheses.

2.1 Introduction

Tidal channels are a ubiquitous feature of the tidal landscape, yet in comparison to meandering river channels, their properties remain little-addressed. Forming due to periodic flooding of an initially flat, erodible surface (*e.g.*, Knighton *et al.*, 1992; Fagherazzi and Sun,

2004; D'Alpaos *et al.*, 2006; Vlaswinkel and Cantelli, 2011; Mariotti and Fagherazzi, 2013) or due to the drowning of an existing fluvial channel during episodes of relative sea-level rise (*e.g.*, Gardner and Bohn, 1980), tidal channels exist in a variety of coastal environments and over a variety of scales (Eisma, 1998; Hughes, 2012). The unifying characteristic among these channels, however, is bidirectional flow due to the ebb and flood of the tides. Thus–at least in a hydrodynamic sense–tidal channels are fundamentally different from their fluvial counterparts (Bridges and Leeder, 1976; Fagherazzi *et al.*, 2004). But does bidirectional flow produce a planform morphology distinct from that of a meandering alluvial river?

The question of how tidal channels compare to terrestrial river channels dates back at least to Campbell's (1927) suggestion that tidally-influenced rivers were "inert" with respect to meander formation and cut-off. Barton (1928) soon refuted this claim based on observation of the Brazos River, Texas. Given the ninety-year time span since the inception of this question, coupled with the morphodynamics community's interest in the general question of meandering, it is surprising that a more robust answer has not yet been found. Past studies have compared tidal and fluvial channels primarily from a network perspective. For example, flow in tidal channels is driven by water surface gradients, resulting in loops in the network, whereas the topography-driven flow in river networks prevents the formation of loop structures (Fagherazzi 2008; Coco *et al.*, 2013). Likewise, tidal channel networks lack the property of scale invariance common to river networks (Cleveringa and Oost, 1999; Rinaldo *et al.*, 1999; Angeles *et al.*, 2004), although both tidal and river channel networks may be topologically random (Novakowski *et al.*, 2004).

Far fewer studies have attempted to compare tidal and river channels at the meander- or reach-scale, although one may begin to compare them by synthesizing data from the body of literature specifically focused on tidal channels. For example, although Barwis' (1978) field study of tidal point bars in South Carolina is primarily focused on sedimentology rather than planform morphology, he did note that tidal meanders tend to be skewed upstream as a consequence of ebb-dominant flow. Fagherazzi *et al.* (2004) obtained a similar result based on field study of tidal channels in California, whereas Marani *et al.* (2002) found

that the tidal channels in their study did not display a preferred skewness direction. In contrast, Burningham (2008) noted that although tidal meanders in the Loughros Estuary, Ireland, were preferentially downstream skewed as a result of flood-dominant flow, there was a pattern of meanders "balancing" the asymmetry of the previous meander by being skewed in the opposite direction. We note for comparison that fluvial meanders are typically upstream skewed (*e.g.*, Parker *et al.*, 1983; Marani *et al.*, 2002), although sub-resonant meanders may be downstream skewed (Zolezzi and Seminara, 2001). In all cases, skewing is quite variable.

Two common features observed in tidal channels are cuspate point bars, which result from the inertial displacement of the flood current relative to the ebb current (Ahnert, 1960; Solari *et al.*, 2002; Dalrymple *et al.*, 2012, p. 93; Hughes, 2012, p. 286) and box-shaped meanders, or meanders with two local curvature maxima that may resemble right-angle turns (Fagherazzi *et al.*, 2004; Dalrymple *et al.*, 2012, p. 93). The presence of box-shaped meanders in tidal channels may be the cause of Marani *et al.*'s (2002) observation that the second harmonic of curvature is non-negligible in tidal meanders, considering that one effect of increasing the second curvature harmonic is to produce two local curvature maxima. Fluvial meanders are commonly represented by the well-known Kinoshita curvature equation (*e.g.* Parker *et al.*, 1983; Marani *et al.*, 2002):

$$\kappa(s) = C_0 \left[\cos\left(\frac{2\pi s}{L_f}\right) - C_F \cos\left(3\frac{2\pi s}{L_f}\right) - C_S \sin\left(3\frac{2\pi s}{L_f}\right) \right] \tag{2.1}$$

where C_F and C_S are the fattening and skewness coefficients, respectively. Marani *et al.* (2002) modified this equation by adding terms representing the second harmonics:

$$\begin{aligned} \kappa(s) = R_1 \cos\left(\frac{2\pi s}{L_f}\right) + I_1 \sin\left(\frac{2\pi s}{L_f}\right) + \\ \varepsilon \left[R_2 \cos\left(2\frac{2\pi s}{L_f}\right) + I_2 \sin\left(2\frac{2\pi s}{L_f}\right) + R_3 \cos\left(3\frac{2\pi s}{L_f}\right) + I_3 \sin\left(3\frac{2\pi s}{L_f}\right) \right] \end{aligned} \tag{2.2}$$

where R_1, I_1, R_2 I_2, R_3, and I_3 are coefficients of the same order of magnitude and $\varepsilon < 1$ is a parameter to ensure that the bracketed term remains small. Those authors claimed that

Equation 2.2 is more appropriate for representing the shape of tidal meanders.

Several authors have also provided values for tidal meander wavelength and sinuosity. The reported intrinsic wavelengths, which are normalized by the width of the channel, range from 7.24 (Dury, 1971) to 20 (Marani *et al.*, 2002), with intermediate values being reported by Bridges and Leeder (1976) and Solari *et al.* (2002). It is interesting to note that Solari *et al.* (2002) also approached the question of wavelength from a numerical modelling perspective, introducing bidirectional flow into the "bend" model first introduced by Ikeda *et al.* (1981) and subsequently modified by Blondeaux and Seminara (1985). This research indicates that natural tidal meanders display a smaller wavelength than the fluvially-derived bend mechanism predicts. Reported channel sinuosities (*e.g.* Pestrong, 1965; Bridges and Leeder, 1976; Eisma, 1998; Marani *et al*, 2002; Kleinhans *et al.*, 2009) also vary significantly. Moreover, the sinuosity of the channel may be dependent on the location of the measurement; Dalrymple *et al.* (2002) observed that tidal channels often display a "straight-meandering-straight" pattern, where the outer, flood-dominated and inner, river-dominated reaches have low sinuosity and the bedload convergence zone in between is highly sinuous.

A well known characteristic of tidal channels is that they widen exponentially downstream as a result of bank collapse at the mouth (Savenije, 2005), high deposition rates relative to scour, and autocompaction of deposited sediment preventing the channel from eroding downward (Fagherazzi and Furbish, 2001). The shape of a tidal channel is typically modeled by the equation (*e.g.*, Davies and Woodroffe, 2010)

$$W(s) = W_0 e^{-s/L_b} \tag{2.3}$$

where s refers to along-channel distance from the mouth and L_b is the e-folding length. However, it is difficult to compare the shape of tidal channel mouths in different geographical locations because previously-reported measurements (Friedrichs and Aubrey, 1994; Lanzoni and Seminara, 1998; Marani *et al.*, 2002; Fagherazzi *et al.*, 2004) are not normalized. More

recently, Davies and Woodroffe (2010) devised a tidal-channel shape parameter

$$S_b = \frac{L_b}{W_0} \tag{2.4}$$

which they then used to analyze tidal channels. However, we are unaware of any subsequent studies presenting channel-mouth data in a systematic and normalized manner.

Tidal channels are formed by a fundamentally different process than river channels, yet it remains unclear whether the two types of channels possess distinct planform geometries. Empirical data regarding the shape of tidal-channel mouths is also limited to a single study. Consequently, our goal is to address the following questions in this paper: (1) What is the statistical distribution of the variables characterizing a tidal channel's planform geometry, and are there any fundamental differences in the planform of tidal channels versus non-tidal river channels?; and (2) What are the properties of the downstream widening observed at the mouths of tidally-influenced channels?

2.1.1 Description of the study area

With their headwaters in the Himalayas, the Ganges and Brahmaputra Rivers drain an area of $1.73 \times 10^6\,\mathrm{km}^2$ (Ericson *et al.*, 2006), carrying an estimated 10^9 tons of sediment per year to the Bengal Basin (Goodbred and Kuehl, 1999). The deposition of this enormous sediment load has produced one of the largest deltas in the world, second only to the Amazon Delta in terms of total area (Ericson *et al.*, 2006). But whereas many macrotidal river mouths (*e.g.*, Amazon River, Fly River) lack a subaerial delta, the high percentage of coarse sediment load carried by the Ganges and Brahmaputra Rivers enabled the formation of a large subaerial delta plain during the Holocene (Allison, 1998b). The modern delta stretches from the Hooghly River in the west to the Meghna Estuary in the east; the eastern delta plain is currently active and progradational, while the region west of 89.9°E (the Haringhata River mouth) is abandoned and experiencing net land loss (Allison, 1998b; Rahman *et al.*, 2011).

The subaerial delta is divided into a tidally influenced lower delta plain and an upper

delta plain that is purely fluvially controlled (Kuehl *et al.*, 2005). The lower delta plain is composed of a series of digitate, north-south oriented peninsulas separated by large, funnel-shaped tidal channels; these likely represent former mouths of the Ganges River created as the channel migrated eastward to its present location (Allison, 1998b; Allison and Kepple, 2001; Allison *et al.*, 2003; Kuehl *et al.*, 2005). The tidal range at the coast is 1.9 m in the west and 2.8 m in the east (Barua, 1990), although estuarine funneling effects increase the range to as high as 6.7 m in the channels (Chatterjee *et al.*, 2013). Wave energy in this region is comparatively low (Coleman *et al.*, 2008). The world's largest mangrove forest, the Sundarbans (var. *Sunderbans*), covers about 10,000 km^2 along the western delta plain (*e.g.*, Food and Agriculture Organization, 2007; Iftekhar and Saenger, 2008; De, 2009); this region is characterized by a dense network of tidal channels dividing the land surface into numerous small islands (Passalacqua *et al.*, 2013). The coastline in eastern Bangladesh was similarly covered with mangroves as late as the 18^{th} century, but it has since been cleared for cultivation (Allison *et al.*, 2003; Kuehl *et al.*, 2005) and embanked to prevent flooding and erosion (Rahman *et al.*, 2011). These embankments, or "polders", have had the effect of eliminating many of the smaller tidal channels (Kuehl *et al.*, 2005).

The upper delta plain is the portion of the delta above the limit of tidal influence, which corresponds to elevations exceeding 3 meters above sea level (Kuehl *et al.*, 2005). The rivers in this region are extremely prone to lateral migration and avulsion as a consequence of one or more of the following: tectonic uplift and subsidence (Morgan and McIntire, 1959; Coleman, 1969; Goodbred and Kuehl, 2000), earthquake-driven sedimentation (Sarker and Thorne, 2006), extreme discharge during the annual monsoon (Hossain *et al.*, 2013), and rapid channel infilling (Coleman, 1969; Pickering *et al.*, in press) caused by the relatively coarse sediment load (Kuehl *et al.*, 2005). The result is a land surface dominated by abandoned channel scars of similar size to the modern channels (Coleman *et al.*, 2008). The upper delta plain is composed of larger island and narrower channels in comparison to the lower delta plain (Passalacqua *et al.*, 2013), which previous authors have attributed to natural channel abandonment (Allison, 1998a; Allison, 1998b) and anthropogenic diversion of water from the

channels (Mirza, 1997; Bharati and Jayakody, 2011).

2.2 Methods

The first step in analyzing channel planforms is to obtain a digital representation of the shape and position of the channel's banks and/or centerline. Methods for identifying the position of the banks include automatic network extraction from digital topographic maps (Fagherazzi *et al.*, 1999), generation of a binary land-water map using spectral data from Landsat (Passalacqua *et al.*, 2013), or manual selection of points on the bank from imagery in GIS (Legleiter and Kyriakidis, 2006; Davies and Woodroffe, 2010). A channel's centerline can be found directly through manual selection of points along the center of the channel (Ferguson, 1975; Howard and Hemberger, 1991; Mariethoz *et al.*, 2014) or indirectly by applying a suitable operation to the digitized banks (Legleiter and Kyriakidis, 2006; Davies and Woodroffe, 2010).

We selected Google Earth as the source of data for this study because this software offers free and user-friendly access to satellite imagery with resolution better than one meter per pixel and has been shown to greatly improve measurement accuracy relative to Landsat methods (Fischer *et al.*, 2012). We manually digitized the left and right banks of each channel using Google Earth's "Add Path" tool, with a target sampling density of eight points per local channel width. In order to obtain bank positions that were independent of stage and tidal cycle, we defined the banks as the limit of permanent vegetation along the channel (Guccione, 1983; Legleiter and Kyriakidis, 2006). The digitized channels were classified as tidal or fluvial based on a compilation of tidal range data from Shri and Chugh (1961), Allison (1998b), Chatterjee *et al.* (2013), Mikhailova (2013), and the location of recent sedimentary tidal deposits as mapped by Persits *et al.* (2001). We further classified the tidal channels based on the opening angle of the mouth (Shaw *et al.*, 2008), connection to upstream fluvial input, and whether the channel displayed unambiguous directionality as evidenced by a clear decrease in width upstream and/or an approximately north-south orientation.

Previous studies addressing the statistical properties of meandering rivers have required

that all data must come from reaches that are a minimum of 40 meanders in length with no major confluences over this distance (Howard and Hemberger, 1991). However, considering that the tidally-influenced portion of the Ganges-Brahmaputra Delta is covered by a densely-interconnected network of channels (Passalacqua *et al.*, 2013), a single channel thread commonly persists over only three or four full meanders before intersecting another channel. We consequently find it necessary to assume that all tidal meanders on the Ganges-Brahmaputra Delta are realizations of the same fundamental process, and that by computing statistics for individual meanders (or for short reaches composed of two or three consecutive meanders), we can analyze their properties as an aggregate. With regards to digitizing channels, then, we begin at the mouth of the channel and proceed upstream until reaching an intersection. As the boundary conditions of our smoothing procedure will require us to discard a certain amount of data at the beginning and end of each channel, it is desirable to extend the channel past the intersection to minimize the amount of data that must be eliminated. If we can continue moving upstream without the digitized channel experiencing an abrupt change in width and visible meander wavelength, we select a direction at random and continue, but in no case do we allow a channel to return to the coast or form a loop. After digitization is complete, we export the banks to MATLAB and convert from degrees latitude/longitude to Bangladesh Transverse Mercator (BTM) coordinates (Ministry of Irrigation, 1992) with WGS84 as the reference ellipsoid.

Unlike those papers that use the position of the thalweg as the channel's centerline (Dury, 1971; Ferguson, 1975; Kopsick, 1983), we define the centerline as the medial axis or skeleton (Blum, 1967; Lee, 1982) of the region defined by the left and right banks. This definition is the same, in name or in concept, as that used by Fagherazzi *et al* (1999), McAllister and Snoeyink (2000), and Davies and Woodroffe (2010). We approximate the medial axis by computing the Voronoi polygonization (Brandt, 1994) of the digitized points on the left and right banks and then selecting those Voronoi vertices that define a curve down the center of the channel. This procedure was fully automated in MATLAB and is detailed in the Supporting Information.

To determine the most effective method for smoothing a noisy, unevenly sampled, nonstationary signal, we developed a test case of $y = \frac{sin(x^2)}{x} + \varepsilon(x)$, $x \in [0.01, 6]$, where $\varepsilon(x)$ is a noise term that scales with the local amplitude of the signal. We smoothed this artificial data using the algorithms proposed by Savitzky and Golay (1964), Douglas and Peucker (1973), Rosensaft (1995), and several variants on the standard smoothing spline algorithm (*e.g.*, De Boor, 1978) before determining that the best method was to apply a weighted smoothing spline to the channel's centerline. In other words, the smoothed data is represented by the function $f(x)$ that minimizes

$$p \sum_{j=1}^{n} w_j [y_j - f(x_j)]^2 + (1-p) \int_{x_1}^{x_n} [f''(t)]^2 \, dt \tag{2.5}$$

where $\{(x_j, y_j)\}_{j=1}^{n}$ are the coordinates of the n data points, p is a parameter controlling the trade-off between goodness of fit (series term) and smoothness (integral term) and w_j is a weight controlling data fidelity at the j^{th} point. In contrast to the standard method of choosing w_j based on the inverse of the variance of y_j (Reinsch, 1967; Woodford, 1970; De Boor, 1978), we assign the highest weights to those regions with the greatest apparent curvature, as these are the locations where the spline is most likely to misrepresent the generating function's true shape.

Considering that a channel's centerline can rarely be represented as a function of a single variable (Güneralp and Rhoads, 2008), we apply the smoothing spline algorithm to the channel centerlines in parametric form:

$$p \sum_{j=1}^{n} w_j [x_j - f_1(s_j)]^2 + (1-p) \int_{s_1}^{s_n} [f_1''(t)]^2 \, dt \tag{2.6}$$

$$p \sum_{j=1}^{n} w_j [y_j - f_2(s_j)]^2 + (1-p) \int_{s_1}^{s_n} [f_2''(t)]^2 \, dt. \tag{2.7}$$

Here, s is an independent parameter that approximates arc length along the centerline using the Euclidean distance between consecutive centerline points, with $s = 0$ at the downstream end of the channel (as in Figure 2 of Marani *et al.*, 2002). We begin with a value of $p =$

$(1+\frac{h^3}{0.001})^{-1}$, where h is the average spacing of s (The MathWorks, 2014), and use a graphical user interface to manually assign weights $w^{(1)} = 1$, $w^{(2)} = 5$, and $w^{(3)} = 25$ to regions of low, moderate, and high curvature, respectively. After calculating smoothed values for the x_j and y_j, we visually examine a plot of the smoothed centerline to evaluate its performance. If we observe the smoothing to be excessive or insufficient, we adjust one or more of p, $w^{(1)}$, $w^{(2)}$, or $w^{(3)}$ and/or add additional weights $w^{(4)}$ and $w^{(5)}$. We repeat this process until we have obtained a smooth parametric curve that provides a good representation of the original Voronoi vertices. Using this curve, we can analytically calculate the curvature of the centerline at any point using the formula

$$\kappa(s) = \frac{\frac{dx}{ds}\frac{d^2y}{ds^2} + \frac{dy}{ds}\frac{d^2x}{ds^2}}{[(\frac{dx}{ds})^2 + (\frac{dy}{ds})^2]^{3/2}}. \tag{2.8}$$

Note that because s increases with distance inland from the coast, κ is positive if the ebb flow (or averaged downstream flow, in the non-tidal case) is turning clockwise and negative if the ebb flow is turning counterclockwise.

Our next task is to obtain the width profile of the channel as a space series along the centerline. A channel's width is generally defined as the distance across the channel normal to the centerline (Pavelsky and Smith, 2008; Davies and Woodroffe, 2010). Upon implementing this definition, we observed that in very tight meander bends, a line segment normal to the channel's centerline will often miss the nearest point bar and instead intersect the bank at a considerable distance up or downstream. The effect is an erroneous spike in width at that point along the channel. To correct for this, we define the width of the channel at a point (x_j, y_j) along the centerline as the shortest possible line segment intersecting both banks and containing (x_j, y_j). In practice, this line segment rarely deviates from the normal by more than a small angle. As it is computationally intensive to search for the shortest distance across the channel at each point along the centerline, we estimate the width of the channel using the normal to the centerline and then perform a shortest-distance search only at those locations that display a significant deviation from the overall trend in widths along the channel.

After obtaining the widths at all points along the centerline, we fit trendlines to the data using three different models for the shape of the channel. Model 1 represents an exponential change in width, represented by the equation $W(s) = W_0 e^{-s/L_b}$, where L_b is the arc length required for the channel's width to decrease by a factor of e. Model 2 is a variation on the exponential model in which the width asymptotically approaches a nonzero constant, *i.e.* $W(s) = (W_0 - W_\infty)e^{-s/L_b} + W_\infty$. Finally, after observing that the upstream channel width W_∞ in Model 2 occasionally took on a negative value, we introduced Model 3, in which the width at infinity was forced to equal the average of the last few[1] measured widths. We used the nonlinear least squares method described by Davies and Woodroffe (2010) to fit the parameters for each model. If the channel was clearly blind, we automatically assigned it to Model 1. Channels with upstream connections were more complicated because they often terminate abruptly by intersecting another channel; we have no knowledge of how the channel would behave upstream because the channel simply ceases to exist. Consequently, we considered two working hypotheses: (1) that the channel would have decayed to zero width if it had not intersected another channel (Model 1), and (2) that the channel would have maintained a positive constant upstream width by connecting to a fluvial channel (Model 2 or 3). If a connected channel obtained a negative value for W_∞ in Model 2, we used Model 3 by default to represent its width. However, if W_∞ was positive in Model 2, we selected the better of Model 2 or Model 3 based on the R^2 value obtained for each. Model 2 most commonly displayed the higher R^2 value because of the presence of a third fitted parameter; however, there were several occasions in which the nonlinear least squares algorithm did not converge in the maximum number of iterations for Model 2, resulting in a higher R^2 value for Model 3.

Having obtained the curvature as a function of s, we are able to locate the channel's inflection points by finding all points at which $\kappa(s) = 0$. This is an important step in our analysis because, in general, any three consecutive inflection points define one full meander (Marani *et al.*, 2002), which is the basis for most of the metrics we wish to evaluate. The pre-

[1] The exact number of measurements to average was defined separately for each channel based on observation of the length of the data series' "tail".

viously described smoothing algorithm should have eliminated most curvature sign-changes resulting from irregularities in the bank or as an artifact of the medial axis approximation. However, there may be locations at which the curvature changes sign over a very short length scale or takes on a zero value without changing sign, forming a "compound meander" (Güneralp and Rhoads, 2008). We attempted to automate the inflection point selection process by defining a "meander" as a reach of channel defined by two consecutive inflection points that exceeds a given percentage of the mean curvature magnitude for the channel. Although we tested the algorithm with various threshold percentages, we found that it was prone in some cases to deleting inflection points that the human eye would identify as "real" and retaining inflection points that were likely the result of noise. Consequently, the author manually selected the subset of inflection points to keep. The risk with manual meander identification is imprinting the author's idea of a "meander" on the data, so we attempted to standardize the process as follows. The primary criterion for inflection point selection was the shape of the banks; we required that both banks display the same curvature sign within a meander. We also deleted those inflection points that appeared to be a result of noise on the bank.

Frascati and Lanzoni (2009) proposed a suite of variables for characterizing channel planforms (see Table 1.1), which we use here. For the individual meanders, we measure each of the following values based on the set of inflection points we have selected:

- L, the arc length of each half meander
- L_f, the arc length of each full meander
- $L^{(u)}$, the arc length from the half-meander's point of maximum curvature to the upstream inflection point
- $L^{(d)}$, the arc length from the half-meander's point of maximum curvature to the downstream inflection point
- ℓ, the Euclidean distance between any two inflection points defining a half-meander
- ℓ_f, the Euclidean distance between any two inflection points defining a full meander.

From these values we are able to calculate the half-meander and full-meander sinuosities and the asymmetry coefficient. Note that although any given half meander is a part of two overlapping full meanders, we restrict each half meander to being part of only one full meander to avoid repeated measurements in our data set. Following Marani *et al.* (2002), we also wish to determine the relative magnitude of the curvature harmonics, but the nonstationary nature of the tidal meanders limits the applicability of the Fourier transform. Rather than analyze an entire reach, we take a separate Fourier transform of each full meander's curvature to determine which harmonics are dominant (Figure 2.1). Our primary interest is to determine the prevalence of the second curvature harmonic, so we define a metric $V = \frac{\mathcal{F}_2}{\mathcal{F}_1+\mathcal{F}_3}$, where $\mathcal{F}_1$, $\mathcal{F}_2$, and $\mathcal{F}_3$ are the magnitudes of the first, second, and third curvature harmonics as determined by the Fourier transform. The reader is referred to Figures 1.1 and 1.2 in the previous chapter for examples of how the second and third curvature harmonics influence a meander's shape.

We also repeated these measurements for each set of two consecutive meanders and each set of three consecutive meanders, with the goal of obtaining metrics that are averaged over short reaches of channel. As described in the previous paragraph, we do not allow any partial overlap between the channel segments. All values are calculated by averaging the respective values from the half- or full-meander calculations, with the following exceptions. First, we measured the average sinuosity as $(\frac{L_{f,i}+L_{f,i+1}}{\ell_{f,i}+\ell_{f,i+1}})$ for the two meander case and $(\frac{L_{f,i}+L_{f,i+1}+L_{f,i+2}}{\ell_{f,i}+\ell_{f,i+1}+\ell_{f,i+2}})$ for the three meander case. This is not generally equal to the average full meander sinuosity, given by either $\frac{1}{2}(\frac{L_{f,i}}{\ell_{f,i}} + \frac{L_{f,i+1}}{\ell_{f,i+1}})$ or $\frac{1}{3}(\frac{L_{f,i}}{\ell_{f,i}} + \frac{L_{f,i+1}}{\ell_{f,i+1}} + \frac{L_{f,i+2}}{\ell_{f,i+2}})$, although in practice the two definitions of average sinuosity vary by only a small amount. The second exception is that we recomputed the Fourier transform using the full set of curvature values for the two or three meanders of interest, anticipating that the Fourier transform would improve in performance when given more data. In the two meander case, this requires us to change the metric to $V = \frac{\mathcal{F}_4}{\mathcal{F}_2+\mathcal{F}_6}$, and in the three meander case the metric becomes $V = \frac{\mathcal{F}_6}{\mathcal{F}_3+\mathcal{F}_9}$ to account for the presence of two and three additional periods, respectively. These formulae are summarized in Table 2.1.

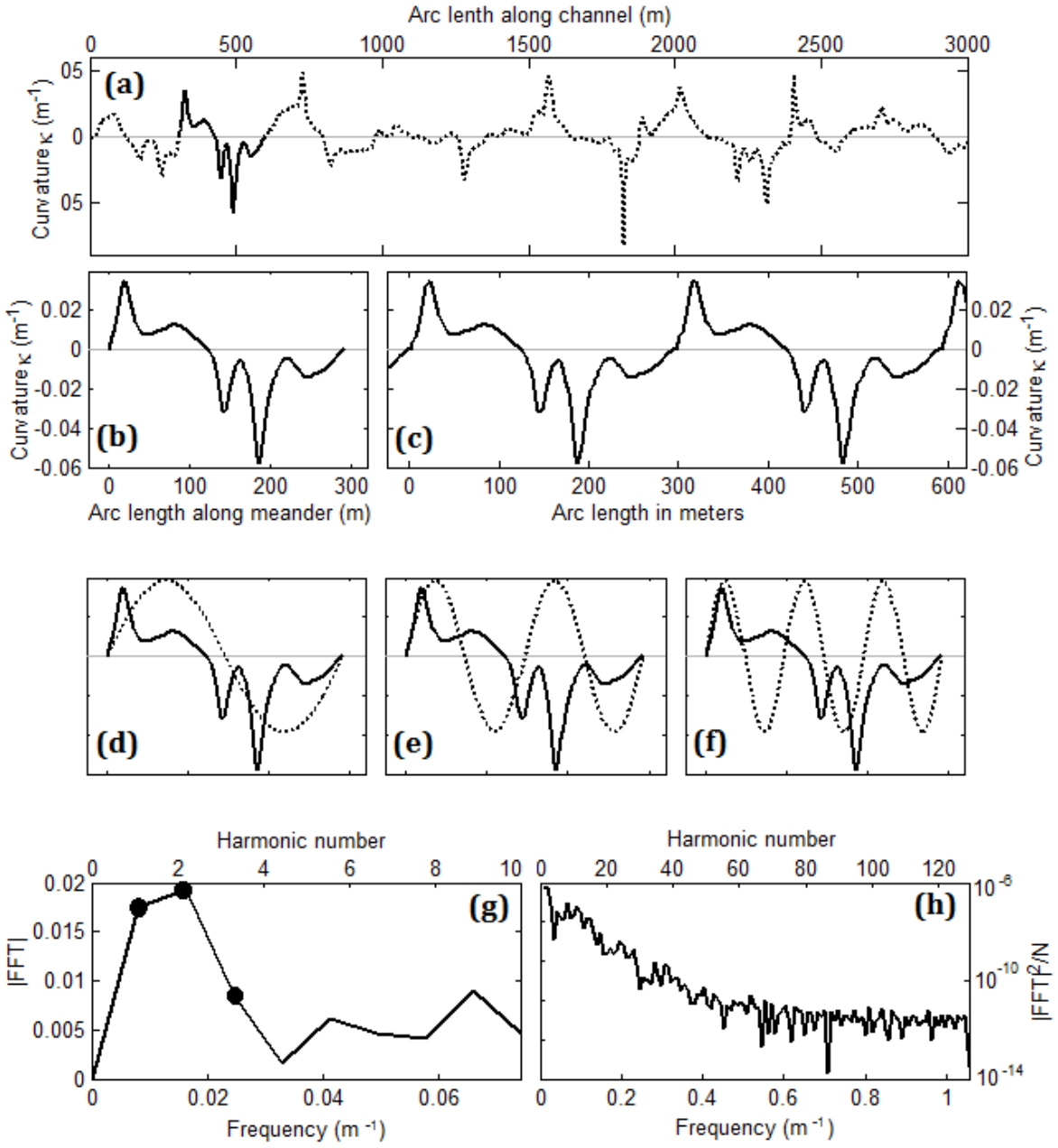

Figure 2.1: *Example of using the Fourier transform to analyze an individual meander's curvature. (a) A portion of the curvature measurements for Channel 122. The curvature corresponding the meander we wish to analyze is highlighted with a solid line. (b) Enlargement of the curvature for the meander of interest. Note that we do not consider any curvature data outside of this meander. (c) An assumption of the Fourier Transform is that the data is periodic, with its period corresponding to the length of the data series. This subfigure is an example of what the Fourier Transform "sees" with regards to the meander of interest. (d), (e), and (f) Sinusoids corresponding to the first, second, and third harmonics, respectively. The purpose of the Fourier Transform is to determine how much of the signal's energy is contained in each frequency. (g) The magnitude of the first few harmonics returned by the Fourier Transform. The values of the first, second, and third harmonic magnitudes are highlighted with black dots. (h) The power spectrum of the meander's curvature.*

Table 2.1: Channel planform metrics used in this study

Metric description (half meander/one full meander case)	**Two-meander case (if applicable)**	**Three-meander case (if applicable)**
L, the intrinsic wavelength (arc length) of one half meander	—	—
L_f, the intrinsic wavelength (arc length) of one full meander	$\frac{1}{2}(L_{f,i} + L_{f,i+1})$	$\frac{1}{3}(L_{f,i} + L_{f,i+1} + L_{f,i+2})$
$L^{(u)}$, the arc length from the half meander's point of maximum curvature to the upstream inflection point	—	—
$L^{(d)}$, the arc length from the half meander's point of maximum curvature to the downstream inflection point	—	—
ℓ, the Cartesian half-meander wavelength, measured as the Euclidean distance between two inflection points defining one half meander	—	—
ℓ_f, the Cartesian full-meander wavelength, measured as the Euclidean distance betwee any two inflection points defining one full meander	$\frac{1}{2}(\ell_{f,i} + \ell_{f,i+1})$	$\frac{1}{3}(\ell_{f,i} + \ell_{f,i+1} + \ell_{f,i+2})$
L/ℓ, the half-meander sinuosity	—	—
L_f/ℓ_f, the full-meander sinuosity	$(\frac{L_{f,i}+L_{f,i+1}}{\ell_{f,i}+\ell_{f,i+1}})$	$(\frac{L_{f,i}+L_{f,i+1}+L_{f,i+2}}{\ell_{f,i}+\ell_{f,i+1}+\ell_{f,i+2}})$
$A = \frac{L^{(u)}-L^{(d)}}{L^{(u)}+L^{(d)}}$, the half-meander asymmetry coefficient	—	—
$V = \frac{\mathcal{F}_2}{\mathcal{F}_1+\mathcal{F}_3}$, the magnitude of the second Fourier harmonic to the first plus third Fourier harmonics	$\frac{\mathcal{F}_4}{\mathcal{F}_2+\mathcal{F}_6}$	$\frac{\mathcal{F}_6}{\mathcal{F}_3+\mathcal{F}_9}$

Finally, we fit trendlines to our measured values using one of two methods. For the channel wavelength measurements, we log-transformed the meander widths and wavelengths and then used linear least squares to obtain the power law of best fit. We selected linear least squares for these calculations because even though error is present in both the width and the wavelength data, linear least squares is most appropriate when one variable restricts, limits, or determines the other in a causal or noncausal manner (Smith, 2009). In the case of meander wavelengths, this is reflected in the basic idea that width limits wavelength because if a channel takes on too small a wavelength relative to its width, it will intersect itself and form an oxbow (Marani *et al.*, 2002). To address trends in the fitted width parameters from Models 1, 2, and 3, we log-transformed the data and used a reduced major axis algorithm because we have no *a priori* knowledge of whether one parameter controls another.

2.3 Results

After analyzing the half-meanders, we find that low sinuosities are preferred in both the tidal and the fluvial case. The average half-meander sinuosity for the tidal meanders is $\sigma_{H,\text{tidal}} = 1.268$, whereas the average half-meander sinuosity for the fluvial meanders is $\sigma_{H,\text{fluvial}} = 1.311$. The histograms of the sinuosity values (Figure 2.2) are visually quite similar. Indeed, performing a Kolmogorov-Smirnov test at $\alpha = 5\%$ ($n_{\text{tidal}} = 1526$, $n_{\text{river}} = 700$, $\mathcal{D} = 0.0598$, $\mathcal{D}_{\alpha,\text{crit}} = 0.0621$), we cannot reject the null hypothesis that the tidal half-meander sinuosity and the river half-meander sinuosity come from the same distribution.

The half-meander Cartesian length is correlated with the width of the channel in both the tidal and the fluvial case (Figure 2.3), although the scatter is considerable. The best-fitting power law for the tidal half-meanders is $\ell = (5.045 \pm 0.513)W^{0.960\pm0.020}$; the error bounds were calculated at $\alpha = 0.05$. For the fluvial half-meanders, the best-fitting power law is $\ell = (3.941 \pm 0.961)^{1.082\pm0.045}$. Note that the fitted power law functions both have powers very close to one, indicating that these relationships are approximately linear. The coefficient in the fitted tidal equation is larger than the coefficient in the fitted river equation, although we observe that the error in the coefficients is such that they could conceivably be equal for

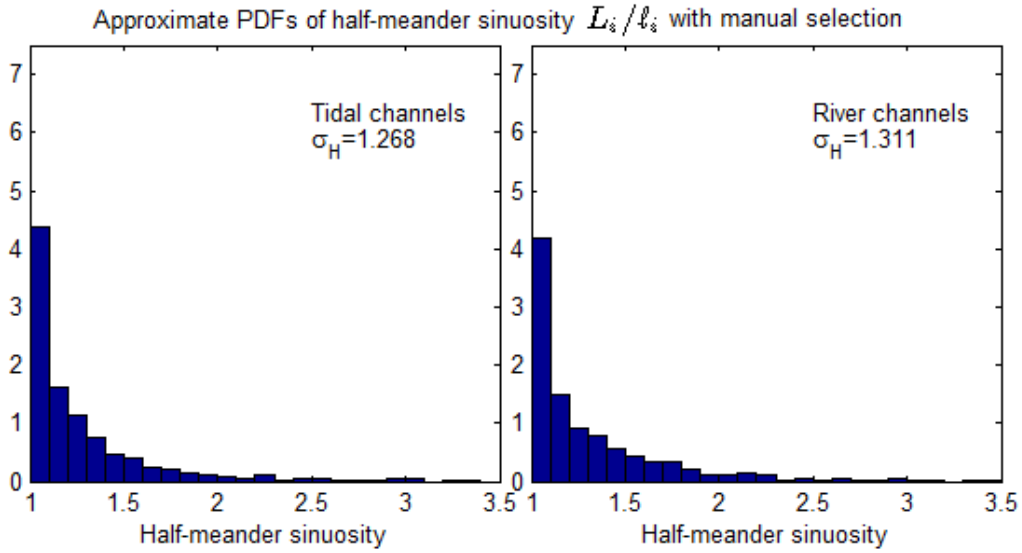

Figure 2.2: *Histograms approximating the probability density functions of half-meander sinuosity for the tidal meanders (left) and the river meanders (right).*

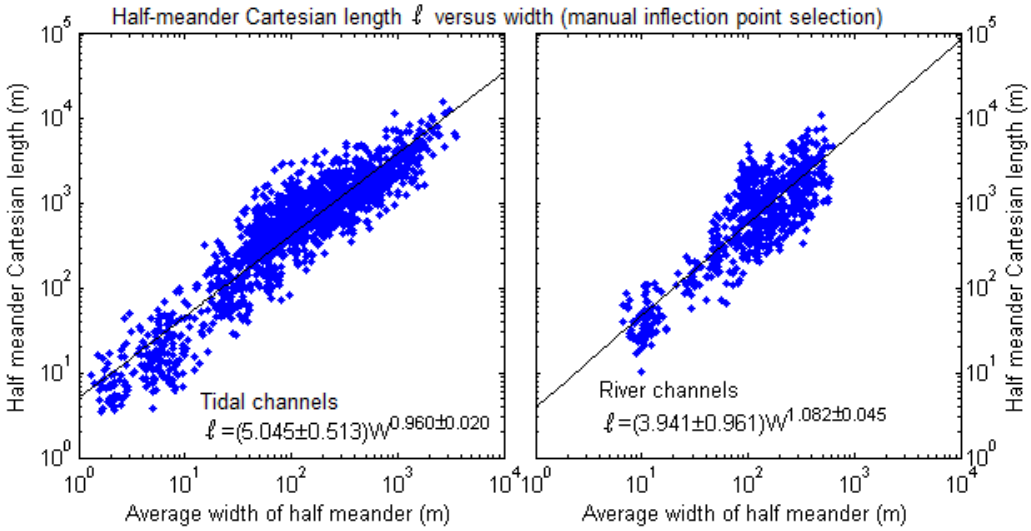

Figure 2.3: *Plot of half-meander Cartesian length ℓ versus the average width of the half meander for the tidal meanders (left) and the river meanders (right). The power law fits were obtained by log-transforming the data and using linear least squares.*

both the tidal and fluvial channels.

Our results for the half-meander intrinsic length are displayed in Figure 2.4. As with the half-meander Cartesian length, the power law relation between width and intrinsic length is approximately linear in both the tidal and fluvial cases, with a power of 0.953±0.021 for the

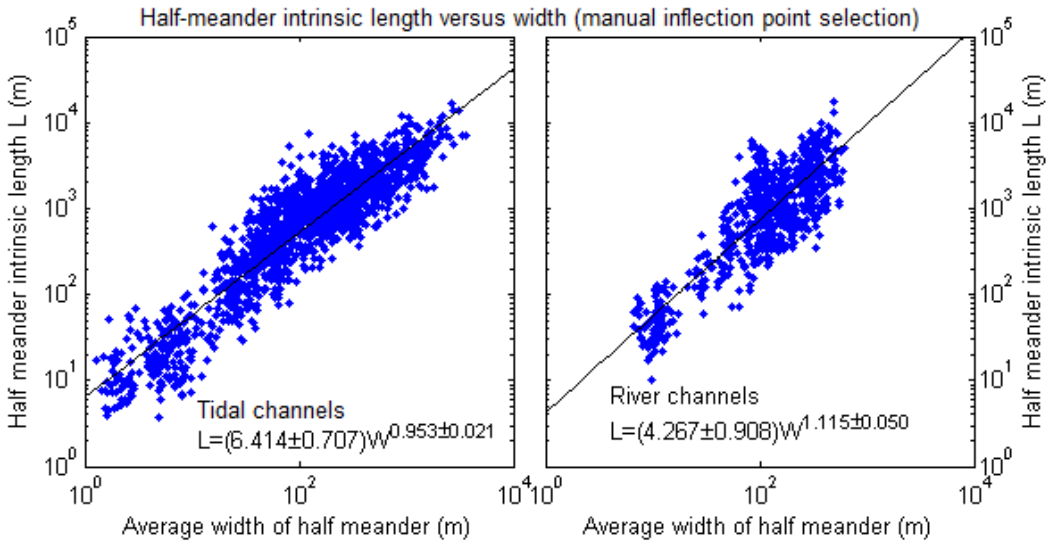

Figure 2.4: *Plot of half-meander intrinsic length L versus the average width of the half meander for the tidal meanders (left) and the river meanders (right).The power law fits were obtained by log-transforming the data and using linear least squares.*

tidal channels and 1.115 ± 0.050 for the river channels. The most notable difference between the two data sets is in the trendline coefficients, with the tidal channels displaying a larger value of 6.414 ± 0.707 relative to the river channels' 4.267 ± 0.908. This implies that for a given width, the tidal channels display a longer arc length between inflection points than the river channels.

Before considering our results regarding the asymmetry coefficients, we note that we only consider those tidal channels which display a clear directionality, either due to a pronounced decrease in width and/or an approximately north-south orientation. We also note that we use the word "skewness" in two contexts. The "skewness" of a half meander refers to the physical position of its curvature apex relative to the defining inflection points, whereas the "skewness" of a distribution refers to the value of the third statistical moment. We observe a visible difference between the tidal and river half-meanders when we consider the asymmetry coefficients (Figure 2.5). On average, both the tidal and the river meanders are slightly upstream skewed (in the physical sense), with $A_{\text{av,tidal}} = -0.0424$ and $A_{\text{av,river}} = -0.0229$. However, the variance is noticeably higher for the river meanders, producing a histogram that is distributed more evenly across the possible values of A. Additionally, the tidal meanders

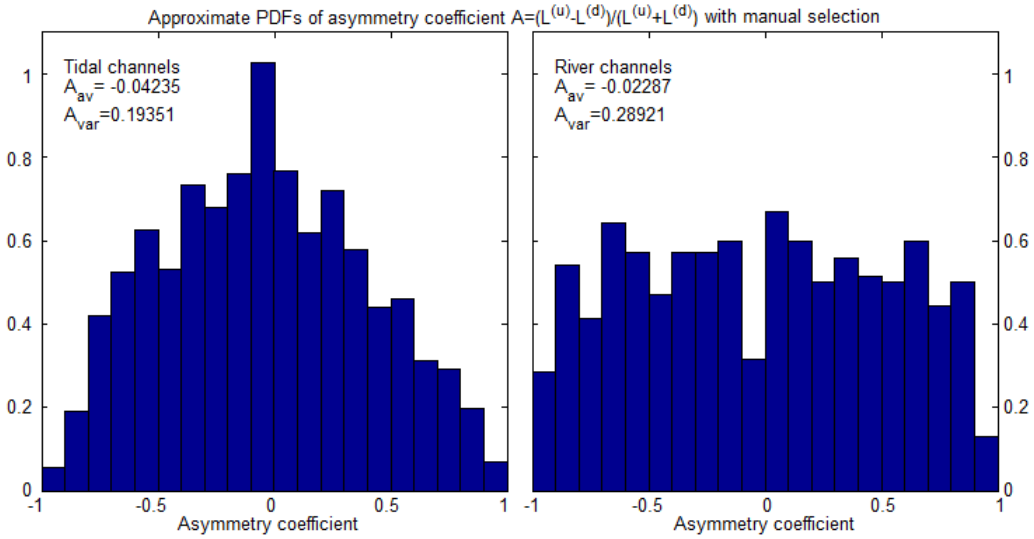

Figure 2.5: *Histograms approximating the probability density functions of the asymmetry coefficients for the tidal half-meanders (left) and the river half-meanders (right).*

are more positively skewed ($A_{\text{sk,tidal}} = 0.119$) than the river meanders ($A_{\text{sk,river}} = 0.0168$). It is unsurprising, then, that the Kolmogorov-Smirnov test ($n_{\text{tidal}} = 1472$, $n_{\text{river}} = 700$, $\mathcal{D} = 0.0947$, $\mathcal{D}_{\alpha,\text{crit}} = 0.0624$) allows us to reject the null hypothesis that the two distributions are the same at $\alpha = 5\%$.

Having addressed our results for the half-meander metrics, we now turn our attention to the results regarding the full meanders. Figure 2.6 displays histograms for the full-meander sinuosity in both tidal and fluvial channels. For the individual full meanders, we observe that the tidal meanders show a stronger preference for low sinuosity values, whereas the histogram for the river meanders displays a more pronounced tail. Based on a Kolmogorov-Smirnov test at $\alpha = 5\%$ ($n_{\text{tidal}} = 732$, $n_{\text{river}} = 348$, $\mathcal{D} = 0.0901$, $\mathcal{D}_{\alpha,\text{crit}} = 0.0886$), we reject the null hypothesis that the tidal full-meander sinuosity and the river full-meander sinuosity come from the same distribution. When we plot the histograms of the full-meander sinuosity measured over two and three meanders, the difference in the shape of the distributions becomes even more obvious. Again, the Kolmogorov-Smirnov test ($n_{\text{tidal}} = 343$, $n_{\text{river}} = 170$, $\mathcal{D} = 0.129$, $\mathcal{D}_{\alpha,\text{crit}} = 0.128$ for the two-meander case; $n_{\text{tidal}} = 208$, $n_{\text{river}} = 111$, $\mathcal{D} = 0.167$, $\mathcal{D}_{\alpha,\text{crit}} = 0.160$ for the three meander case) allows us to reject the null hypothesis at $\alpha = 5\%$

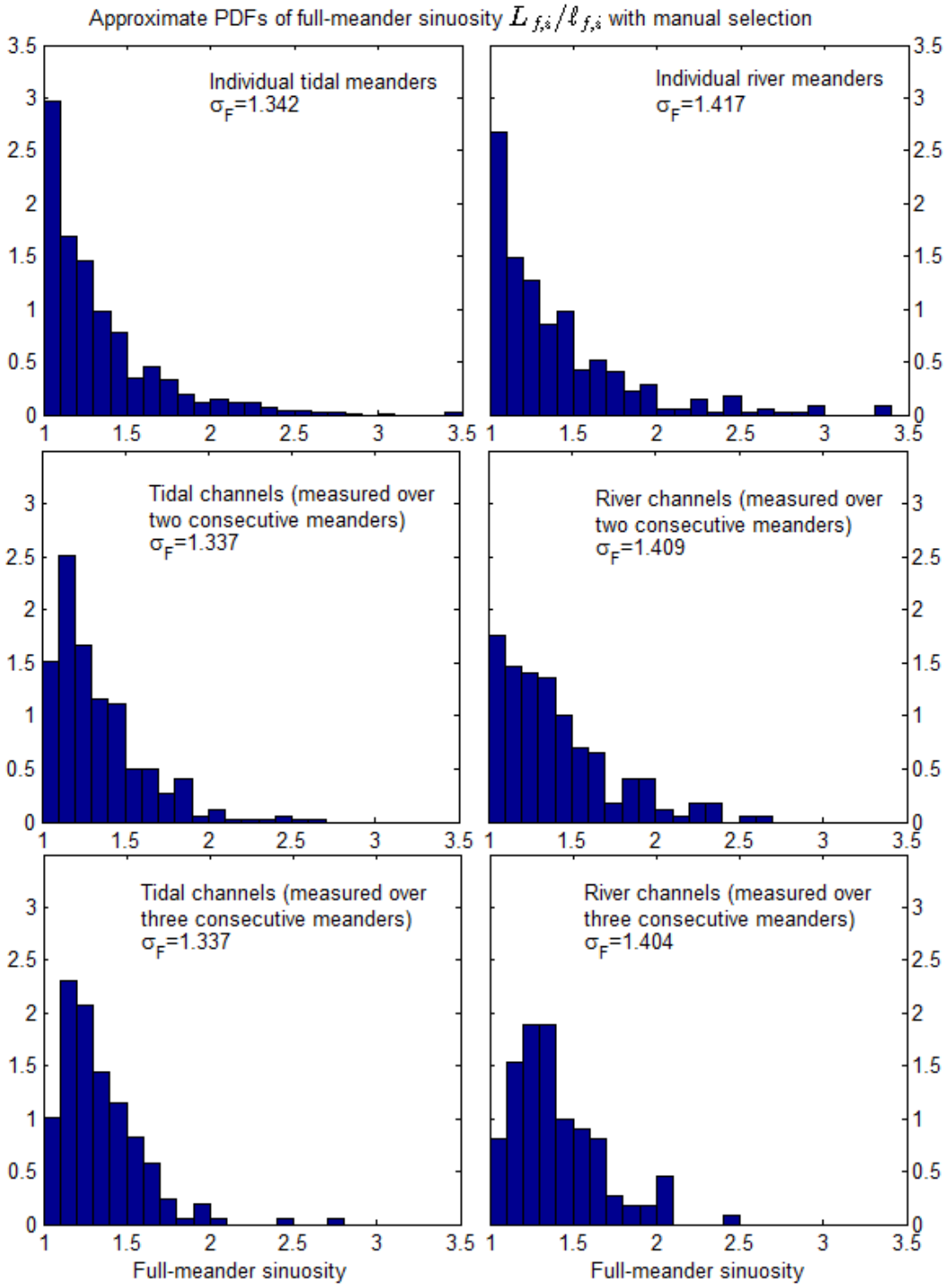

Figure 2.6: *Histograms approximating the probability density functions of full-meander sinuosity for the tidal meanders (left) and the river meanders (right).*

that these sinuosities were drawn from the same distribution.

The full-meander Cartesian length (Figure 2.7) behaves similarly to the half-meander Cartesian length, displaying a positive correlation with width for both types of channels. For the individual tidal meanders, the best-fitting power law function is $\ell_f = (9.868 \pm 1.289)W^{0.963\pm0.025}$. When we average our measurements over two and then three consecutive meanders, the coefficient maintains a similar value: 9.986 ± 1.768 for two meanders and 9.718 ± 2.229 for three meanders. The power also remains very near to one in the two- and three-meander cases. For the individual river meanders, the fitted power law is given by $\ell_f = (7.578 \pm 2.189)W^{1.090\pm0.053}$; averaging values over two and three meanders increases the coefficient to 7.623 ± 2.773 and 7.754 ± 3.288, respectively. The power in the two- and three-meander river channel fits also remains close to one. We observe that the tidal meanders consistently display larger values of ℓ_f than the river meanders for a given width (as suggested by the larger coefficients and approximately linear powers), although the error range on the coefficients could allow equal values for the tidal and river meanders.

Our results regarding the full-meander intrinsic length are displayed in Figure 2.8. Once again, the meander wavelength is positively correlated with the channel width in both the tidal and river cases, and the power law relations are very nearly linear. For the individual tidal meanders, the fitted power law function is given by $L_f = (13.438 \pm 1.925)W^{0.953\pm0.027}$, whereas for the individual river meaners, we obtain $L_f = (8.792 \pm 2.954)W^{1.123\pm0.060}$. When we measure the same variables over two and three meanders, the tidal channel coefficients change to 13.659 ± 2.599 and 13.604 ± 3.334, respectively; the powers on these equations remain near one. For the river meanders, the two-meander measurements have a fitted coefficient of 8.827 ± 3.747, and the three-meander measurements have a coefficient of 9.079 ± 4.429. Once again, we observe that the tidal channels display a longer wavelength than the river meanders, although there is overlap in the error ranges such that we could obtain the same values in both the tidal and fluvial environments.

Histograms of the metric V suggest that the values are not normally distributed in either the tidal or the fluvial case. Consequently, we apply a one-sided Wilcoxon rank-sum test to compare the two distributions. We begin with the null hypothesis that the median

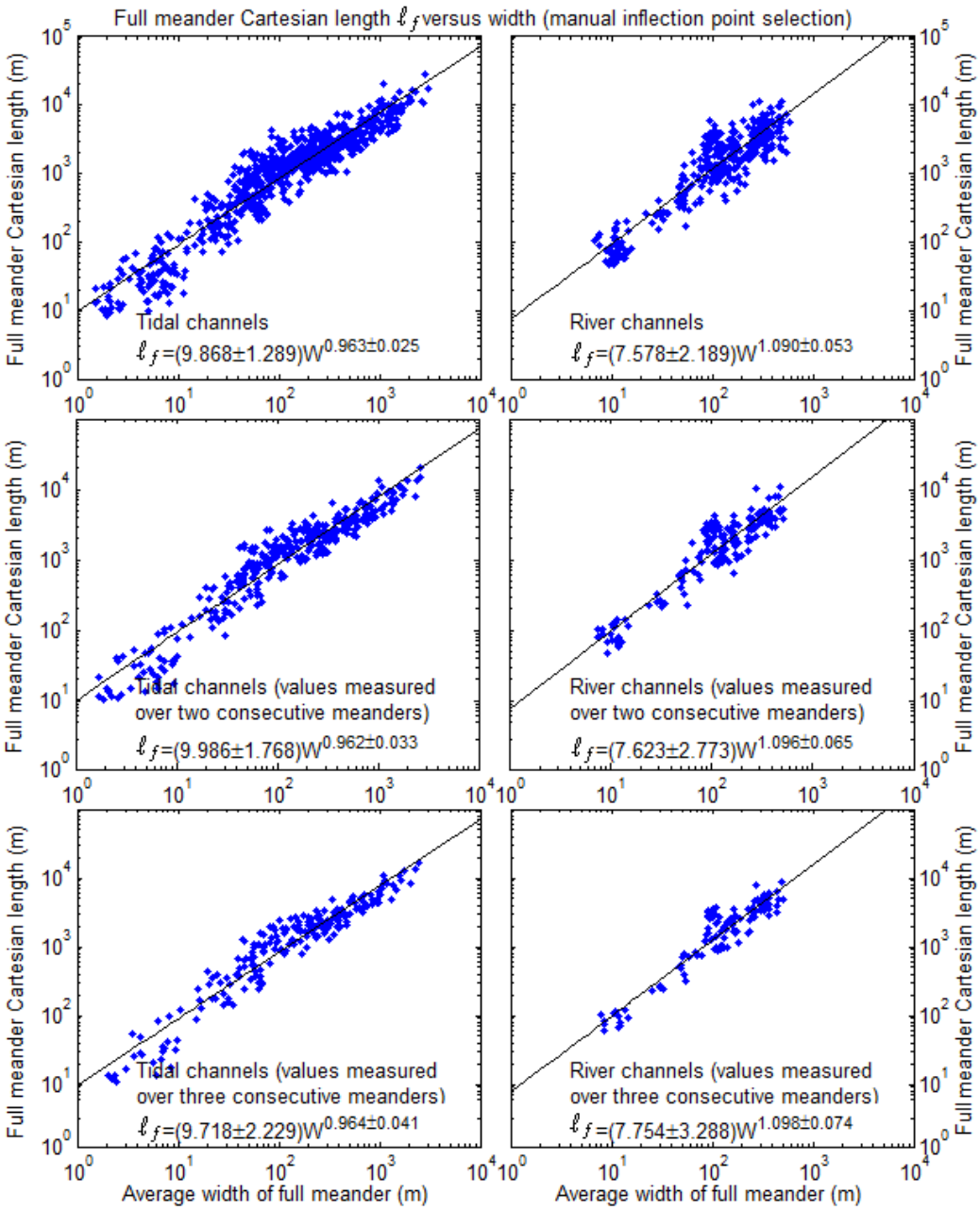

Figure 2.7: *Plot of full-meander Cartesian length ℓ_f versus the average width of the meander for the tidal meanders (left) and the river meanders (right). The power law trendlines were obtained by log-transforming the data and applying linear least squares.*

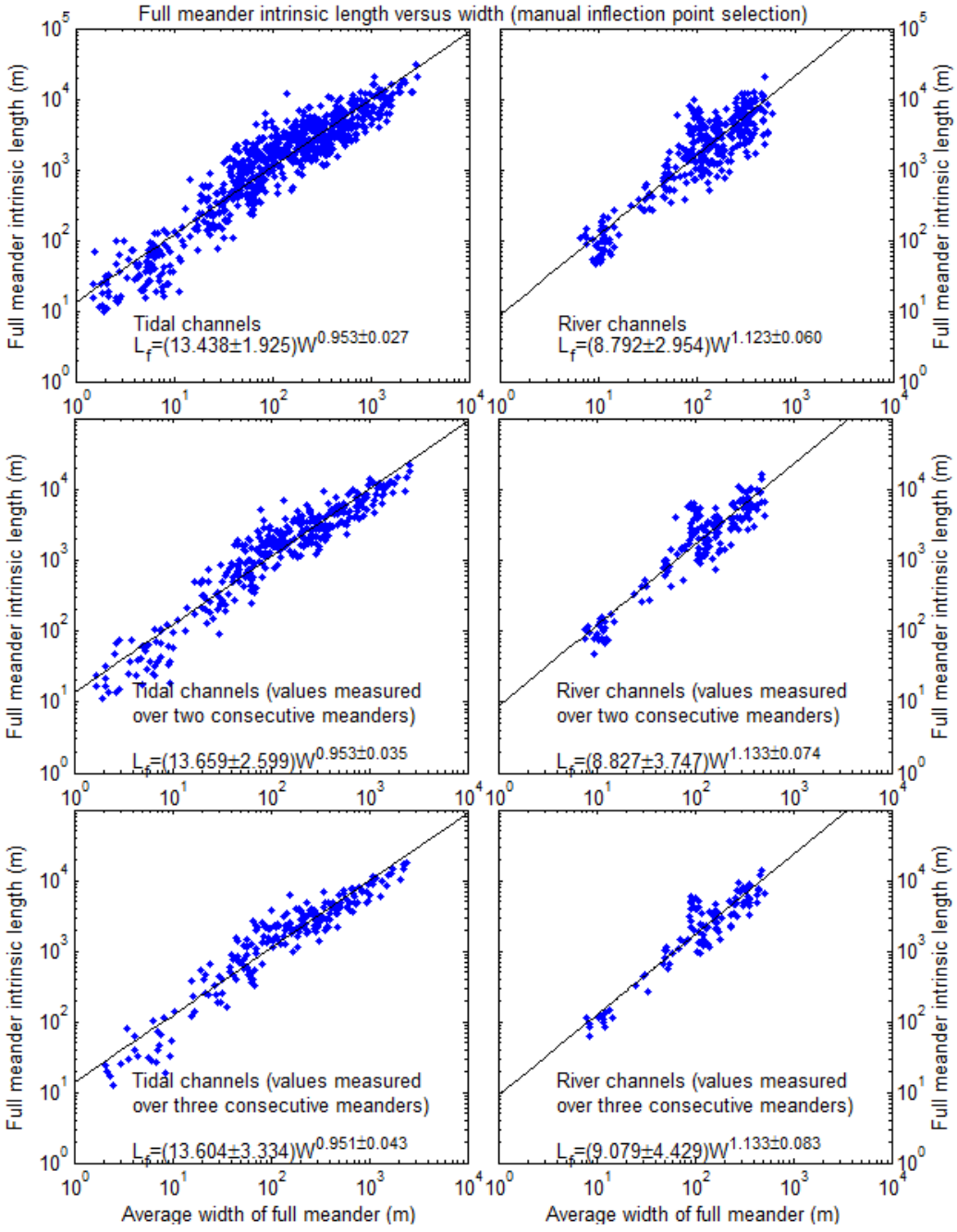

Figure 2.8: *Plot of full-meander intrinsic length L_f versus the average width of the meander for the tidal meanders (left) and the river meanders (right).*

value of V_{tidal} is equal to the median value of V_{river}; our alternate hypothesis is that the median value of V_{tidal} is greater than the median value of V_{river}. We are primarily concerned with the curvature of the "meanders", so it seems appropriate to consider only those meanders which exceed a given sinuosity value. A channel is considered "meandering" if its sinuosity exceeds 1.5; however, this value was arbitrarily chosen and does not reflect physical differences between the channels (Charlton, 2008, p. 138). As such, we present the results of the test for a variety of sinuosities in the first four columns of Table 2.2.

Table 2.2: *Results of Wilcoxon rank-sum test comparing the median values of V_{tidal} and V_{river} for varying cutoff "meander" sinuosities.*

		$H_0 : \tilde{V}_{\textbf{tidal}} = \tilde{V}_{\textbf{river}}$ $H_a : \tilde{V}_{\textbf{tidal}} > \tilde{V}_{\textbf{river}}$		$H_0 : \tilde{V}_{\textbf{tidal}} = \tilde{V}_{\textbf{river}}$ $H_a : \tilde{V}_{\textbf{tidal}} < \tilde{V}_{\textbf{river}}$	
Cut-off sinuosity	**Number of samples**	$\mathcal{P}$	**Reject null hypothesis at $\alpha = 5\%$?**	$\mathcal{P}$	**Reject null hypothesis at $\alpha = 5\%$?**
Individual meanders					
None	1079	1.000	No	1.92×10^{-7}	Yes
1.1	770	0.9999	No	9.77×10^{-5}	Yes
1.2	594	0.9998	No	1.74×10^{-4}	Yes
1.3	443	0.9990	No	9.84×10^{-4}	Yes
1.4	341	0.9932	No	0.0068	Yes
1.5	250	0.9531	No	0.0471	Yes
Two consecutive meanders					
None	513	0.9996	No	4.47×10^{-4}	Yes
1.1	431	0.9996	No	3.87×10^{-4}	Yes
1.2	320	0.9996	No	3.56×10^{-4}	Yes
1.3	239	0.9899	No	0.0101	Yes
1.4	176	0.9331	No	0.0673	No
1.5	121	0.6345	No	0.3675	No
Three consecutive meanders					
None	319	0.9545	No	0.0456	Yes
1.1	289	0.9629	No	0.0372	Yes
1.2	224	0.8446	No	0.1559	No
1.3	160	0.7746	No	0.2265	No
1.4	112	0.2916	No	0.7105	No
1.5	92	0.1364	No	0.8660	No

Considering that the Wilcoxon test prevents us from rejecting the null hypothesis for any combination of sinuosity and number of meanders analyzed, we performed a second one-

sided Wilcoxon rank-sum test. Our null hypothesis is again that the median value of V_{tidal} is equal to the median value of V_{river}, but we now consider the alternate hypothesis that the median value of V_{tidal} is less than the median value of V_{river}. The results of this test are displayed in the last two columns of Table 2.2. For the individual meanders, we reject the null hypothesis at all values of the cut-off sinuosity for meandering; that is, we conclude that the second Fourier harmonic is comparatively higher in the fluvial meanders than in the tidal meanders. However, when we measure values over two or three consecutive meanders, we can only reject the null hypothesis when we include low-sinuosity reaches in the data set. Raising the cut-off sinuosity value for meandering prevents us from rejecting the null hypothesis that the second Fourier harmonic has equal relative strength in both settings.

We now address the results pertaining to the taper of tidal channels relative to their mouths. We observe a positive correlation between the measured width of the channel mouth $\hat{W}(0)$ and the e-folding length L_b regardless of which model we select for the connected channels, as shown in Figure 2.9. However, when we log-transform our data and use the reduced major axis algorithm to calculate separate power-law trendlines for the blind and connected channels, we find that the relation between e-folding length and mouth width is of a lower power for the connected channels (possible powers range between 0.521 and 1.121, depending on the model selected) than for the blind channels (power of 1.296 ± 0.323). The break in slope between the two types of channels is more prevalent under the assumption that the connected channels have a width of zero upstream, but it is also present when we assume that the connected channels have nonzero upstream width.

To compare our results with those obtained by Davies and Woodroffe (2010), we also calculated the following correlation coefficients for the full set of data points: Pearson's correlation coefficient R^2, which indicates the linearity of any trend in the data; Spearman's ranked correlation coefficient ρ, which indicates how strongly monotonic the data is; and Kendall's correlation coefficient τ, which also measures monotonicity. These values are reported in Table 2.3 along with the p-value for each coefficient, which gives the probability of no correlation existing. Our data are notably more linear than the results reported by Davies

and Woodroffe (2010), and the strength of the monotonicity is much greater. We perform a similar analysis of the relationship between $\hat{W}(0)$ and the shape parameter S_b, with the results displayed in Figure 2.10 and Table 2.4. Our data display significantly more scatter than was previously reported, regardless of which model we select for the connected channels. Moreover, our values of ρ and τ indicate that there is a negative correlation between the variables, which is stronger under the assumption that the connected channels have a nonzero width at infinity. Davies and Woodroffe (2010) also reported a negative correlation for these variables.

Table 2.3: *Correlation between the width convergence length L_b and the measured mouth width $\hat{W}(0)$ based on the data from this paper and as reported by Davies and Woodroffe (2010).*

	This study (model 1)	This study (model 2 or 3)	Davies & Woodroffe (2010)
R^2	0.345	0.416	0.0000173
	$p = 1.1 \times 10^{-10}$	$p = 3.32 \times 10^{-13}$	p=0.971
ρ	0.809	0.735	0.2274
	p=0	p=0	p=0.044
τ	0.619	0.546	0.148
	$p = 4.76 \times 10^{-20}$	$p = 5.99 \times 10^{-16}$	p=0.053

Table 2.4: *Correlation between the shape parameter S_b and the measured mouth width $\hat{W}(0)$ based on the data from this paper and as reported by Davies and Woodroffe (2010).*

	This study (model 1)	This study (model 2 or 3)	Davies & Woodroffe (2010)
R^2	0.124	0.107	0.683
	p=0.000302	p=0.000832	$p < 2.2 \times 10^{-16}$
ρ	-0.377	-0.515	-0.539
	$p = 0.00011$	$p = 5.64 \times 10^{-8}$	$p = 4.61 \times 10^{-7}$
τ	-0.299	-0.369	- 0.3878
	$p = 9.27 \times 10^{-6}$	$p = 4.75 \times 10^{-8}$	$p = 4.21 \times 10^{-7}$

Assuming that the connected channels display a nonzero width at infinity, we observe a positive correlation between the fitted width at infinity and the measured width at the channel mouth (Figure 2.11). The trendline through these points obtained by log-transforming the data and using the reduced major axis algorithm is a power law of power 0.977 ± 0.158; that is, an essentially linear relationship. Clearly, the width at infinity is not correlated with channel mouth width if we assume that the connected channels decay to a width of zero at

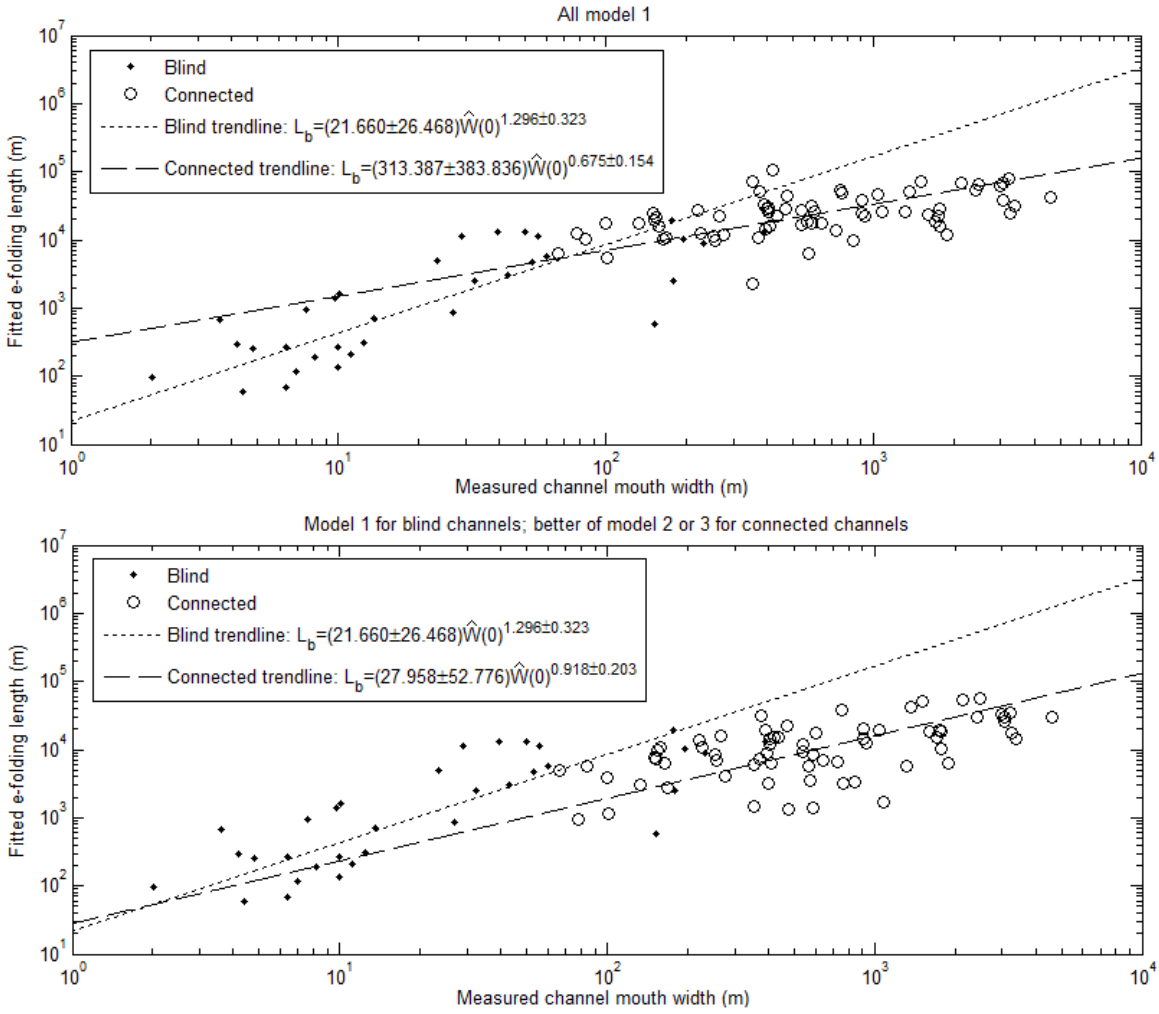

Figure 2.9: *The e-folding L_b plotted against the measured mouth width $\hat{W}(0)$. This plot includes data from both connected and dead-end channels. In the upper frame, we assume that the connected channels have a width of zero at infinity; in the lower frame, we assume that the connected channels have a positive nonzero width at infinity.*

infinity.

2.4 Discussion

2.4.1 Differences between tidal and fluvial meanders

Our meander metrics suggest that there are certain differences in the planform geometry of tidal channels versus river channels on the Ganges-Brahmaputra-Jamuna Delta. Most

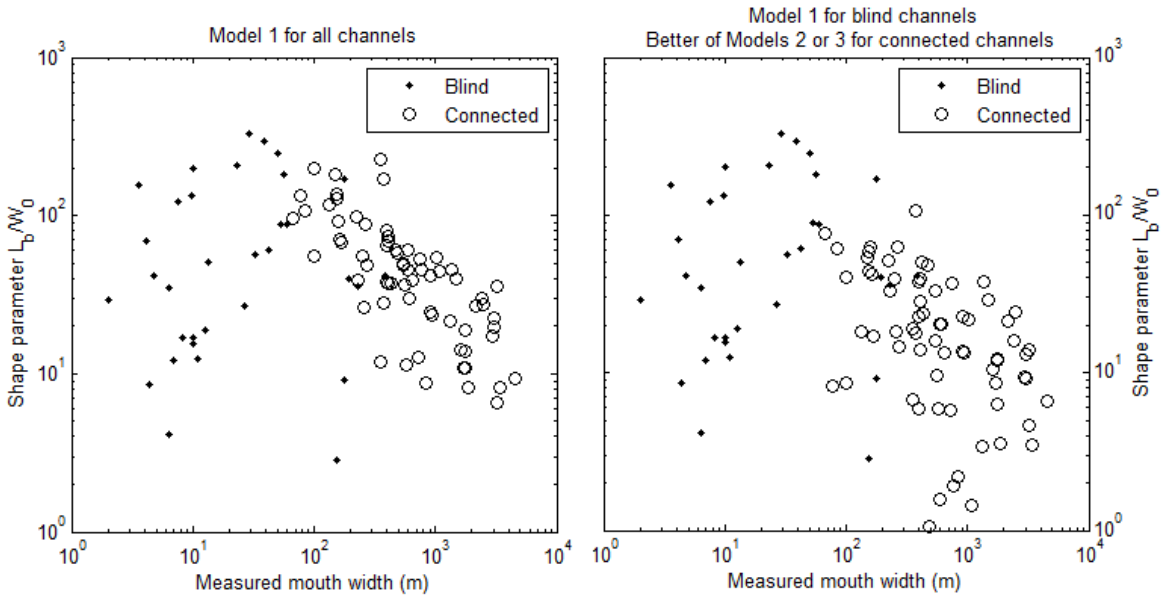

Figure 2.10: *The shape parameter S_b plotted against mouth width $\hat{W}(0)$. In the left plot, we assume that the connected channels have a width of zero at infinity. In the right plot, we assume that the connected channels have a positive nonzero width at infinity.*

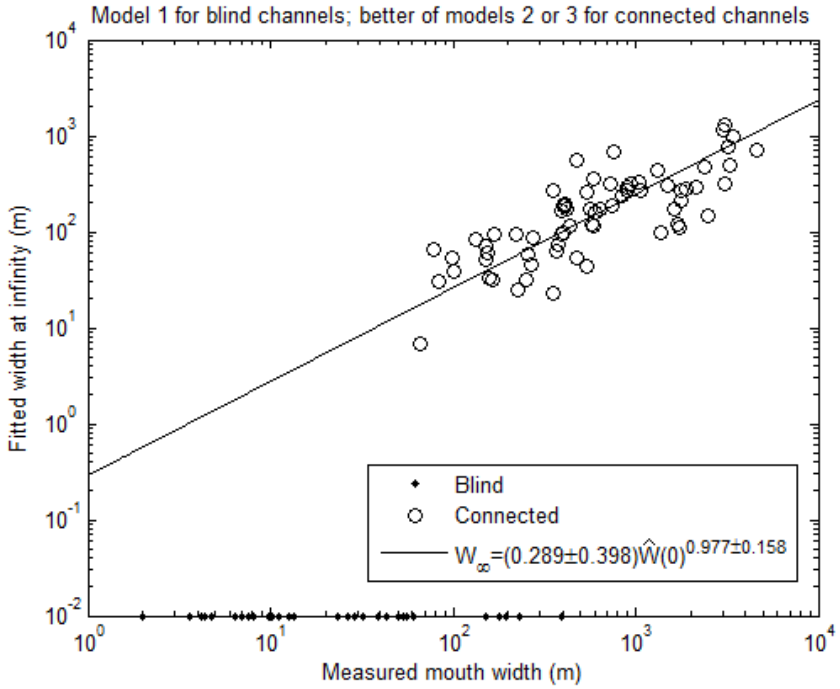

Figure 2.11: *The fitted width at infinity W_∞ plotted against mouth width $\hat{W}(0)$. In this plot, we assume that the connected channels have a nonzero width at infinity. Note that we have assigned the blind channels an arbitrary value of $W_\infty = 0.01$ m to force them to appear on the plot.*

notably, we observe differences in the distribution of full meander sinuosities and in the skewness of the meanders in physical space. Our data also suggest that the tidal meanders display, on average, longer intrinsic and Cartesian wavelengths than the river meanders, although the confidence intervals for these measurements overlap in almost all cases. In the following paragraphs, we discuss the primary differences between tidal and fluvial meanders and present possible physical explanations for why these differences occur.

A number of factors can influence channel sinuosity, including floodplain slope and resistance (Lazarus and Constantine, 2013), tectonics (Petrovszki *et al.*, 2012; Kumar *et al.*, 2014), and channel engineering (*e.g.*, Urban and Rhoads, 2003). Although our study area is tectonically active, it seems unlikely that tectonic effects would be isolated to only the tidal or only the fluvial setting. Likewise, as the effect of engineering is generally to straighten the channel, we would expect those channels in the highly populated areas of the delta–the fluvial channels–to be *less* sinuous than the tidal channels if the difference in sinuosity were an anthropogenic effect. We also have no evidence suggesting that the fluvial channels systematically display a lower slope than the tidal channels. Consequently, the most reasonable explanation for the fluvial channels' higher sinuosities is differing flow resistance on the floodplain. The abandoned channels characterizing the non-tidal upper delta plain (Coleman *et al.*, 2008) likely contain clay plug deposits that resist erosion when the channel reoccupies its former position; an effect of this increased floodplain resistance would be to increase the sinuosity of the river channels. In contrast, we have little evidence of channel migration in the tidal region of the delta, which is consistent with prior observations that tidal channels have extremely low migration rates (*e.g.*, Solari *et al.*, 2002). Indeed, we observe only one oxbow lake forming throughout the entire Sundarbans region, as shown in Figure 2.12. It is certainly possible that the dense mangrove vegetation in the Sundarbans conceals evidence of more rapid channel migration, but we note that migration indicators such as scroll bars are clearly visible in Google Earth images of other densely vegetated floodplains (*e.g.*, the Amazon Rainforest).

The preference for low asymmetry values displayed by the tidal channels in our study

Figure 2.12: *Image of the only oxbow lake observed in the Sundarbans. The relative absence of meander cutoffs in this region suggests very low rates of channel migration. Google Earth image of Channel 16, centered at 22.189353° N, 89.700374° E. Imagery date 1/31/10.*

area is likely a direct consequence of bidirectional flow. Displacement of the ebb current relative to the flood current (Ahnert, 1960; Dalrymple *et al.*, 2012, p. 93; Hughes, 2012, p. 286) shifts the location of maximum erosion within the channel, preventing any net meander migration that would allow asymmetric meanders to form (Solari *et al.*, 2002). The tidal half-meanders are, on average, slightly upstream skewed, which indicates an ebb-dominated environment (*e.g.*, Fagherazzi *et al.*, 2004). A surprising aspect of our sinuosity measurements is that although the river meanders display more extreme skewness values than the tidal meanders, the number of upstream-skewed fluvial meanders is nearly balanced by the number of downstream-skewed meanders. This is contrary to the theory that fluvial meanders should be preferentially upstream skewed (Parker *et al.*, 1983; Marani *et al.*, 2002). We initially wondered whether we had inadvertently misinterpreted the flow direction of one or more of the river channels during digitization, which would be an easy mistake to make given the complex drainage patterns in Bangladesh. However, after revisiting each of these channels in Google Earth, we are confident that we have accurately identified the downstream and upstream directions for every channel, and that the distribution of asymmetries displayed in Figure 2.5 is not in error.

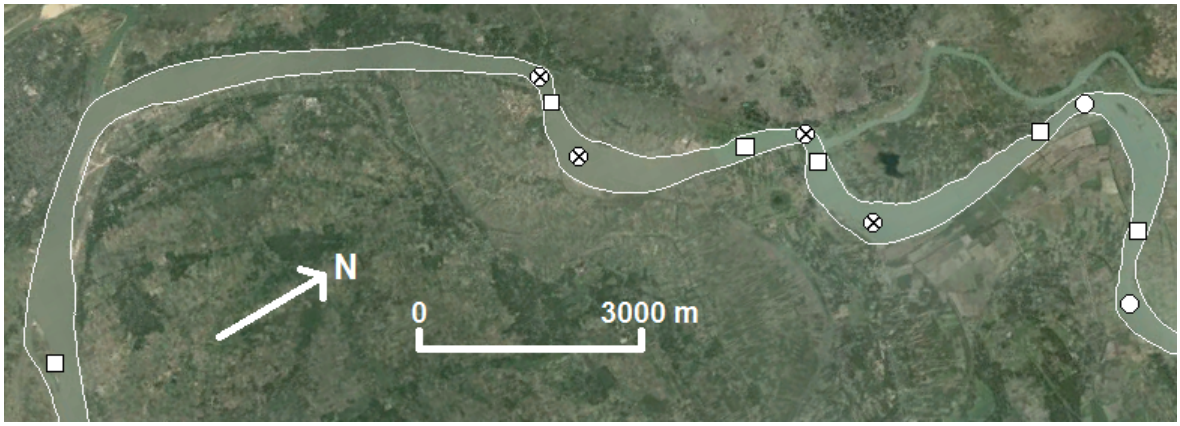

Figure 2.13: *A possible explanation for the observed distribution of fluvial asymmetry coefficients. The image shows a stretch of the Hooghly River in which the downstream skewed half meanders alternate with upstream skewed half meanders. Squares indicate inflection points; circles indicate meander apices. The crossed circles are those that adhere to the pattern of interest; note that not all meanders display this pattern. Google Earth image centered at 23.718617°N, 88.190672°E. Imagery date 2/9/2014.*

A possible explanation for the observed distribution of the fluvial asymmetry coefficients is the qualitative observation that a strongly downstream skewed meander is often immediately followed by a strongly upstream skewed meander, as displayed in Figure 2.13. However, this pattern is not present everywhere along the channels, and further quantitative study is necessary to determine (1) whether the observed pattern is responsible for the unexpected asymmetry distribution, and (2) if so, what physical properties of the flow produce the alternating downstream and upstream skewness. Physical explanation notwithstanding, we note that even "upstream skewed" river channels often contain a fairly high percentage of downstream skewed meanders (personal communication with C. Paola, July 2014), and that certain rivers often cited as quintessential upstream skewed channels, such as the Beaver River in Alberta, Canada (*e.g.*, Parker *et al.*, 1983; Gutierrez and Abad, 2014), are bedrock-influenced.

The tidal channels in our study area display full-meander intrinsic wavelengths consistent with those reported by Solari *et al.* (2002) and Marani *et al.* (2002). The coefficient on the best-fitting power law for our full-meander Cartesian wavelengths is approximately 10 in the tidal case, which is similar to the value of 11 obtained by Leopold and Wolman (1960)

for meanders occurring in a variety of environments. In contrast, our fluvial intrinsic and Cartesian wavelengths are unexpectedly low. Solari *et al.*'s (2002) work suggests that the fluvial meanders, rather than the tidal meanders, should display the larger intrinsic wavelength. Likewise, our power law coefficient of ~ 7.6 for the fluvial Cartesian wavelengths is noticeably lower than Leopold and Wolman's (1960) value, although it does fall within the range of 7 to 15 reported by Leopold and Wolman (1957). Prior field studies suggest that a channel's Cartesian wavelength should be positively correlated with mean annual discharge, mean annual flood, and with bedload grain size (Schumm, 1967). Given that discharge and width are also positively correlated (Leopold and Maddock, 1953), we do not expect to gain much insight into this problem by examining discharge differences between the two types of channels. Our results are also inconsistent with the hypothesis that variations in grain size control the wavelength of the channels; if this were so, we would expect the sandy river channels (Coleman, 1969; Goodbred and Kuehl, 2000; Small *et al.*, 2009) to display a longer wavelength than the channels in the silt- and clay-dominated tidal region (Goodbred and Kuehl, 2000). It is possible that the meander wavelengths of the tidal and fluvial channels are controlled by fundamentally distinct processes (*e.g.*, Whiting and Dietrich, 1993), and further study of flow and sediment transport processes in these environments may be necessary to determine why the tidal channels display a longer wavelength than the fluvial channels.

Then again, the fluvial channels' shorter wavelength may be a consequence of noise in the digitized channels. Although we put great effort into digitizing the true bankfull position of each channel, this task was far more straightforward in the unpopulated Sundarbans, where embankments, cultivation, and vegetation removal are absent. It is possible that human modifications to the fluvial channels resulted in the selection of an excessive quantity of inflection points, decreasing the apparent wavelength of the channels in this environment. Consequently, we cannot reject the possibility that variations in meander wavelength are not a true difference between tidal and fluvial channels.

Before closing our discussion of the differences between tidal and fluvial meanders, we

wish to comment on a negative but nevertheless significant result. Our data indicate that there is no configuration of threshold sinuosity and number of meanders analyzed for which the second curvature harmonic is greater in the tidal meanders than the fluvial meanders on the Ganges-Brahmaputra-Jamuna Delta. However, we do observe that the second curvature harmonic is greater in the fluvial channels when we include low sinuosity values and/or isolated meanders in our analysis. This directly contradicts Marani *et al.*'s (2002) result that tidal meanders display relatively higher values of the second curature harmonic. The implications of this result are twofold: first, it appears that there is no statistical difference between the curvatures of tidal and fluvial meanders in most cases, which is surprising considering that the two types of meanders form due to two distinct flow patterns. Second, our observations imply that the Kinoshita equation (Equation 2.1) may contain insufficient terms to represent the geometry of fluvial meanders, considering that there are situations in which the second harmonic is non-negligible in fluvial channels.

2.4.2 Properties of tidal channel mouth flaring

Our channel width data represent a moderate departure from the tidal channel geometries reported in the literature. Specifically, we have made the following observations:

1. There is a positive correlation between a channel's measured mouth width $\hat{W}(0)$ and its e-folding length L_b, although appreciable scatter in the data must be noted (Figure 2.9). In either case, our data display a much stronger correlation betweenL_b and $\hat{W}(0)$ than observed by Davies and Woodroffe (2010), who report a very weak positive correlation.

2. We observe a weak negative correlation between a channel's measured mouth width and the funnel-shape parameter $S_b = L_b/W_0$ (Figure 2.10), whereas Davies and Woodroffe (2010) report a stronger negative correlation. Note that this negative correlation implies that the larger-mouthed channels are more funnel shaped than the smaller-mouthed channels.

3. On average, the blind channels display higher values of the shape parameter S_b than

the connected channels (Figure 2.10). This appears to contradict the prior assertion by Savenije (2005) that the blind channels should be more strongly funnel-shaped (*i.e.*, display smaller values of S_b) than those receiving upstream discharge.

4. For the connected channels, there is a positive correlation between mouth width $\hat{W}(0)$ and the upstream width W_∞ (Figure 2.11), provided that we assume that the connected channels have a nonzero width at infinity. We are unaware of any comparable results in the literature, as previous results address only blind channels.

To explain the observed phenomena, we considered several hypotheses regarding possible controls on a channel's e-folding length, which we discuss below. In the following paragraphs, we assume (1) that the upstream width W_∞ serves as a proxy for the channel-forming fluvial discharge, and (2) that the e-folding length of the channel is some fraction of the total length of tidally-influenced channel.

Hypothesis 1: L_b is a function of the regional tidal range

We first consider whether our observed e-folding lengths could be controlled by the regionally-averaged delta geometry and tidal prism. This hypothesis hinges on the idea that a channel's shape is driven exclusively by external boundary conditions–in this case, tidal range. Indeed, Davies and Woodroffe (2010) predict, using the St. Venant equations, that two tidal channels with identical e-folding lengths, bathymetries, and boundary conditions but different mouth widths (Figure 2.14) will display identical flow depths and cross-sectionally averaged velocities at each point along the channel axis. This implies that either channel geometry can represent an equilibrium morphology for the channel.

To test this hypothesis, we estimated the slope of the delta along several approximately north-south transects between the Ganges River and the coast, obtaining values ranging from 5.0×10^{-5} to 7.6×10^{-5}. Neglecting local topographic variations and assuming that the tidal range is uniform along the coast, we approximate the horizontal tidal range as the vertical tidal range divided by the delta slope. As this distance is independent of channel mouth width, it plots as a horizontal line in Figure 2.15. Under our initial assumptions, the e-

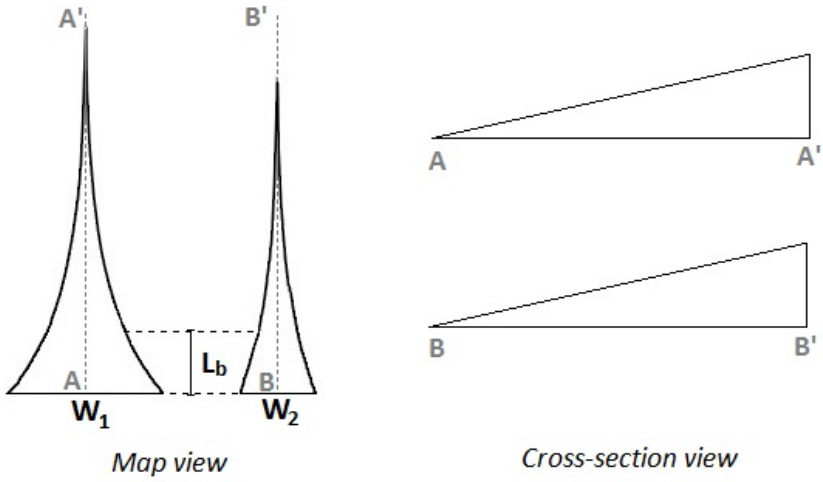

Figure 2.14: *Two channels meeting the criteria for Davies and Woodroffe's (2010) analysis. The two channels have identical e-folding lengths and bed profiles; the only geometrical difference is the mouth widths W_1 and W_2. The St. Venant equations predict that the two channels will have identical flow depths and average velocities at every transverse cross-section through the channels.*

folding length is some fraction of the initial tidal penetration distance, but it nevertheless remains independent of the mouth width. Consequently, this hypothesis does not explain the observed correlation between mouth width and e-folding length displayed by our data.

Hypothesis 2: L_b is a function of the upstream discharge

Alternately, we consider whether the upstream discharge could be controlling the e-folding length of the channels. Using the upstream width W_∞ as a proxy for the channel-forming fluvial discharge, consider an axis system in three dimensions where x is parallel to the coastline (east-west in the Ganges-Brahmaputra case), y is perpendicular to the coastline and parallel to the tidal flow (north-south), and z represents elevation. Assuming that fluvial channels maintain an approximately constant aspect ratio, we obtain the following relationship:

$$c \cdot L_b(\text{meters in } y) = \frac{D_\infty(\text{meters in } z)}{S_0\left(\frac{\text{meters in } z}{\text{meters in } y}\right)} \propto \frac{W_\infty(\text{meters in } x)}{S_0\left(\frac{\text{meters in } z}{\text{meters in } y}\right)} \tag{2.9}$$

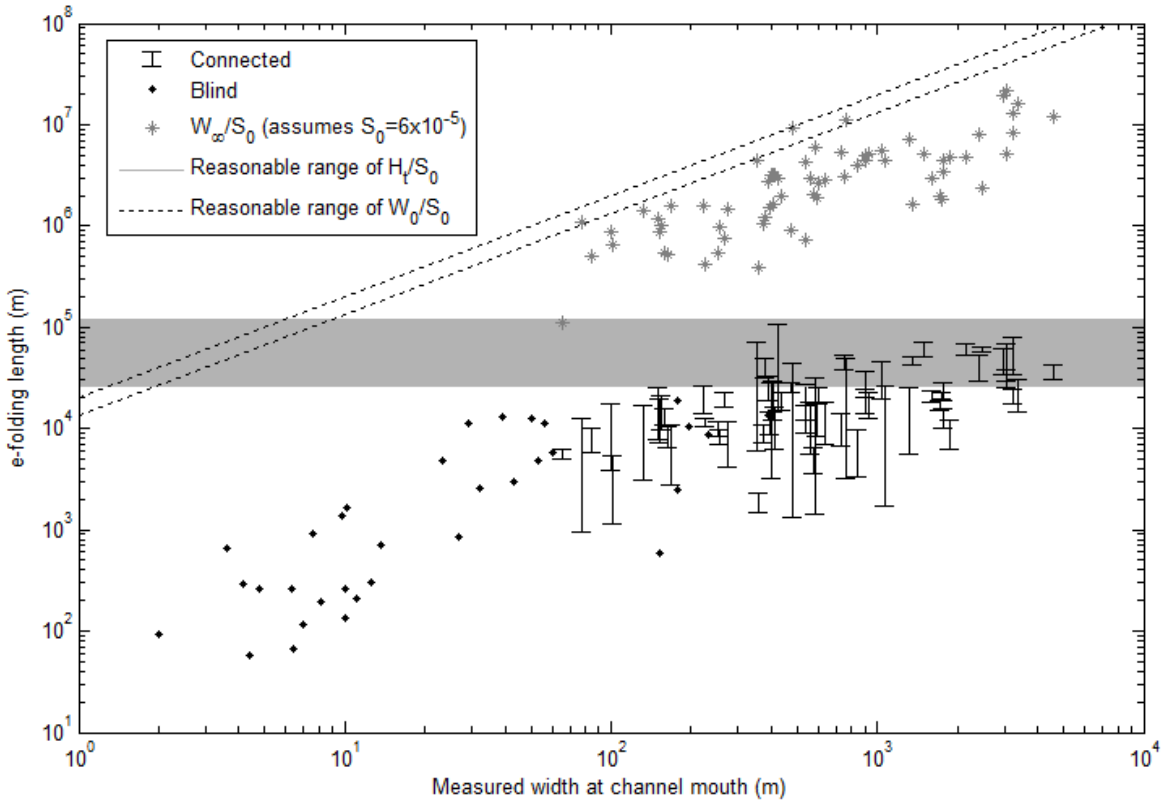

Figure 2.15: *Plot of e-folding length versus mouth width overlain with plots of expected shape under each of our three hypotheses. The bars for the connected channels indicate the minimum and maximum possible e-folding lengths for the channel, obtained by assuming a zero and a nonzero upstream width at infinity.*

where D_∞ is the depth corresponding to W_∞ and $c \geq 1$ is some multiplicative constant. Dividing the upstream width of the connected channels by an average delta slope of 6×10^{-5} and including these points in Figure 2.15, we observe that the slope of the new ponts is greater than the slope of the fitted values of L_b with respect to $\hat{W}(0)$ for the connected channels. On a log-log plot, a steeper slope indicates a greater power in the power law relationship between two variables. It is thus unlikely that the upstream discharge is the exclusive control on the channels' e-folding length. Observe, however, that the points corresponding to the upstream discharge display a similar slope to that of the blind channels in Figure 2.15.

Hypothesis 3: L_b is a function of the local tidal prism

Using a similar argument to that preceding Equation 2.9, we obtain a relationship of the form

$$c \cdot L_b(\text{meters in } y) = \frac{D_0(\text{meters in } z)}{S_0\left(\frac{\text{meters in } z}{\text{meters in } y}\right)} \propto \frac{W_0(\text{meters in } x)}{S_0\left(\frac{\text{meters in } z}{\text{meters in } y}\right)} \tag{2.10}$$

where D_0 is the mean depth at the channel mouth. Substituting the minimum and maximum possible values for S_0 into this equation and plotting the results in Figure 2.15, we once again observe a plot similar in shape to our data from the blind channels, but steeper in slope than the data from the connected channels. This suggests that the tidal prism could be setting the e-folding length for the blind channels. However, the limitation to this explanation is that the proportionality between D_0 and W_0 is less well-established than in the fluvial case. It is thus unclear whether the mouth width W_0 is an appropriate proxy for the tidal prism of the channel. Past studies have established that the tidal mouth area A_0 is related to the tidal prism Ω by a relationship of the form $A_0 = k\Omega^n$, where k and n are empirical constants (*e.g.*, O'Brien, 1931; Gao and Collins, 1994). However, models of tidal channels disagree on whether the tidal prism is accommodated exclusively by an increase in width (Savenije, 2005) or by some combination of increased width and average depth (Lanzoni and Seminara, 2002).

For reasons discussed in the Supporting Information (Chapter 3 of this thesis), we are hesitant to use Google Earth as a reliable source of channel bed elevation data, which could be used to elucidate a possible relationship between width and depth at the mouths of tidal channels. Bathymetric data from other sources is extremely limited for channels in Bangladesh. Using navigational charts of the coastline (U.S. Defense Mapping Agency, 1994), we estimated aspect ratios at the mouths of four large tidal channels in the Sundarbans (Table 2.5). These four data points do not suggest a correlation between channel width and depth, but we clearly need more measurements before we can ascertain whether any trend exists. However, soundings on these charts do not extend very far inland and do not include the smaller channels, making it difficult to compile a sufficiently large dat aset from existing sources.

Table 2.5: *Aspect ratios at the mouths of four large tidal channels in the Sundarbans, as measured from navigational charts by the U.S. Defense Mapping Agency (1994).*

Channel name	**Mouth Width**	**Average depth at mouth**	**Aspect ratio**
Matla River	12,300 m	8 m	1540
Harinbhan River	6,600 m	6.5 m	1020
Raimangal River	9,800 m	6 m	1630
Pusur River	12,100 m	6 m	2020

Other authors have attempted to relate channel mouth geometry to the channel-forming discharge Q rather than to the tidal prism. We note that tidal prism and the time-dependent discharge are related by $\Omega = \int_0^{T_{1/2}} Q(t)dt$, where $T_{1/2}$ is half the tidal period. The equation for discharge is (after Williams *et al.*, 2002)

$$Q = WDv \tag{2.11}$$

where v is the cross-sectionally averaged velocity. Basic algebra then implies that

$$Q = aQ^b \cdot cQ^f \cdot kQ^m \tag{2.12}$$

for any constants a, b, c, f, k, and m such that $ack = 1$ and $b + f + m = 1$. Equating Q in Equations 2.11 and 2.12 then gives us

$$W = aQ^b \qquad D = cQ^f \qquad v = kQ^m \ . \tag{2.13}$$

Numerical modeling and field measurements have provided remarkably consistent values for the exponents in these equations (Table 2.6), with mean values of $b = 0.73$, $f = 0.23$, and $m = 0.04$. Williams *et al.* (2002) note that these formulae apply only to mature channels; young channels that have not yet reached an equilibrium geometry will be much deeper than they are wide. Assuming that the relationships hold for the tidal channels in our study area implies that the width-to-depth ratio at a channel mouth should be $\frac{a}{c}Q_0^{b-f} \approx \frac{a}{c}Q_0^{0.5}$. Nevertheless, in the absence of additional data, we cannot confirm that the ratio $\frac{a}{c}$ is constant over all channels.

Table 2.6: *Values of b, f, and m as compiled by Allen (2000).*

Study	**Model or field data?**	b	f	m
Langbein (1963)	Model	0.72	0.23	0.05
Woldenberg (1972)	Model	0.727	0.227	0.045
Langbein (1963)	Field	0.72	0.22	0.06
Myrick and Leopold (1963)	Field	0.77	0.23	0.00
Pestrong (1965)	Field	0.70	0.30	0.00
Redfield (1965)	Field	0.74	0.17	0.09
Geyl (in Woldenberg, 1972)	Field	0.73	0.23	0.04
Mean		**0.73**	**0.23**	**0.04**

Although the proposed relationship between local tidal prism and e-folding length explains the correlation between mouth width and e-folding length that we observe for the blind channels, it does not illuminate the cause of the correlation between mouth width and e-folding length for the connected channels. It also does not reconcile the differences between our data set and the results of prior studies. The previous finding that channels with non-negligible fluvial input should display a longer e-folding length relative to those channels lacking a fluvial connection (Savenije, 2005) suggests that the tidal prism, tentatively scaling with the mouth width, cannot be the exclusive control on a channel's e-folding length. Moreover, this hypothesis cannot explain why large-mouthed tidal channels are more funnel-shaped than small-mouthed channels in northern Australia (Davies and Woodroffe, 2010) and to some extent in Bangladesh (Figure 2.10), although the correlation is much weaker in the Bangladesh case.

An integrated explanation for the observed correlation between L_b, W_0, and W_∞

The above paragraphs demonstrate that none of the three variables L_b, W_0, or W_∞ exerts a first-order control on the other two. Given the complexity of this natural delta system, it is not surprising that we lack a simple explanation for the observed correlation between the variables of interest. Indeed, the shape of the channels is likely a consequence of intricate relationships between tidal and fluvial processes and the sedimentary history of the system. Although available data is insufficient to address these relationships in detail, we

offer the following "thought experiment" as an example of how multiple interrelated processes could control the planform of the channels.

First, let us consider the effect of the region's 2 to 3 meters of mean annual rainfall (Shahid and Khairulmaini, 2009) on the shape of the channels. We previously assumed that those channels appearing to be "blind" in Google Earth are controlled exclusively by tidal processes, whereas the "connected" channels experience some degree of fluvial influence. But if the blind channels exist, in part, to conduct rainfall to the Bay of Bengal, there may be fewer hydrodynamic differences between the blind and connected channels than we first anticipated. Consequently, it is not unreasonable to assume that all channels in our study area have a partly fluvially-controlled geometry, and we obtain nonzero upstream widths for the "blind" channels by extrapolating along the trendline in Figure 2.11.

Suppose that two fluvial distributary channels form in the absence of tidal influence. As the geometry of these channels is strictly controlled by fluvial processes, we anticipate that the width W_∞ of the channels scales with the depth D_∞. Moreover, W_∞ and D_∞ should maintain roughly constant values in the downstream direction. Now suppose that after the shape of the channels is well-established, we introduce a constant tidal range at the mouth of both channels. Neglecting the effect of discharge onto the tidal flats, the initial horizontal tidal penetration will be greater in the deeper channel. Recalling that D_∞ is correlated with W_∞, we immediately obtain the following relationships:

$$\Omega = f_1(W_\infty) \tag{2.14}$$

and, as the e-folding length is some fraction of the tidal penetration distance,

$$L_b = f_2(W_\infty) \ . \tag{2.15}$$

With sufficient time, we expect that the cross-sectional mouth area of each channel will equilibrate to the tidal prism. As tidal prism and cross-sectional mouth area are generally

thought to be correlated, we obtain

$$A_{\text{mouth}} = f_3(\Omega) = f_4(W_\infty) \ . \tag{2.16}$$

Moreover, assuming that the mouth width W_0 scales with the mouth's cross-sectional area, Equation 2.16 implies that

$$W_0 = f_5(W_\infty) \ . \tag{2.17}$$

We thus arrive at the conclusion that the upstream channel width controls both the e-folding length (Equation 2.15) and the mouth width (Equation 2.17), which is consistent with an extrapolation of the observed trend between W_∞ and W_0 to the scale of the "blind" channels.

Implicit in our thought experiment is the idea that there are no external geologic factors controlling the shape of the channels. Specifically, we assume that the tidal channels form in homogeneous alluvium that exerts no control on flow direction or channel shape. Floodplain heterogeneities such as autocompacted sediment layers or bedrock outcrops could significantly affect our conclusions, and here, perhaps, we may explain the break in slope observed in our data in Figures 2.9 and 2.15. Bedrock influence is unlikely in the tidal portion of the Ganges-Brahmaputra-Jamuna Delta, which has up to 90 meters of sediment cover (Goodbred and Kuehl, 2000). However, low-erodibility sediment layers resulting from autocompaction processes in the tidal environment (*e.g.*, Allen, 2000) could certainly impact the morphology of at least some tidal channels. For example, Nittrauer *et al.* (2011) found that consolidated substratum in the lower Mississippi River behaves as "surrogate bedrock". Upon encountering an erosion-resistant strata, the channel would be forced to erode laterally rather than vertically in order to accommodate the tidal prism (Fagherazzi and Furbish, 2001; *c.f.* the description of Yalimbah Creek in Davies, 2011), as required by Equation 2.16. Assuming that the mouth depth scales with the mouth width in the homogeneous case, the largest channels should have the greatest likelihood of encountering a layer of autocompacted sediment and "over-widening" relative to the homogeneous equilibrium morphology. This could cause the largest channels to have shorter e-folding lengths relative to their mouth

widths, as we observe in Figures 2.9 and 2.15.

Although the largest-mouthed channels in our study area display a less pronounced increase in e-folding length than the smaller-mouthed channels, the trend is less well-defined than it is in Davies and Woodroffe's (2010) north Australia study area. However, perhaps we can reconcile these differences by considering the effect of bedrock on tidal channels. Although those authors do not explicitly mention the presence of bedrock controls on the shape of the channels, Semeniuk (1981) notes that tidal flat surfaces in King Sound, northern Western Australia, are covered by an "ephemeral sediment veneer" that is regularly stripped away. Semeniuk (1993) found that Pleistocene limestone outcrops in the Pilbara region of northern Western Australia profoundly influence the local coastal geomorphology, and that large tidal channels expose the underlying limestone. Likewise, Nott (2003) observes the limited extent of alluvial cover in the region around Darwin, Northern Territory, Australia, and Lal *et al.* (2012) report a depth to bedrock of 1 to 3.5 meters in the Daly River Basin south of Darwin. As proposed for the Bangladesh case, the presence of bedrock below a tidal channel could induce substantial widening at the mouth, so perhaps the northern Australian tidal channels are "over-widened" relative to an equilibrium mouth width in homogeneous sediment. As the largest channels would again be more likely to erode down to bedrock, this could explain why the large channels in Australia are more funnel-shaped than the small channels. Additionally, as the erosion rate of bedrock is likely lower than that of autocompacted (but not lithified) sediment, we would expect the trend to be more extreme in Australia, just as the data suggests.

Of course, our thought experiment represents an idealized and highly simplified environment that is not necessarily representative of the natural system on the Ganges-Brahmaputra Delta. For example, it is not realistic to assume that initial channel establishment occurred in the absence of tides; sedimentary structures in the Neogene Surma Group (Gani and Alam, 2003; Rahman *et al.*, 2009) indicate that the strong tidal influence in this region predates the formation of the current tidal channel network. A possible explanation is that the *ratio* of stream energy to tidal energy was likely higher in the past, given that the channels repre-

sent relict courses of the modern Ganges River. The considerable scatter in our data likely reflects the complex interplay of processes controlling the system, in contrast to the simple explanation we have presented here.

The validity of our argument rests on two key assumptions: (1) for a tidal channel formed on homogeneous substrate, the width of the mough scales with the depth at the mouth, and (2) that tidal channels in northern Australia are at least partly bedrock-controlled, limiting vertical erosion to a greater degree than in unlithified sediment. Presently-available data does not allow us to adequately address the first assumption, and future studies should endeavor to address the presence or absence of such a relationship. Additionally, future field work is required to determine to what degree, if any, erosion-resistant strata affect the planform morphology of tidal channels in northern Australia and Bangladesh. Indeed, as existing models of tidal channel formation assume that the tidal flats are purely alluvial, addressing the potential effects of bedrock is a clear next step towards understanding how these channels form and evolve.

2.5 Conclusion

Meandering channels are a common feature in both tidal and fluvial environments, but the formative processes are quite different: bidirectional flow in the tidal case, unidirectional flow in the fluvial case. As a result of these differing processes, one might expect tidal and fluvial meanders to display unique planform geometries. However, the minimal number of publications comparing tidal and fluvial channels limits our ability to ascertain how the channels differ in shape. In this study, we contribute to this question by calculating a variety of metrics related to the planform geometries of tidal and fluvial channels on the Ganges-Brahmaputra-Jamuna Delta in Bangladesh. Our data suggest that tidal meanders display low values of the asymmetry coefficient, which may be attributed to bidirectional flow, whereas fluvial meanders prefer higher negative and positive asymmetries. Although our data is insufficient to explain the physics controlling fluvial meander asymmetry, we have qualitatively observed that downstream skewed meanders often alternate with upstream skewed

meanders, which could be the cause of the observed fluvial asymmetry distribution.

Our measurements of the channels' intrinsic and Cartesian wavelengths indicate that wavelength displays an approximately linear correlation with meander width in both the tidal and fluvial environments, but the tidal meanders appear to have longer wavelengths in all cases. As none of the variables related to wavelength–mean annual discharge, mean annual flood, and grain size–are consistent with the trends observed in our data, further study is necessary to determine the cause of unusually short meander wavelengths in the fluvial case. At the same time, we note that (1) the coefficients on our (nearly linear) power law fits have overlapping error margins for almost every measurement configuration, and (2) it is possible that the short wavelengths could be a consequence of our inability to separate human channel modifications from the natural position of the banks when digitizing the channels.

The tidal and fluvial channels in our study area also display different sinuosity distributions, with the fluvial channels preferring higher sinuosity values. One explanation for this phenomenon is that lateral floodplain heterogeneities above the tidal limit encourage increased sinuosity in the fluvial channels; as tidal channels migrate very slowly, there should be fewer abandoned channel scars and clay plug deposits affecting their sinuosity values. Although we are unable to quantify tidal channel migration rates using our current methods, we observed only one oxbow lake forming in the Sundarbans region of the delta, which is consistent with minimal channel migration.

It is interesting to note that our data do not confirm Marani *et al.*'s (2002) observation that tidal channels display higher values of the second curvature harmonic than fluvial channels. In contrast, we find some evidence that the second curvature harmonic is relatively higher in the fluvial channels, in particular when we include isolated and/or low-sinuosity "meanders" in our analysis. When we calculate the Fourier transform of the channels' curvature over two or three meanders at the standard threshold meander sinuosity of 1.5, there is no difference in the statistical distribution of the second harmonic for the tidal versus fluvial meander cases.

The flaring of tidal channels near their mouths has been well-established, but we are

aware of only a single study (Davies and Woodroffe, 2010) that systematically compares normalized metrics of tidal channel mouth shape. We calculated similar metrics to classify the shape of tidal channels on the Ganges-Brahmaputra-Jamuna Delta and observed a relatively strong positive correlation between channel mouth width and e-folding length, a weak negative correlation between mouth width and the channel shape parameter, and a positive correlation between mouth width and the constant width at infinity for those channels with an upstream connection. Although presently available data is insufficient to explain the relationship between these variables, a "thought experiment" related to the interaction of relevant processes demonstrates one way in which tidal prism, delta slope, fluvial discharge, and erosion-resistant strata could produce the observed channel mouth geometries.

Future studies focused on the differences between tidal and fluvial channels should address several important questions. First, we must determine whether the pattern of alternating downstream- and upstream-skewed meanders is statistically significant in the fluvial case. Another open question is whether the tidal flat surface is sufficiently homogeneous in comparison to the non-tidal floodplain to produce meanders of low sinuosity in the tidal case. Finally, it will be important to determine the degree to which autocompacted sediment layers and bedrock influence tidal channel mouth geometries, and to establish whether channel mouth width is a function of the tidal prism. Answering these questions will greatly improve our understanding of how and why tidal channels and fluvial channels differ.

Chapter 3

Extended methods section

3.1 Definitions

In this section, we define all directions with regards to the flood flow in the tidal channels. This means that the "left bank" of the channel is the left-hand bank when moving inland along the channel; similarly, the "right bank" of the channel is the right-hand bank when moving inland along the channel. These definitions remain true even for those channels that do not experience a flood/ebb cycle, such as river channels that are above the tidal limit.

Arc length, which we use as the intrinsic coordinate along the channels, is defined as zero at the point on the channel that is nearest the coast and increases with distance inland, as in Figure 2 of Marani *et al.* (2002) and Section 2.1.1 of Savenije (2005).

3.2 Digitizing Channels

Google Earth imagery was the source of the data presented in this thesis. This software was selected because (1) it offers free and user-friendly access to satellite imagery with resolution better than one meter per pixel, (2) the user has easy access to historical imagery, allowing one to observe the channels at various flow stages, and (3) the relative ease with which MATLAB is able to interface with Google Earth. Although Google Earth has long been recognized as a valuable teaching tool (*e.g.*, Lisle, 2006), to date few quantitative geo-

morphological studies have used Google Earth as a data source (Fisher *et al.*, 2012). However, Constantine and Dunne (2008) were able to predict the distribution of oxbow lake length as a function of sinuosity using measurements from Google Earth. Likewise, Fisher *et al.* (2012) demonstrated that the use of Google Earth greatly improved channel-width measurement accuracy relative to Landsat methods. More recently, Mariethoz *et al.* (2014) used Google Earth to produce training patterns for meander simulation.

We digitized all channels by manually drawing paths along the left and right banks, as defined by the limit of permanent vegetation along the channel. These paths consisted of a series of points separated by approximately one-eighth of the local channel width. Early digitization efforts (Channels 1 through 17) involved a much smaller distance between consecutive points, which served little purpose beyond capturing local irregularities in the bank due to vegetation overhanging the channel, slumping, etc. For the narrowest portions of certain channels (local width less than 4 meters), the lower limit on Google Earth's zoom capability made it physically impossible to digitize eight points per local width; however, we visually inspected the resulting channel centerlines (see next section) to verify that this did not affect the results.

In their study concerning fluvial meander statistics, Howard and Hemberger (1991) required a channel reach to have at least 40 meanders with no major confluences, having observed that channel statistics display high variability for reaches less than several tens of meanders in length and that changes in discharge due to tributaries affect the dominant wavelength of a channel. However, the tidally influenced portion of the Ganges-Brahmaputra-Jamuna Delta consists of a densely interconnected network of channels (Passalacqua *et al.*, 2013), such that it is common for a single tidal channel thread to persist for only two or three full meanders between channel junctions. In order for our study to proceed, we consequently must assume that each tidal channel in the study area represents one realization of the same fundamental process, and that although we have insufficient data to address differences between two given tidal channels, we can analyze the properties of tidal channels as an aggregate. At the same time, it is desirable to make each digitized channel as long as possible

to reduce the amount of data which must be eliminated as a consequence of our smoothing procedure (see Section 3.4.5 and 3.4.6). Thus when digitizing the banks, we begin at the downstream end of a channel and proceed upstream until reaching a junction. If we can continue digitizing in an upstream direction without introducing an abrupt change in channel width or visible meander wavelength, we select whichever of the channels is most visually similar to the downstream reach and continue digitizing. In no case do we allow the digitized channel to form a loop or return to the coast. Davies and Woodroffe (2010) broke down multi-channel estuaries into single channels in a similar manner, although that paper does not address how this might affect the meander statistics.

There are several sources of uncertainty in the position of the digitized banks. First, although our intention in observing the position of the vegetation was to capture the bankfull width of each channel, Riley (1972) found that irregular growth patterns and different inundation tolerances among plant species make vegetation an unreliable tool for determining bankfull conditions. However, alternate definitions of "bankfull width" (Williams, 1978) proved to be incompatible with Google Earth because they required (1) identification of benches on the floodplain, which is infeasible when using satellite images of densely vegetated regions like the Sundarbans; (2) identification of points of maximum elevation on channel bars, a task which would require higher-resolution elevation data than that provided in Google Earth; or (3) identification of the transition from sand- to silt-sized particles along the channel, which cannot be determined from one-meter-resolution satellite imagery. Identifying bankfull conditions from the break in slope on a plot of stage versus discharge (Parker, 2004, Chapter 3) is likewise infeasible for this study because most of the channels are ungaged.

As an alternative to using a vegetation-based definition of bankfull, one could conceivably implement bankfull definitions requiring measured channel-cross sections (*e.g.*, Williams, 1978) using Google Earth's elevation profile tool. However, the absence of public documentation for Google Earth makes it unclear whether the software is using SRTM elevation data or some other source (Fisher *et al.*, 2012). Assuming the use of SRTM data over Bangladesh, the inability of InSAR to penetrate dense vegetation (Farr *et al.*, 2007) implies the existence

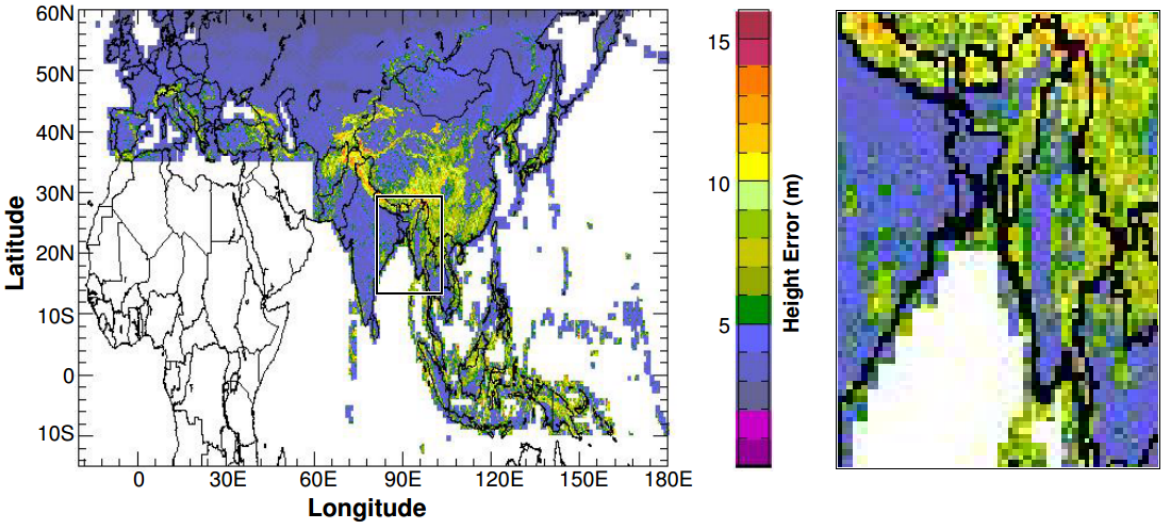

Figure 3.1: *Absolute error of SRTM data over Eurasia. From Rodríguez* et al.*, 2005, with inset added.*

of significant errors in elevation measurement throughout the Sundarbans. Figures from Rodríguez *et al.* (2005) indicate that the absolute error in SRTM elevation over Bangladesh is between 3 and 10 meters (Figure 3.1), although none of that study's ground-truth elevation transects pass through Bangladesh. Then again, Google Earth may be using a more accurate source of data in at least some regions. Benker *et al.* (2011) found that the average error between Google Earth elevations and high-precision GPS measurements in the Big Bend region of Texas was 1.63 meters, although Salinas-Castillo and Paredes-Hernández (2013) argue that the value should be increased to 4.77 meters. Both values are less than the 5 meter SRTM elevation error reported by Rodríguez *et al.* (2005). Similarly, Mohammed *et al.* (2013) report an average elevation error of 1.73 meters between Google Earth and GPS measurements in Khartoum, Sudan, which should have an SRTM error of 8 to 10 meters (Rodríguez *et al.*, 2005). We note that absolute elevation error is not as relevant as *relative* elevation error in terms of determining the bank's position on a channel cross section. However, the absence of vegetation in the channel and the presence of dense vegetation at the water's edge will likely result in a large jump in relative elevation at the vegetation limit, resulting in a bank position that is essentially identical to one visually selected from satellite imagery.

We remain wary of Google Earth's elevation data after examining transects across

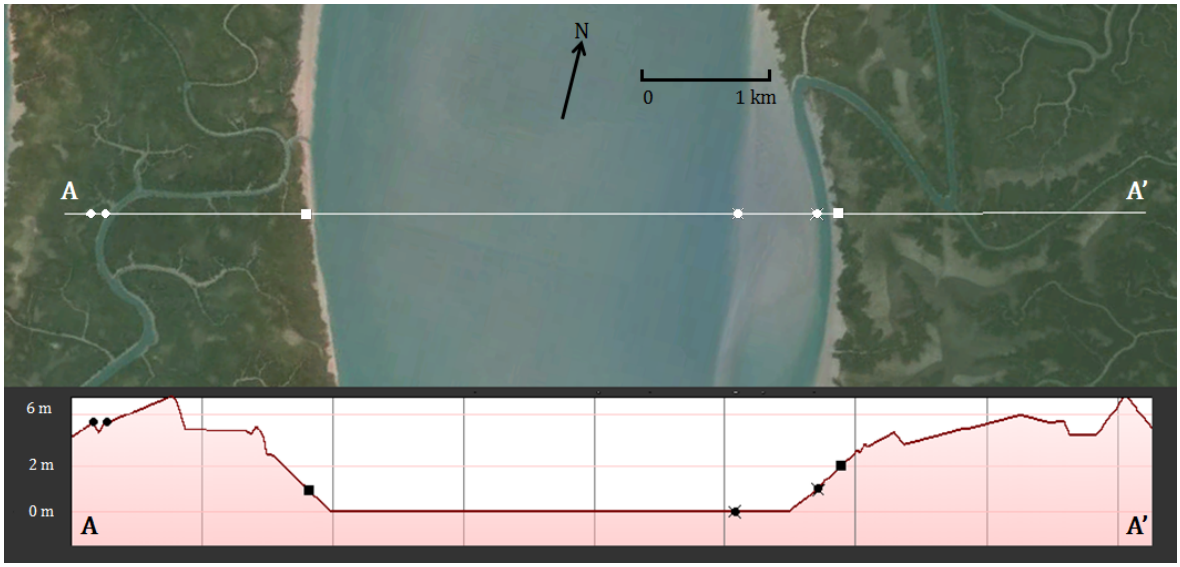

Figure 3.2: *Elevation profile across Channel 3. Google Earth imagery dated 2/7/10. Centered at 21.677527° N, 88.864202° E. Note that the vertical scale in the cross section is not linear. Flood flow is from bottom of page to top.*

multiple channels on the Ganges-Brahmaputra Delta. For large channels (local width on the order of several hundreds to thousands of meters; see Figure 3.2), the topography appears to correspond fairly well with the shape and position of the displayed channel. However, there are several aspects of Figure 3.2 that are troubling when one considers using the topographic profile to define the channel's bankfull width: the obvious lack of any bathymetric data, possibly a consequence of InSAR's inability to penetrate the smooth water surface (Farr *et al.*, 2007); the lack of topographic expression for the sand bar along the eastern bank of the channel, which historical imagery suggests has been a fairly intransient feature since at least 2007; and the offset between the topographic and imaged position of the small channel in the western portion of the figure, although there is no visible evidence that this channel has recently moved. Google Earth's elevation appears to vary in quality for the smaller channels (local width up to several hundreds of meters). In Figure 3.3, for example, the southern portion of the channel seems fairly well-resolved, whereas the northern portion of the channel shows almost no topographic expression on the cross-section.

In addition to the questionable quality of Google Earth's elevation data, another draw-

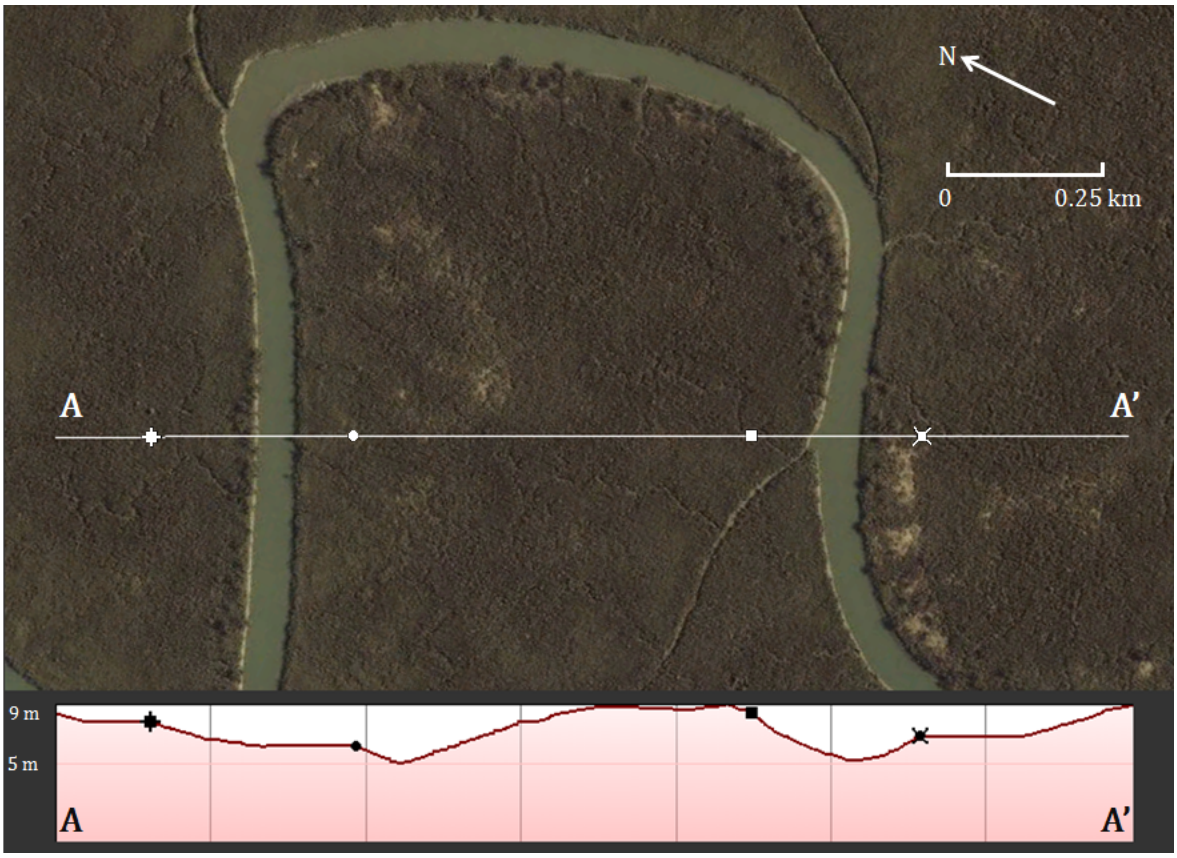

Figure 3.3: *Elevation profile across an unnumbered channel. Google Earth imagery dated 1/10/07. Centered at 21.869049° N, 89.391796° E. Flood flow is from right side of page to left, ebb flow from left side of page to right. Notice the near-absence of topographic expression of the channel in the left portion of the cross section. Vertical scale is nonlinear.*

back of using a cross-section-based definition of bankfull width is the potential increase in man-hours associated with channel digitization. One would have to plot an appropriate number of cross-sections for a given reach of channel and then transfer the selected bankfull points from each cross-section to the image before the banks of the channel could be defined. In contrast, the position of vegetation is already displayed in the image and eliminates the need for this additional step. After considering the increased uncertainty associated with Google Earth's elevation data, along with the added efficiency of basing the bankfull width on the limit of permanent along-channel vegetation, we believe that a vegetation-based definition of bankfull is most appropriate for the work presented here. Using vegetation to define the banks of the channel follows the work of several other authors, including Guccione (1983)

and Legleiter and Kyriakidis (2006). More importantly, using vegetation produces consistent bankfull measurements for all channels. Nevertheless, the reader should realize that all widths presented in this paper likely represent the minimum possible bankfull width of the channel.

The second source of uncertainty in the position of the digitized banks is closely related to the first. In populated portions of the delta, human interactions with the vegetation further complicate the question of where to place a channel's bank. In some areas, removal of vegetation may increase the channel's apparent bankfull width; in other regions, cultivation on sandbars may decrease the apparent width of the channel. The combination of local agricultural practices and tropical climate makes this particularly problematic:

> Once a char [sandbar] is exposed, following flood recession, its surface is soon occupied by the local inhabitants and put under cultivation. Plant growth under tropical conditions of Bangladesh is rapid and as a result many of the newly formed chars soon have the appearance of having been at that location for quite a long period. (Ghulam Kibria, 1972)

To compensate for cultivation within the banks of the channel, we identified locations along the channel which did not appear to be agriculturally modified (*e.g.*, large trees that would have required many years to grow) and then manually interpolated between these locations through the more ambiguous regions. Figure 3.4 shows an example of this method. The third source of uncertainty is that the word "bankfull" conveys different meanings for tidal channels versus fluvial channels. Leopold *et al.* (1964, p. 319) have found that fluvial rivers attain or exceed bankfull conditions with an average recurrence interval of 1.5 years, although Williams (1978) argues that the bankfull recurrence interval can fall anywhere between 1 year and 32 years and that the 1.5-year average has little meaning. Regardless of which viewpoint the reader prefers, the fluvial case appears to contrast significantly with the tidal case, where the recurrence interval at which a channel overtops its banks onto the intertidal flats is measured in hours rather than years (Leopold *et al.*, 1964, p. 322). This is hardly a trivial matter, considering that flow at the bankfull stage is thought to control the average morphology of the channel (Knighton, 1984, p. 94). To account for these differences, Leopold *et al.* (1964, p. 322) suggested that the most effective channel-forming discharge occurs only

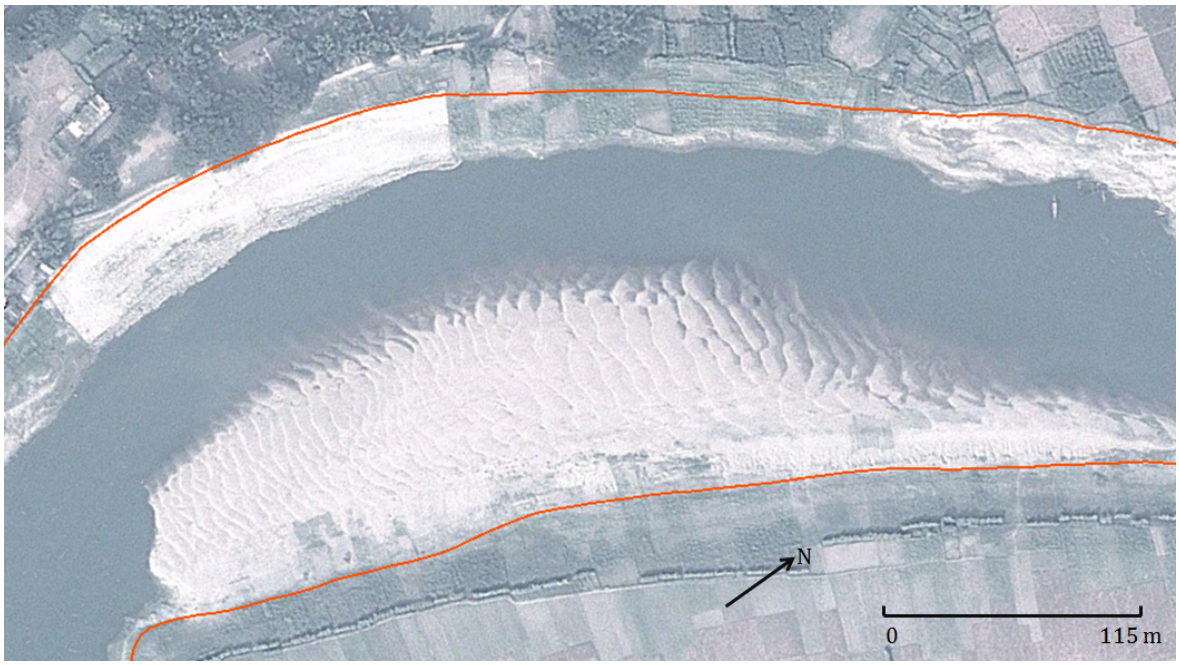

Figure 3.4: *Google Earth image centered at 24.970740° N,92.240134° E. Imagery date 1/13/12. Shows the digitized banks of Channel 45Aa. The bank nearer the top of the figure shows interpolation between two obviously sandy areas across agricultural fields that likely would not be vegetated without human activity. Flow is from right to left. This is the Surma River (Meghna tributary) in the Sylhet Division of Bangladesh.*

when two conditions are met simultaneously; that is, although the intertidal flats flood once per tidal cycle, conditions analogous to a fluvial channel's "bankfull" are only achieved if (1) the maximum stage is equal to the average high tide, and (2) the maximum velocity of the tidal current coincides with the time at which the channel overtops its banks. Based on Leopold *et al.*'s (1964) observation of the Potomac Estuary, these modified conditions have a recurrence interval of one year, although we are unaware of any subsequent studies confirming this result. However, Barwis (1978) notes that although bankfull is not the channel-forming discharge in a tidal environment, tidal channels' very steep banks cause the meander geometry to be the same at bankfull and maximum velocity conditions.

3.3 Obtaining Centerline

Following manual bank digitization, we converted the bank coordinates from degrees latitude and longitude to Bangladesh Transverse Mercator (BTM) coordinates (Ministry of Irrigation, 1992; note that we used WGS84 rather than Everest 1830 as the reference ellipsoid for these calculations). The BTM system is effectively identical to the Universal Transverse Mercator (UTM) system, except that it places a central meridian at 90°E to avoid splitting Bangladesh into two UTM zones. All conversions were performed using the method of Snyder (1987).

For ease of future calculations, it was desirable to represent the shape and position of the channel as a single curve in two-dimensional space. It is common practice in the literature to evaluate a channel's "centerline", but authors have a variety of ideas about what a centerline is and how best to obtain it. Kopsick (1983) found that the shape of a meandering channel is best represented by the position of a bend's outer bank, because this closely corresponds to the position of the thalweg and maximizes the channel's radius of curvature regardless of stage. However, because the focus of that study was to measure meander radii as isolated values, there is no indication of how to extend the method to a reach containing multiple bends. Indeed, the shape of the channel's centerline could vary greatly depending on how one connects the outer banks of adjacent half-meanders, as shown in Figure 3.5(a) and 3.5(b). One option would be to estimate the position of the thalweg based on, *e.g.*, the field observations of Dietrich *et al.* (1979), the numerical models of Parker *et al.* (1983), or the experimental results of Abad and Garcia (2009), but in the tidal case this would be complicated by the differing flow paths taken by the ebb and flood flow (*e.g.*, Ahnert, 1960; Dalrymple *et al.*, 2012, p. 93; Hughes, 2012, p. 286).

Another option for finding a channel's centerline defines the centerline of a channel as the midpoints of a series of line segments connecting corresponding points on the left and right bank (Legleiter and Kyriakidis, 2006). The method itself is simple to implement, but it requires careful selection of left- and right-bank point pairs. In particular, the spacing of points on the outer bank of a bend must be greater than the spacing of points on the inner

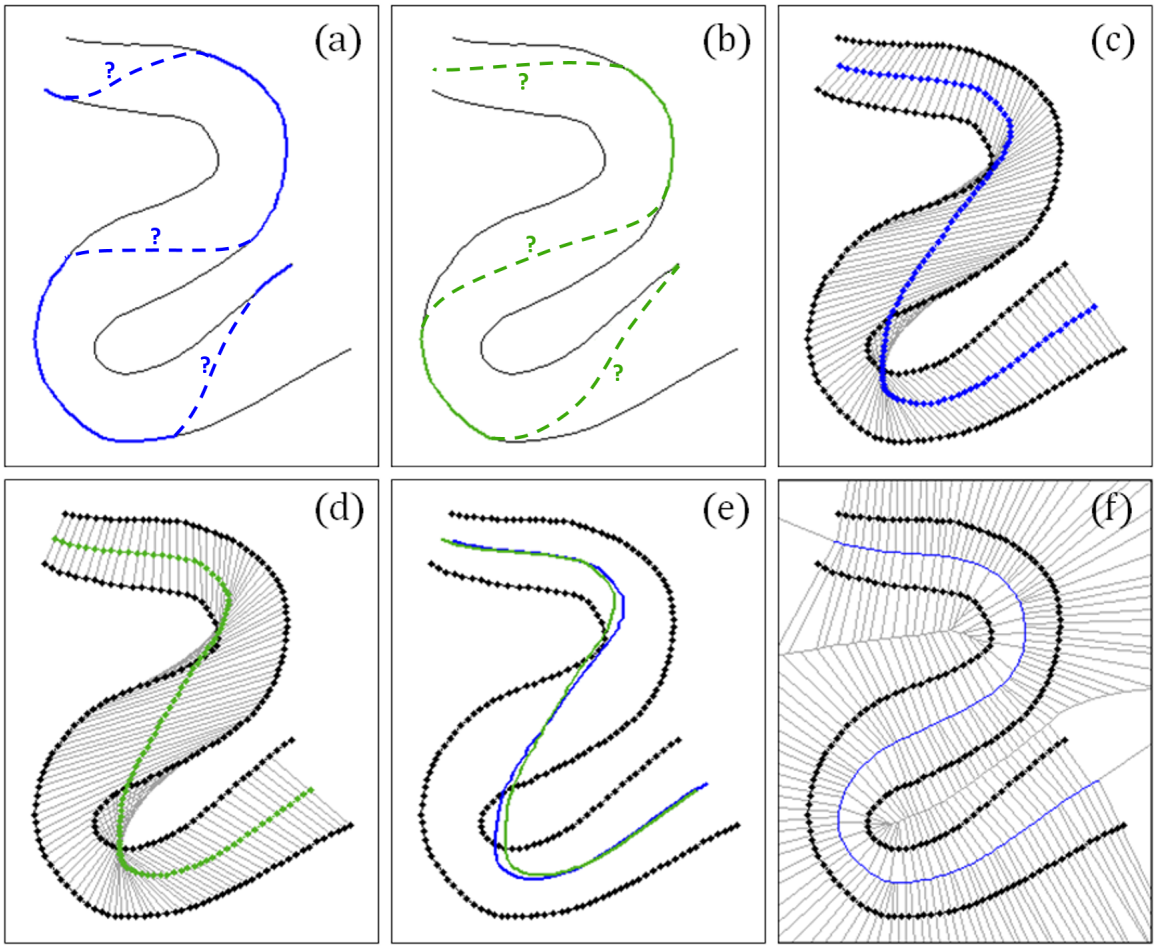

Figure 3.5: *Different methods for obtaining a channel's centerline. (a) After Kopsick (1983); (b) another possibility for Kopsick's method–the results are not unique; (c) Extreme example of Legleiter and Kyriakidis (2006); (d) another possibility for Legleiter and Kyriakidis; (e) centerlines from (c) and (d) overlain to show that the result is not unique; (f) Voronoi polygons acting as medial axis transform.*

bank of a bend; if the same spacing is used on both banks, the resulting centerline can leave the channel entirely (Figure 3.5(c) and (d)). Moreover, if unequal numbers of points exist on the left and right banks, the selection of which points to discard affects the position of the centerline, as shown in Figure 3.5(e). We do note that the basic principles of Euclidean geometry guarantee that this method would converge to a unique line down the center of the channel if the channel were prismatic and perfectly straight. However, it must be used with care in channels of high sinuosity, which limits its applicability.

A third possibility is to define the centerline of the channel as its medial axis (McAllister and Snoeyink, 2000; note that this is conceptually identical to the definition used by Fagherazzi *et al.*, 1999, and Davies and Woodroffe, 2010). The concept of the medial axis of a two-dimensional shape was first introduced by Blum (1967), who defined it as "the locus of points equidistant from the pattern"; Lee (1982) restates the definition more clearly: "Given an object represented, say by a simple polygon G, the medial axis $M(G)$ is the set of points $\{P\}$ internal to G such that there are at least two points on the object's boundary that are equidistant from $\{P\}$ and are closest to $\{P\}$". The transform from a shape to its medial axis is a function[1]; that is, there is only one possible medial axis for a given shape (Blum, 1967). If the shape is a *bona fide* polygon, the medial axis can be found exactly as a subset of the Voronoi edges corresponding to the shape's vertices (Lee, 1982). For shapes with continuous, smoothly curving edges, the medial axis can be approximated by finding the Voronoi diagram of a finite number of sampled points on the shape's boundary; as the number of sampled points approaches infinity, a subset of the Voronoi edges will converge to the medial axis (Brandt, 1994).

To implement this method, we consider the dual of the Voronoi diagram, which is known as Delaunay triangulation. Mostafavi *et al.* (2003) noted that although the Delaunay triangulation can be derived from the Voronoi polygons and vice versa, each has certain practical advantages over the other. In the case of obtaining a channel's centerline, we find that although the Voronoi diagram allows one to visualize the medial axis on a plot (Figure 3.5(f)), the Delaunay triangulation is more straightforward to use in the automatic extraction of the medial axis from a set of channel-bank points. Our algorithm for finding the medial axis of a channel is as follows: we first define a closed polygon by connecting the first digitized point on the left bank and the first digitized point on the right bank with a straight line segment. Similarly, we connect the last digitized point on the left bank and the last digitized point

[1]This function is invertible (injective or "one-to-one") if and only if we store information about distance to the shape in addition to the position of the medial axis. For example, given a circle of radius 2 centered at the origin, the (only possible) medial axis is a point at the origin. However, given that the medial axis is the point (0,0), we do not know whether the original shape is the circle of radius 2 or the circle of radius 17. But if we store both distance (2) and position (0,0) with the medial axis, we can reconstruct the original shape. (After Blum, 1967)

on the right bank with a straight line segment. Next, we perform a constrained Delaunay triangulation within the channel polygon. An important property of Delaunay triangulation is that the vertices of the Voronoi diagram are equal to the circumcenters of the Delaunay triangles (*e.g.*, Aurenhammer, 1991; Okabe *et al.*, 2000, p. 73; Aurenhammer *et al.*, 2013, consequence of Lemma 2.1 plus Theorem 2.1); thus we can extract the centerline visible in the Voronoi diagram by drawing line segments between the circumcenters of adjacent Delaunay triangles. Because the medial axis is sensitive to "bulges" or irregularities in the position of the bank (McAllister and Snoeyink, 2000), we ignore the circumcenters of any triangles that have all three vertices on the same bank when constructing the channel's centerline; an example is shown in Figure 3.6. This acts as a simple pruning algorithm for the medial axis transform (*e.g.*, Shaked and Bruckstein, 1998).

3.4 Smoothing Centerline

We now consider methods for smoothing the channel centerline produced by the medial axis transform. Because our ultimate goal is to analyze the meander-scale channel planform, we seek a smoothing method that will eliminate (1) noise due to real irregularities in the bank with a length scale less than one channel width, such as those produced by bank slumping or tree canopies protruding over the water surface, and (2) noise that is an artifact of using Voronoi polygons to approximate the medial axis. As discussed in the previous section, ignoring those Delaunay triangles that have all three vertices on the same bank has already eliminated the most significant bank perturbations, so we focus our attention on the second source of noise. McAllister and Snoeyink (2000) note that when Voronoi polygons are used to approximate the medial axis transform of a channel, a wide spacing between the digitized points along the banks causes the centerline to take on a zig-zag appearance (see inset of Figure 3.6). We expect that as the number of digitized points increases to infinity, the zig-zags will decrease in amplitude as the medial axis approximation converges to a smooth curve. Nevertheless, the presence of even low-amplitude zig-zags is problematic with regards to calculating the curvature of the channel for a number of reasons. Taking the first and

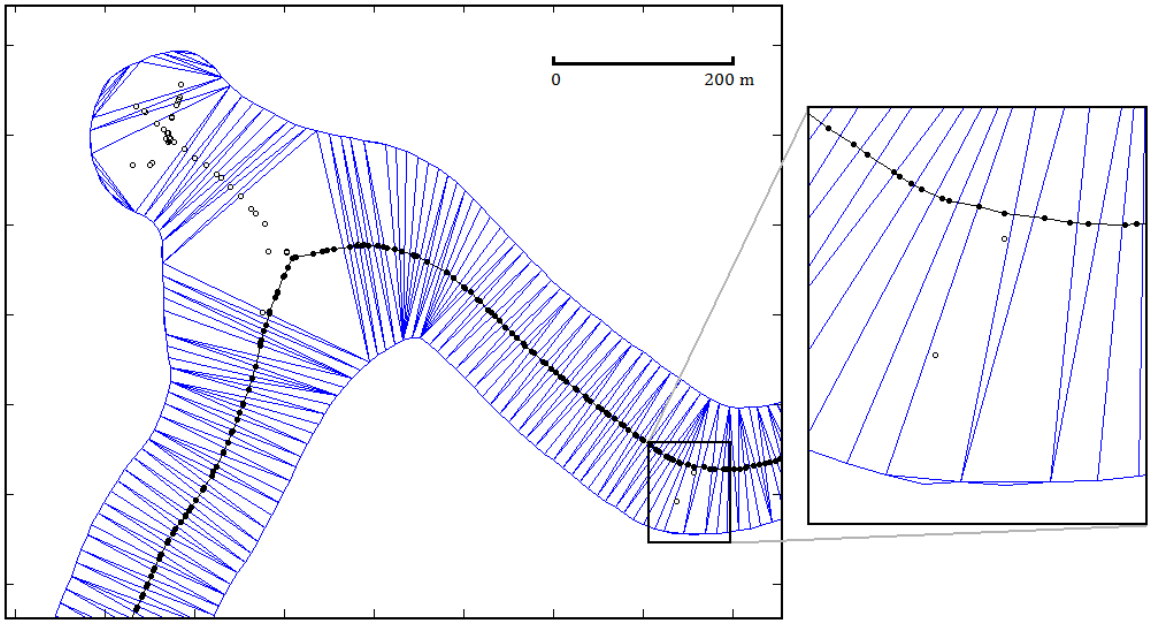

Figure 3.6: *Shows a portion of Channel 65 with the constrained Delaunay triangulation in blue. The triangles' circumcenters are displayed as open circles if all three of the corresponding triangle's vertices lie on the same bank, and as filled circles if the triangle has vertices on both banks. The circumcenters from the triangles in the bulge seen in the upper left of the figure are not included in the centerline because all three vertices of the triangles lie on the same bank of the channel; however, these points do define Voronoi edges that are part of the medial axis proper. The inset shows an example where noise due to raster digitization has caused two triangles to have all three vertices on the same bank. The circumcenters from these triangles are not included in the channel centerline, but again would be used to define the true medial axis.*

second derivatives of the centerline, which is necessary for the curvature computation, will amplify the noise considerably (Figure 3.7 (A), (B), and (C)). Additionally, because curvature is defined as the inverse of the local radius of curvature, these small changes in direction along the centerline will produce large curvature values (Fagherazzi *et al.*, 2004) that may drown out the desired signal (Figure 3.7 (D)).

The complexity of this smoothing problem increases greatly when one considers that tidal meanders are statistically non-stationary. It is a well-known fact that estuaries, including tidal channels (Wolanski, 2007, p. 2), increase in width towards the coast (Davies and Woodroffe, 2010). Indeed, Savenije (2005) has shown that tidal estuaries with parallel banks are morphologically unstable. If we assume that meander wavelength is a function of channel

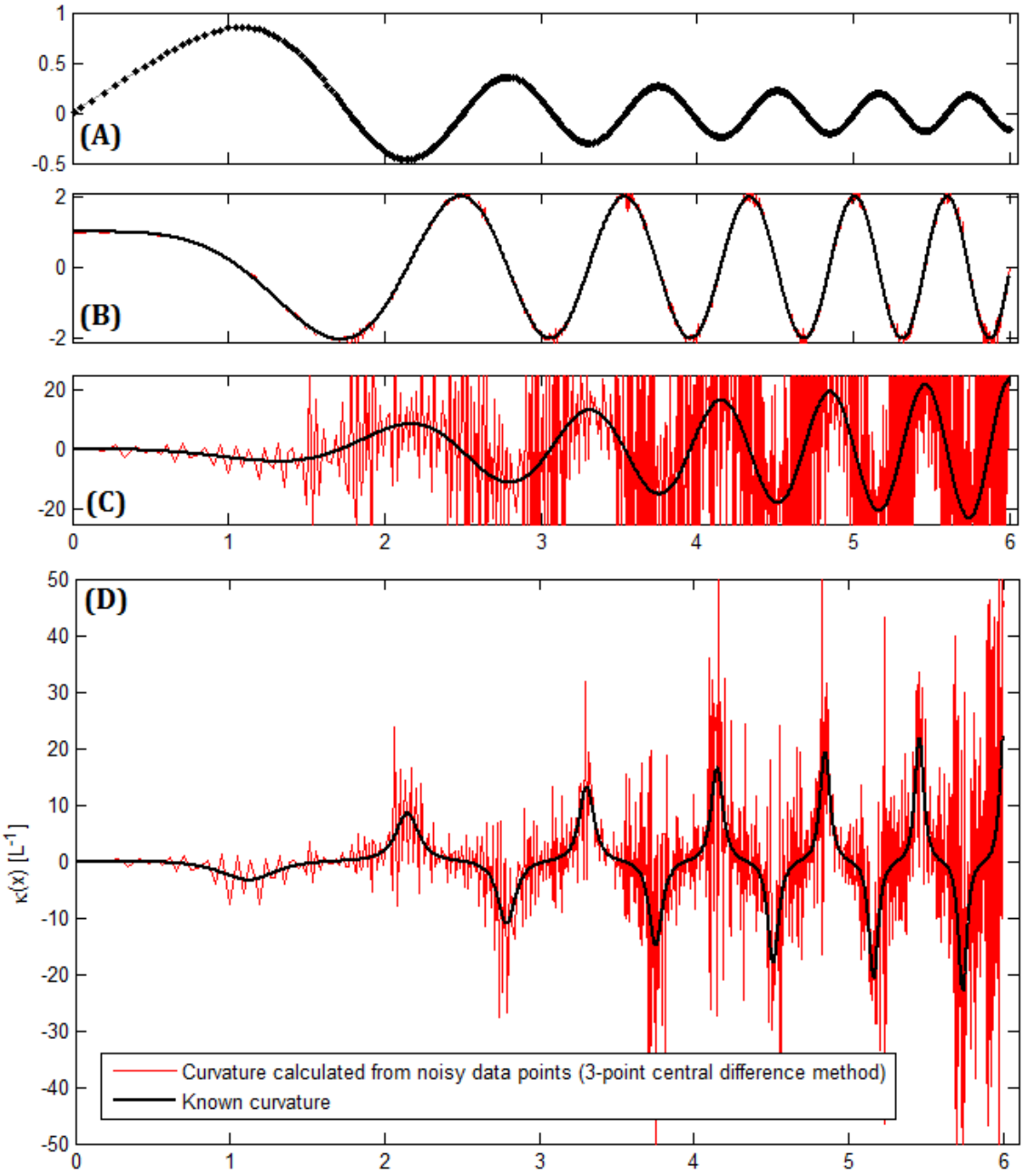

Figure 3.7: *The effect of noise on differentiation and curvature calculations. (A) The decaying chirp signal* $y = \frac{sin(x^2)}{x}$ *plus noise for* $x \in [0.01, 6]$. *(B) The first derivative of the signal in (A) calculated using a three-point central difference method, compared to the known derivative of the chirp. (C) The second derivative of the signal in (A) calculated using a three-point central difference method, compared to the known second derivative of the chirp. (D) The curvature of the chirp, calculated using the values from (B) and (C), compared to the known curvature of the chirp.*

width, as has been observed in meandering rivers (Leopold and Wolman, 1960; Ferguson, 1975; Williams, 1986), we can easily see that meander wavelength should decrease as we move inland along the channel. Moreover, the "straight-meandering-straight" pattern observed by Dalrymple *et al.* (1992) suggests that the signal of interest is non-stationary. Consequently, oscillations that we would consider noise in the downstream portion of the channel may have the same wavelength and amplitude as the signal of interest in the upstream portion of the channel.

To analyze the efficacy of various algorithms for smoothing nonstationary data, we examined the effect of each algorithm on the decaying chirp signal $y = \frac{sin(x^2)}{x}$ for $x \in [0.01, 6]$. We plotted this function in MATLAB and then introduced noise to the data by manually clicking along the curve with a target sampling density of 50 clicks between consecutive inflection points. The resulting set of sampled points mimics the observed behavior of the tidal channel centerlines in that the sampled points are unevenly spaced in arc length, but with the overall trend of the arc length between sampled points decreasing inland as the channel narrows. Additionally, we performed the resampling such that the vertical field of view was approximately equal to the local amplitude of the signal. This caused the noise introduced by manual resampling to decrease in magnitude as the chirp decreases in magnitude, just as the noise in the tidal channel centerlines decreases in magnitude with distance inland.

3.4.1 Rosensaft algorithm

The inherent presence of zig-zags in the medial axes produced by Voronoi polygons suggests that the algorithm proposed by Rosensaft (1995) may be well suited to this smoothing problem. This algorithm smooths a digitized line by considering sets of four consecutive points; if these four points define a "Z" shape with given length and angle parameters, then the two middle points are deleted and replaced by their average. The user must specify a maximum length for segment D_2 and a maximum absolute size for angles A_1 and A_2 (Figure 3.8), beyond which smoothing will not occur. For the channel centerlines, we set the maximum absolute size of A_1 and A_2 to 180°, indicating that *any* Z-shaped patterns defined

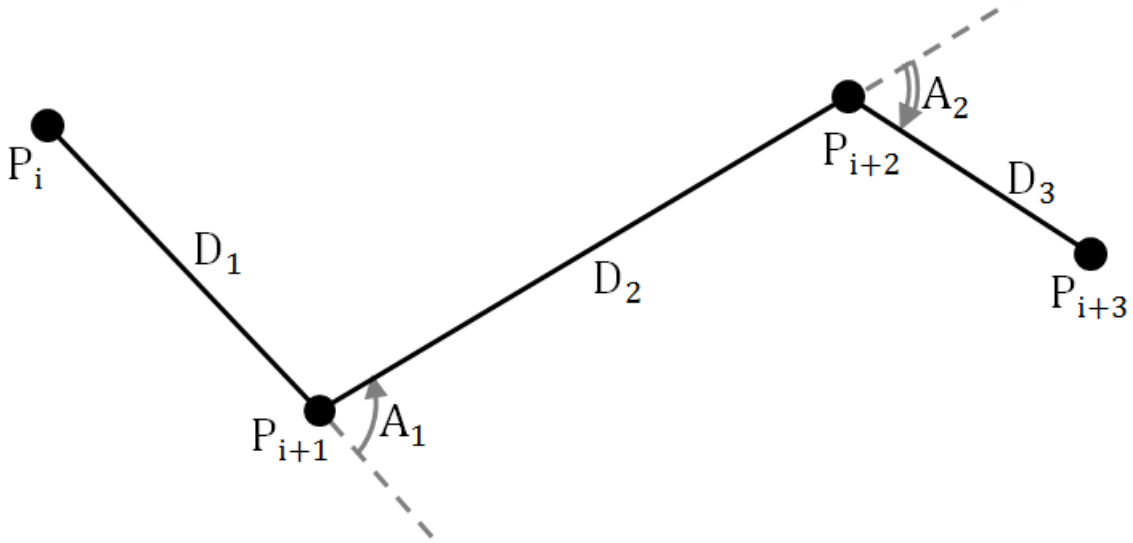

Figure 3.8: *Schematic of variables considered in Rosensaft (1995) algorithm. Note that the direction in which we measure the angles matters (hence the arrows).*

by four consecutive points represent noise. This is reasonable considering that it would be extremely unusual for a channel to complete a full meander in a single width, and having digitized 8 points per local width per bank should guarantee a minimum of 7 centerline points within this distance. The maximum length of D_2 should presumably correspond to the width of the channel.

When we ran Rosensaft's (1995) algorithm for our noisy decaying chirp signal, the results were not what we expected. Although the algorithm was able to smooth the high-curvature regions while maintaining sufficient data points, it produced a very long, perfectly straight segments with no data points in the low-curvature regions. At first we thought this might be the result of a bug in our code; however, careful analysis revealed that the problem was with the design of the algorithm itself. Specifically, the "delete" conditions of the algorithm are based only on the parameters A_1, A_2, and D_1 (Figure 3.8), which means that the algorithm will replace points P_{i+1} and P_{i+2} regardless of the length of D_1. Indeed, D_1 can continue increasing in length indefinitely, producing the long stretches with no data points that we observed. While this is not an issue for data reduction purposes, the algorithm

would need to be reworked to include the length of D_1 in the delete conditions in order to be useful for our smoothing needs. We attempted to introduce D_1 into the stop conditions by trying (a) a maximum absolute length for D_1 and (b) a maximum value of the ratio D_1/D_2, but neither of these changes produced the desired smoothing properties.

3.4.2 Douglas-Peucker algorithm

An alternative method for smoothing noisy data is the algorithm described by Douglas and Peucker (1973). The Douglas-Peucker algorithm was first developed as a means of data-size reduction for digitized lines in cartography. However, given a curve represented by an ordered set of densely spaced, noisy points, it seems plausible that one could smooth the line by selecting a subset of certain key points that define the fundamental shape of the curve while deleting the rest. To implement the algorithm, the user selects a maximum distance or "ε-buffer" (Saalfeld, 1999) from which the new curve may deviate from the original curve. The selection of points to keep then proceeds as follows (see Figure 3.9):

1. The endpoints of the curve are kept by default, and the line segment connecting these two points acts as an initial guess for the simplified line.

2. We measure the perpendicular distance from each data point to the new line. If one or more points exceed a distance ε from the line, the point that is farthest from the line is added to the subset of points to be kept.

3. Connecting subsequent "kept" points produces a new guess for the simplified line. We again measure the perpendicular distance from each point to the corresponding line segment. For a given segment, if any points exceed a distance ε from that segment, the point that is farthest from the segment is added to the subset of points to be kept.

4. Iteration continues until the distance from all points to the new line is less than ε.

The primary issue with using the Douglas-Peucker algorithm on a non-stationary signal is to determine a value of ε that is appropriate for the entire curve. In Figure 3.10, we show the output of the Douglas-Peucker algorithm for $\varepsilon = 0.001$ and $\varepsilon = 0.05$. When $\varepsilon = 0.001$,

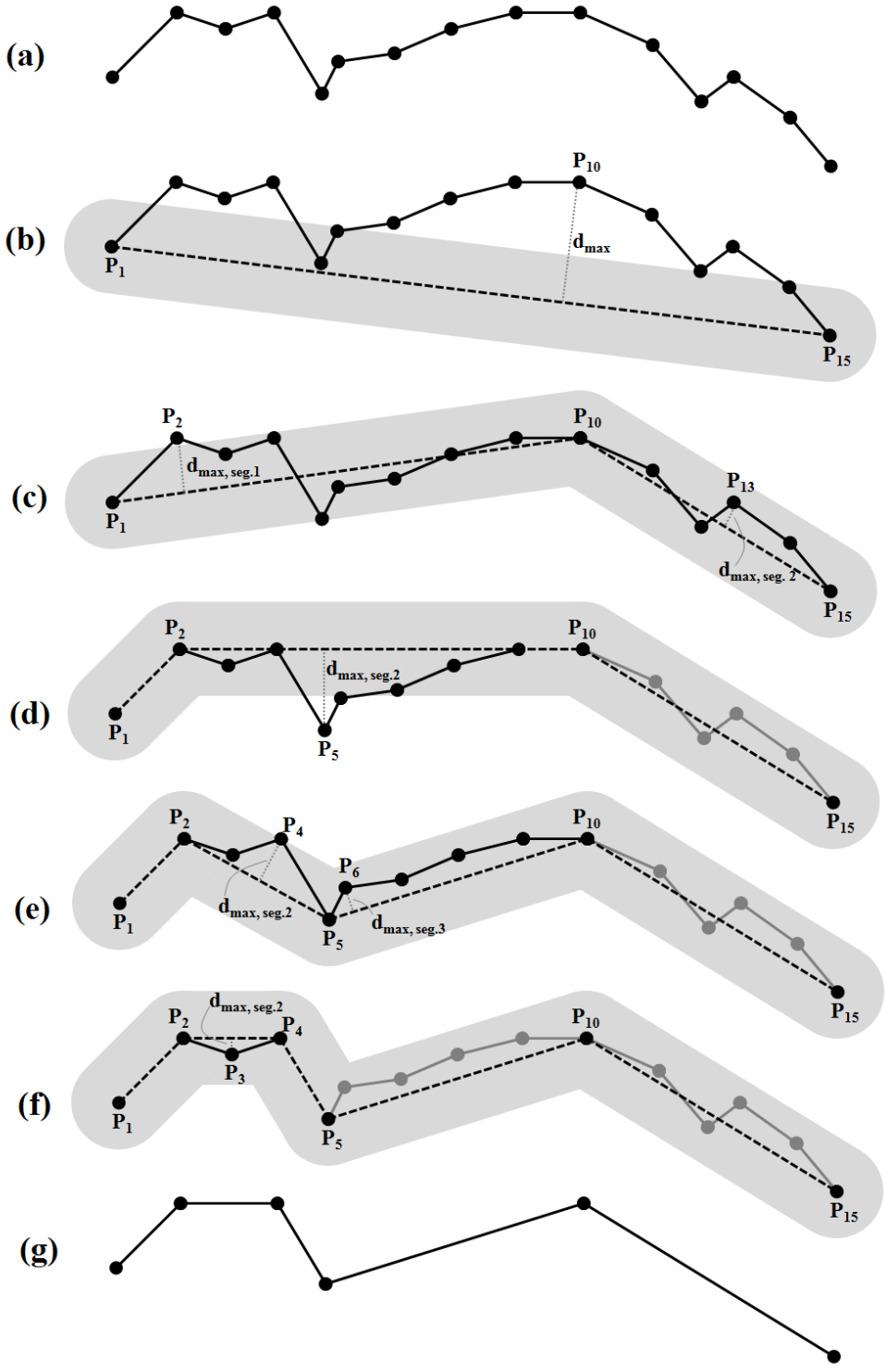

Figure 3.9: *Steps for implementing the Douglas-Peucker algorithm. The gray regions represent the epsilon-buffer of Saalfeld (1999).*

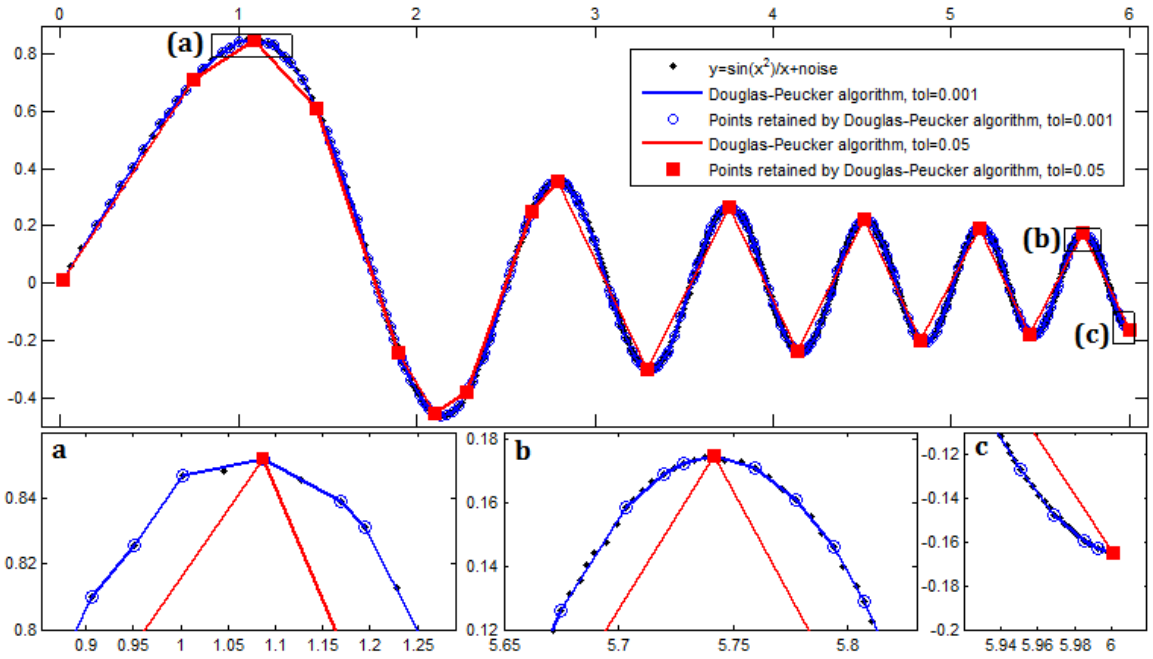

Figure 3.10: *Results of using the Douglas-Peucker algorithm on the decaying chirp. Insets (a) and (b) show enlargements of the indicated regions in the main plot.*

the algorithm acceptably smoothes the higher-frequency regions of the curve, but it preserves noise in the lower-frequency regions of the curve. Increasing ε to a larger value produces a representation of the curve that resembles a decaying triangular wave. One solution might be to define ε as a function of distance along the curve; however, we had become concerned by the prospect of deleting points from our data set and decided to move on to other algorithms.

3.4.3 Savitzky-Golay filter

Our observations of the Rosensaft (1995) and Douglas-Peucker (1973) algorithms suggest that deleting points from a channel's centerline does not produce the desired smoothing effects. Hence we turn our attention to smoothing algorithms that preserve the original quantity of points. One algorithm with this property is the well-known Savitzky-Golay filter (Savitzky and Golay, 1964). Although the original algorithm requires that the data points be evenly sampled, subsequent studies have extended its use to nonuniformly sampled data (*e.g.*, Gorry, 1991). Implementation of Savitzky-Golay filtering requires the user to choose

two parameters: a smoothing window of length $2n + 1$, $n \in \mathbb{N}$, and a polynomial degree $d \leq 2n$. To perform the smoothing, a polynomial of degree d is fitted with least squares to the points in the smoothing window, and the smoothed value at the middle point in the window is calculated as the value of the polynomial at that point. The window is then shifted one point forward and the process is repeated until all possible windows have been considered (Figure 3.11). Note that the first and last n points will not be smoothed by this process; Eilers (2003, in that paper's supporting material) suggests using the first and last fitted polynomials to calculate values at these points.

The Savitzky-Golay filter is attractive as a smoothing algorithm because it has the property of preserving the shape and height of local extrema in the data (Ahnert and Abel, 2007; Schafer, 2011), unlike a basic moving average, which reduces the value of data peaks (Savitzky and Golay, 1964). An additional benefit of this method is that values of the signal's first d derivatives can be calculated by differentiating the polynomial centered at the point of interest, eliminating the need to use ill-conditioned finite difference methods for numerical differentiation (Ahnert and Abel, 2007). Unfortunately, smoothing the data with local windows can produce small jumps between windows, which adversely affect the smoothness of the derivative (Eilers, 2003 in supporting material; Ahnert and Abel, 2007). Indeed, Ahnert and Abel (2007) found that the Savitzky-Golay filter was two orders of magnitude more noisy than several global methods (*i.e.*, methods which consider the full data set when smoothing, rather than local subsets of the data). For additional details on the properties of Savitzky-Golay differentiation, the reader is directed to the paper by Luo *et al.* (2005).

Another drawback of the Savitzky-Golay filter is that the user must define optimal parameters for the window and the polynomial degree. For constant window length, increasing the degree of the polynomial increases data fidelity at the expense of smoothing; for constant polynomial degree, increasing the length of the window increases smoothing at the expense of data fidelity (Bromba and Zlegler, 1981; Browne et al., 2007). It is also common practice to filter the data multiple times, requiring the user to determine an optimal number of itera-

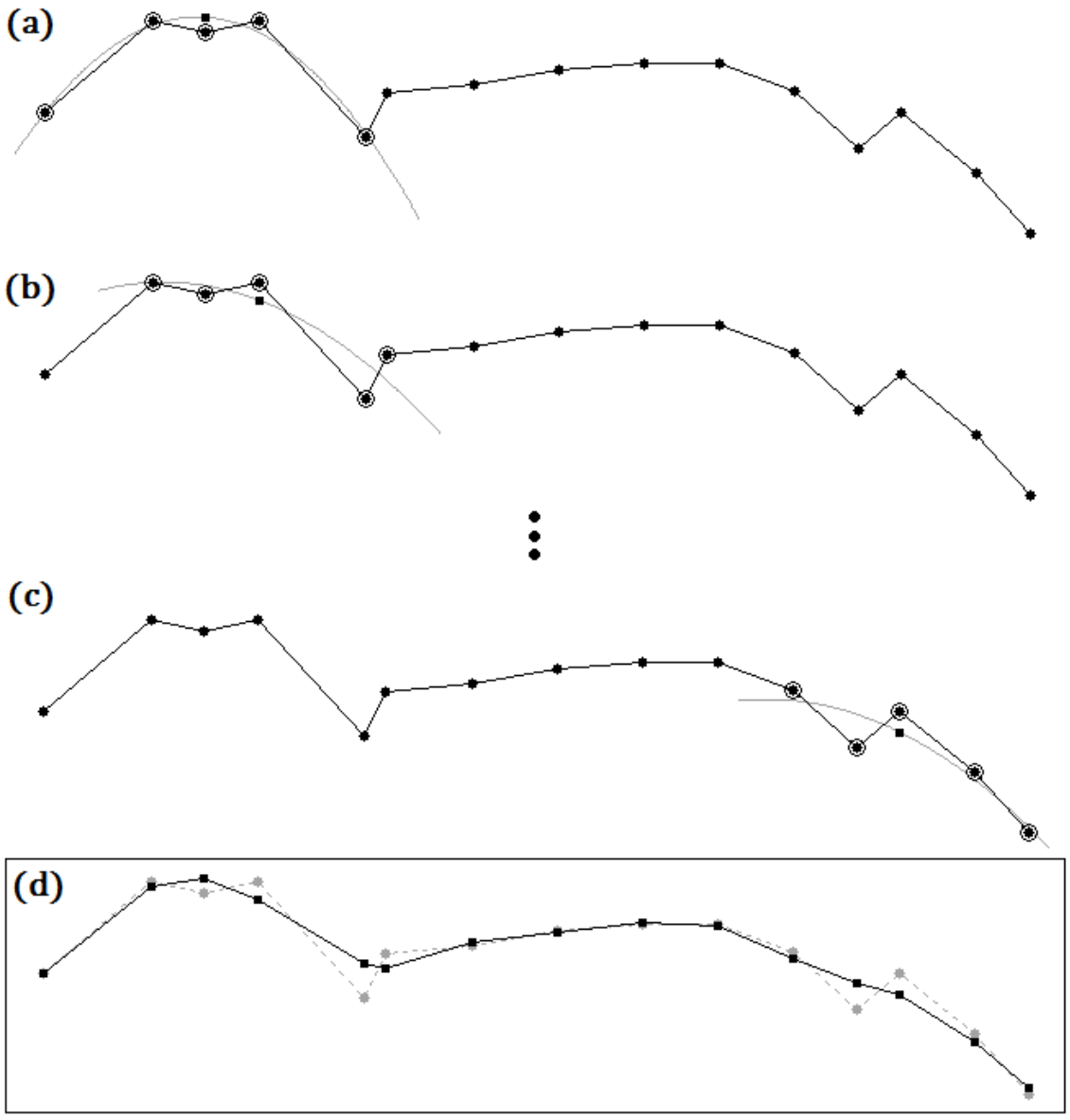

Figure 3.11: *Steps for implementing the Savitzky-Golay filter with $n = 2$ (window=5), $d = 2$, and one iteration. Filled circles indicate original data points. Open circles indicate those points in the window currently being considered. Squares indicate the smoothed data points. (a) the first window centered at the third data point with a least-squares parabola. (b) The window from (a) shifts right by one point and the process is repeated. (c) The window continues to shift until it reaches the end of the data. In this example, this is the window centered at the 13th data point. (d) The final set of smooth points superimposed on the original data points. Note that smoothed values for the first and last two points were obtained from the parabolas in (a) and (c), respectively.*

tions. In previous studies of meandering channels, authors have found a variety of parameters to be "optimal". Fagherazzi *et al.* (2004) used a fifth-degree polynomial, a filter window of 15 points, and 3 iterations to smooth tidal channel centerlines from San Francisco Bay, California, whereas Legleiter and Kyriakidis (2006) used a third-degree polynomial, a filter window of 7 points, and 3 iterations to smooth the centerline of Soda Butte Creek, Wyoming. Savitzky and Golay (1964) stated that the window should be sufficiently small that it contains no more than one inflection point in the data, but beyond this, selecting the filter parameters is a "largely arbitrary" decision (Barak, 1995) that is both subjective and site-specific (Legleiter and Kyriakidis, 2006). One way to avoid this subjectivity involves the use of *adaptive* Savitzky-Golay filters, in which the local polynomial degree (Barak, 1995; Jakubowska and Kubiak, 2004) or local filter length (Browne *et al.*, 2007) is selected by systematically increasing d or n, respectively, and observing the effect of this change on the residuals of the fit. These methods have been shown to outperform the standard Savitzky-Golay filter and seem particularly attractive for smoothing non-stationary signals, such as the tidal channel centerlines. However, to quote Browne *et al.* (2007), "It is not recommended that applied researchers replace the [Savitzky-Golay filter] by implementing the [adaptive window Savitzky-Golay filter (AWSGF)] in its current form. As with any data-adaptive approach, the behavior of the AWSGF needs to be tested in a wide range of situations." Given this statement, coupled with the fact that adaptive methods do not guarantee any improvement in our ability to differentiate the signal, we do not consider these methods further.

3.4.4 Cubic smoothing spline

The next smoothing method we consider is the cubic smoothing spline. In its simplest form, the smoothing spline is the piecewise-defined, continuous, twice-differentiable function f that minimizes

$$p\sum_{j=1}^{n}[y_j - f(x_j)]^2 + (1-p)\int_{x_1}^{x_n}[f''(t)]^2\,dt \tag{3.1}$$

(after De Boor, 1978, p. 235) where $\{x_i\}$ and $\{y_i\}$ are the coordinates of the n data points and p is a smoothing parameter controlling the balance between goodness of fit (the series

term in (3.1)) and smoothness (the integral term in (3.1)). The MATLAB function `csaps` provides a simple way to obtain the piecewise-polynomial form of the spline, which can then be evaluated or differentiated using the functions `ppval` and `fnder`, respectively.

Because it controls the trade-off between interpolation and smoothing, the choice of the parameter p is clearly of great importance when creating a smoothing spline. When $p = 0$, f is the linear least-squares fit to the data points, whereas when $p = 1$, f is the cubic interpolating spline with natural boundary conditions. The documentation for `csaps` recommends choosing $p = (1 + \frac{h^3}{6 \cdot 10^v})^{-1}$, where h is the average spacing of the abscissa and v is a value that ranges from -1 for moderate smoothing to 1 for moderate data fidelity (The MathWorks, 2014). Alternate methods of selecting the smoothing parameter involve ordinary cross validation or generalized cross validation (*e.g.*, Wahba, 1990, Chapter 4; Green and Silverman, 1994, Chapter 3). Figures 3.12 and 3.13 demonstrate the effect of smoothing the artificial decaying-chirp data using smoothing splines for various values of p. The mean spacing of the abscissa is 0.00882, suggesting that an optimal value of p should be somewhere between 0.983 (for $v = 1$) and 0.99999886 (for $v = -1$). However, the overall decrease in the spacing of the abscissa along the chirp prevents a single value of p from being suitable everywhere. Indeed, after testing several values of p, we observe that the spline curves behave differently depending on position along the chirp. When $p = 0.999$, the smoothing spline effectively smoothes the data points within the lower-frequency oscillations at the beginning of the chirp (Figure 3.12, inset a), but tends to oversmooth the higher-frequency oscillations at the end of the chirp signal (insets b and c). Increasing p to 0.999999 produces a smoothing spline that performs well within these higher-frequency oscillations but preserves excessive noise near the beginning of the signal. Differentiating the splines confirms our observation that this method is not appropriate for smoothing nonstationary signals (Figure 3.13).

3.4.5 Local cubic smoothing splines

One solution to this problem that we considered was to merge the concept of local-window smoothing, as in the Savitzky-Golay filter, with smoothing spline interpolation. This

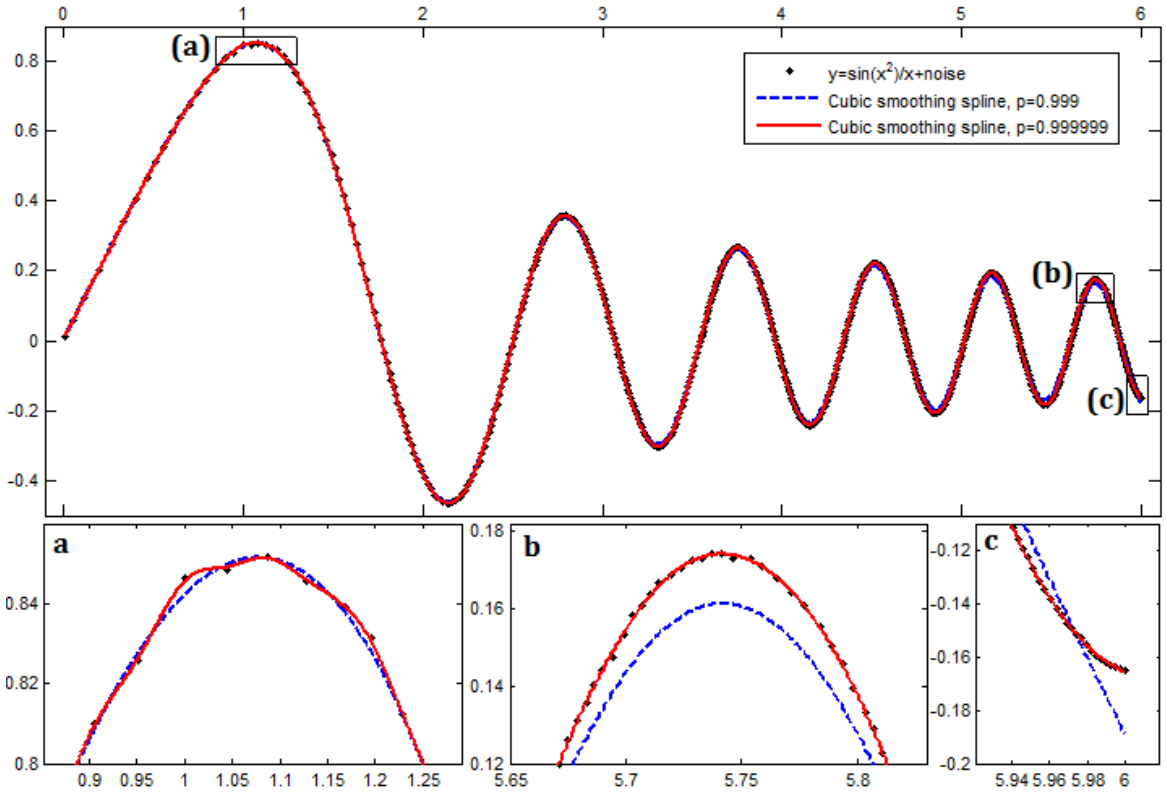

Figure 3.12: *Smoothing spline with various values of p applied to decaying chirp signal plus noise.*

allows us to change the value of p between windows such that p is appropriate for the local spacing of the data points. To implement this method, we select a window length $w \in \mathbb{N}$ and a constant value for v. We then calculate the mean value of the abscissa for the first w points: $h = \frac{x_1+\ldots+x_w}{w}$. After using this value of h to compute a value for p, we construct a cubic smoothing spline for these w data points. We then shift the window forward by one point and repeat the process until the window reaches the last data point. Unlike the Savitzky-Golay filter, in which only the value at the midpoint of the window is calculated, we calculate values at all w points for each smoothing spline and then average these with the values obtained from any splines that overlap at a given point. Figure 3.14 shows a schematic example of this procedure.

Smoothing with local, overlapping cubic smoothing splines has two significant limitations that we must consider. Unlike cubic spline interpolation, in which an underdeter-

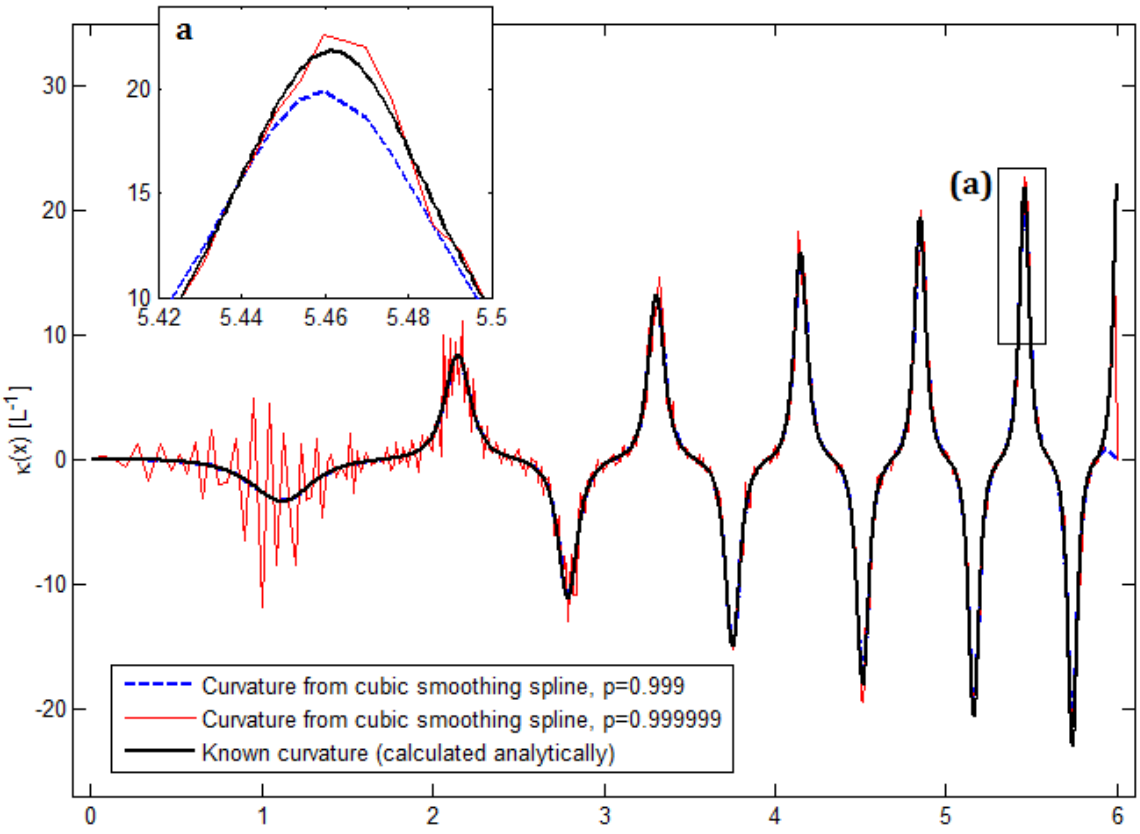

Figure 3.13: *Curvature of decaying chirp signal calculated from cubic spline.*

mined system of equations requires a choice of appropriate boundary conditions (e.g., Bradie, 2005, Section 5.6), the introduction of the roughness penalty $\int[f'']^2$ automatically produces a spline with natural boundary conditions (Green and Silverman, 1994, p. 18)–that is, $f''(x_1) = f''(x_n) = 0$, as shown in Figure 3.15. This is true whether we use a single (global) smoothing spline for all data points or multiple smoothing splines covering local windows of data. We can mitigate the effect of the boundary conditions by throwing away points at the beginning and end of the splines, but this raises the question of how many points must be eliminated.

To answer the question of how far boundary condition effects "propagate" into the spline before becoming unnoticeable, we examined the effect of smoothing splines on the curvature of two simple functions: the quarter-circle of radius 1 given by $x = cos(s)$, $y = sin(s)$, $s \in [0, \frac{\pi}{2}]$, and the sine-generated curve with curvature function $\kappa(s) = \frac{3\pi^2}{5}cos(\pi s) + \frac{\pi^2}{10}cos(\frac{2\pi}{1.3}s)$,

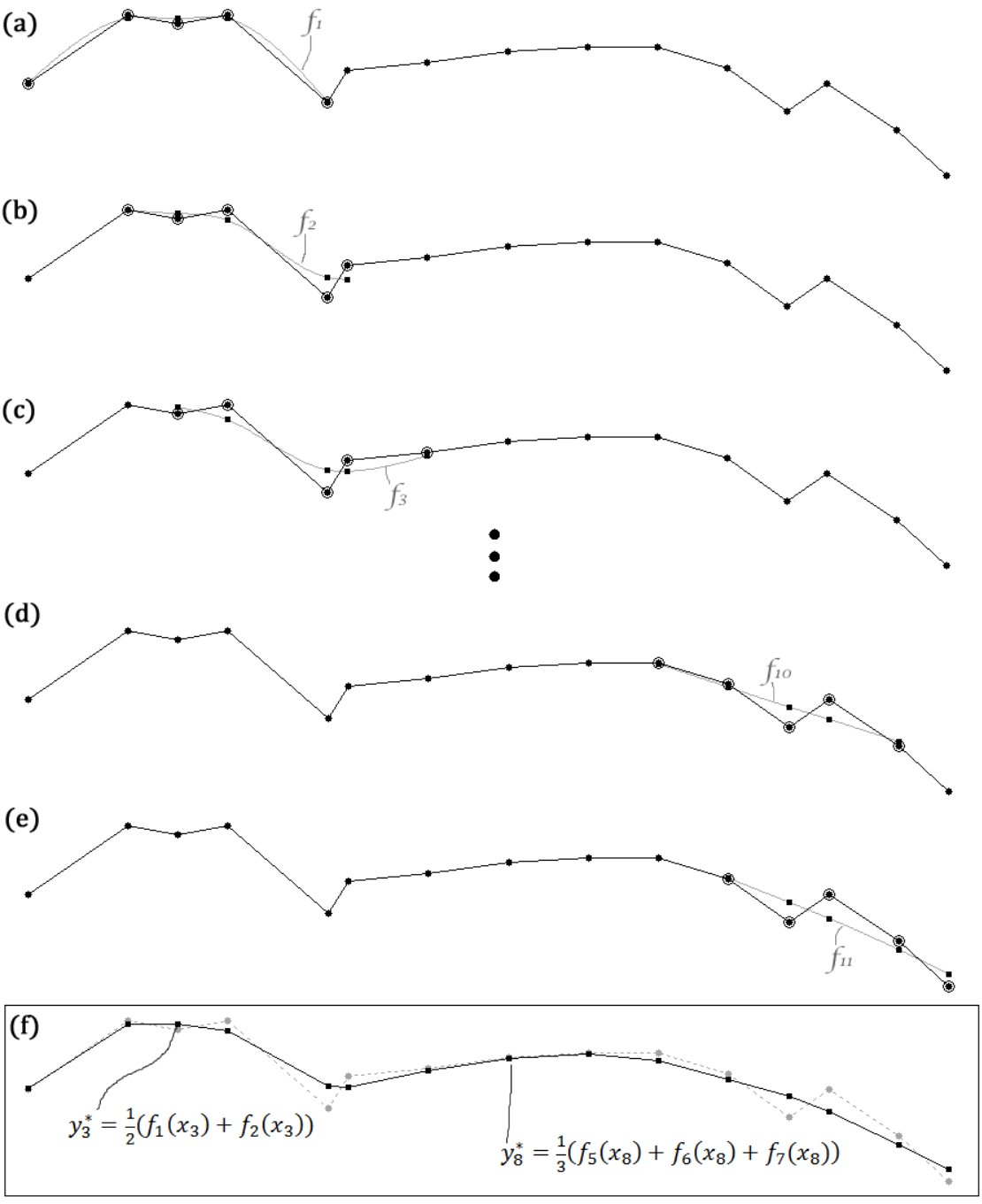

Figure 3.14: *Schematic of overlapping spline smoothing. Window=5. * indicates smoothed value of y. We do not use the endpoints of any of the splines to minimize the effect of the natural boundary conditions.*

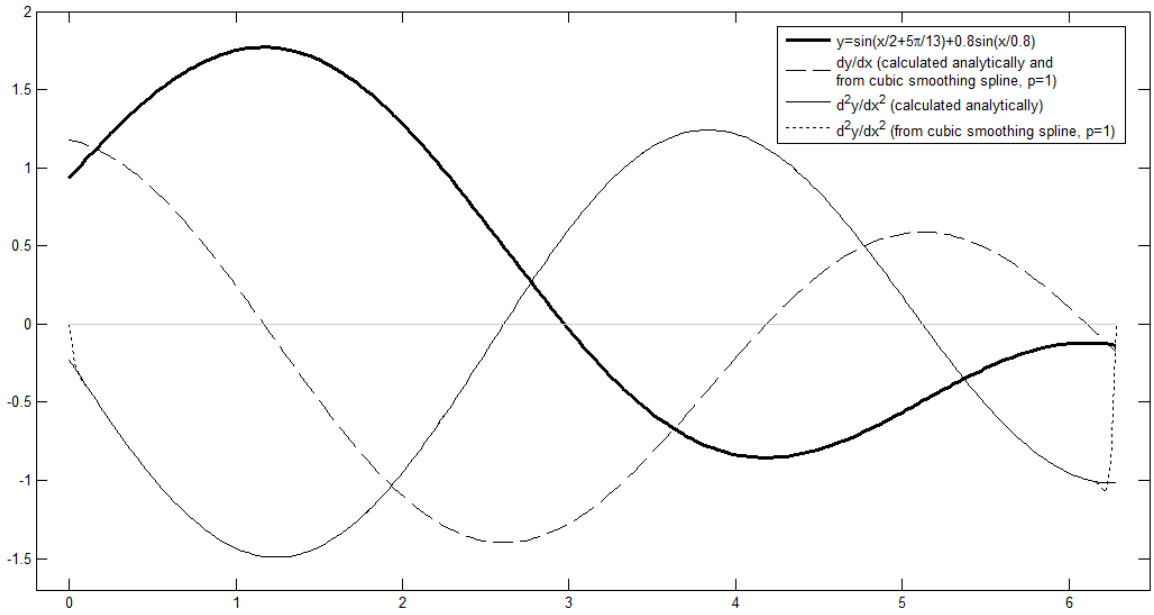

Figure 3.15: *Shows that smoothing spline has natural boundary conditions.*

$s \in [2, 3]$. We sampled each function at 11, 21, 31, 41, and 51 equally-spaced points and then interpolated each set of points parametrically using cubic smoothing splines with $p = 1$. We visually examined each spline to verify that its position closely mimicked that of the original function; each spline was indistinguishable from the original function at the scale of Figure 3.16 (a) and (b). We next differentiated each spline two times and calculated the curvature of the spline using the formula $\kappa(s) = \frac{\frac{dx}{ds}\frac{d^2y}{ds^2} + \frac{dy}{ds}\frac{d^2x}{ds^2}}{[(\frac{dx}{ds})^2 + (\frac{dy}{ds})^2]^{\frac{3}{2}}}$. For the purpose of this example, we define the absolute error between the known and spline-calculated curvature to be acceptably small if it is less than 0.01. Plotting the percentage of "acceptable" curvature values against the percentage of the function's total arc length between consecutive points, we observe a strong negative linear relationship: the more points controlling the spline, the greater the percentage of total arc length that meets our error criterion (Figure 3.16(e)). The specific parameters of the linear relationship vary for the two examples and are likely controlled, at least in part, by the complexity of the original function. This example suggests that the natural boundary conditions will have a much greater effect on the overlapping smoothing splines than the global smoothing spline due to the limited number of points in each local smoothing window.

Consequently, the user of this method faces the challenge of finding a window that is long enough to contain a subset of points near its middle that are not significantly affected by the boundary conditions, yet small enough to use a single value of p over the entire window.

The second limitation of the overlapping smoothing splines is that the benefits of using a global smoothing method, which is a primary attraction of smoothing splines, are lost. Ahnert and Abel (2007) found that global smoothing methods produce derivatives that are two orders of magnitude smoother than those produced by local smoothing methods. We anticipate that averaging values from all splines that overlap a given point will produce some improvement in the smoothness, but examination of the algorithm's output indicates that this averaging is insufficient to compensate for the loss of global smoothing.

The results of using local, overlapping smoothing splines on the noisy decaying chirp are shown in Figures 3.17 and 3.18. In terms of data fidelity, the overlapping splines are clearly superior to the global smoothing spline because they eliminate minor inaccuracies in position while remaining close to the original data at all wavelengths. However, when we compare the overlapping splines' curvature calculation ability with that of the single spline, we observe that the single smoothing spline with p=0.999 outperforms the overlapping smoothing splines in the low-frequency portion of the chirp, while the single smoothing splines with p=0.999 and p=0.999999 both outperform the overlapping smoothing splines in the high-frequency portion of the chirp.

3.4.6 Weighted cubic smoothing spline

Having concluded that the problem of smoothing channel centerlines is best addressed by a global smoothing method, we return our attention to the global smoothing splines, but add a term to the functional that the spline must minimize:

$$p\sum_{j=1}^{n} w_j[y_j - f(x_j)]^2 + (1-p)\int_{x_1}^{x_n} [f''(t)]^2\,dt \tag{3.2}$$

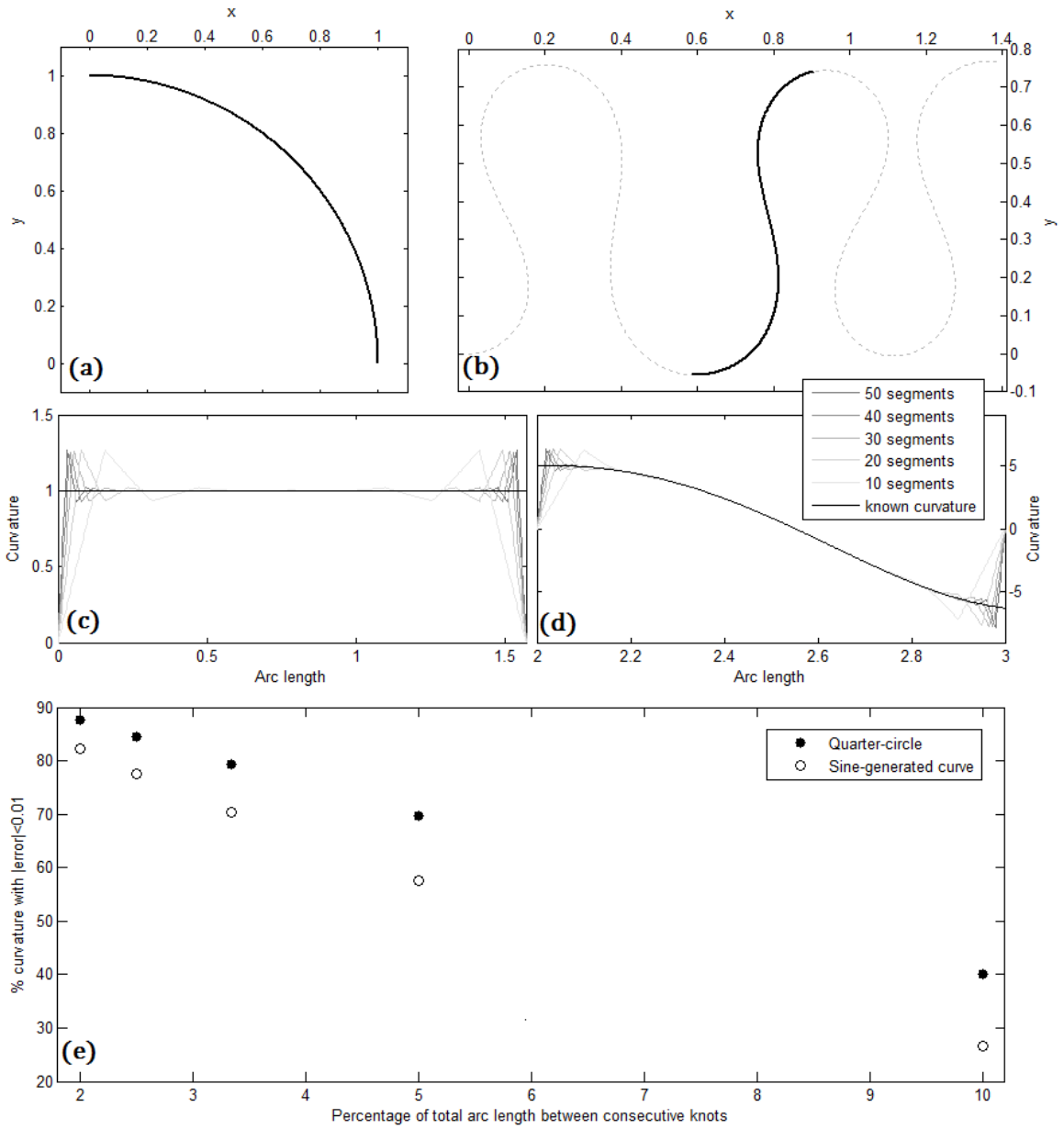

Figure 3.16: *(a) Quarter-circle of radius 1; (b) sine-generated curve with curvature* $\kappa(t) = \frac{3\pi^2}{5}cos(\pi t) + \frac{\pi^2}{10}cos(\frac{2\pi}{1.3}t)$, $t \in [0, 5]$. *The dark portion of the curve is for* $t \in [2, 3]$, *corresponding to (d); (c) curvature calculated for various knot spacings compared to known curvature; (d) curvature of the dark portion of (b) for various knot spacings compared to known curvature; (e) the relationship between knot spacing and the amount of "usable" spline due to the propagation of boundary conditions through the curve.*

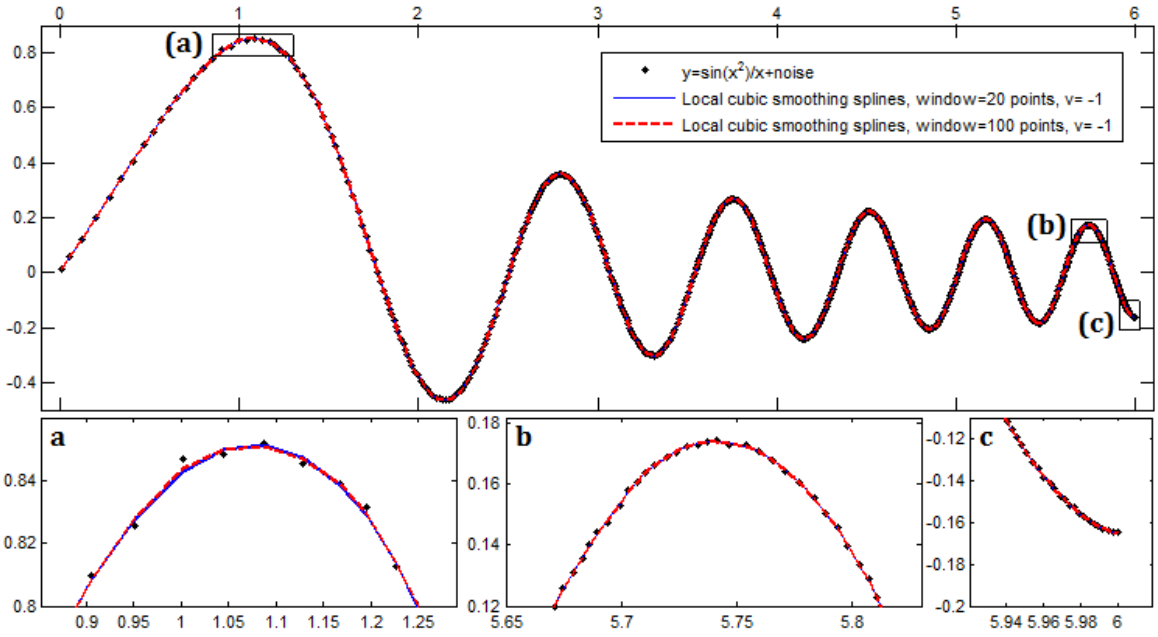

Figure 3.17: *Overlapping splines. Deleted 40% of the data points for window=20 and 16% of the data points for window=100 (values to delete approximated from Figure 3.16.).*

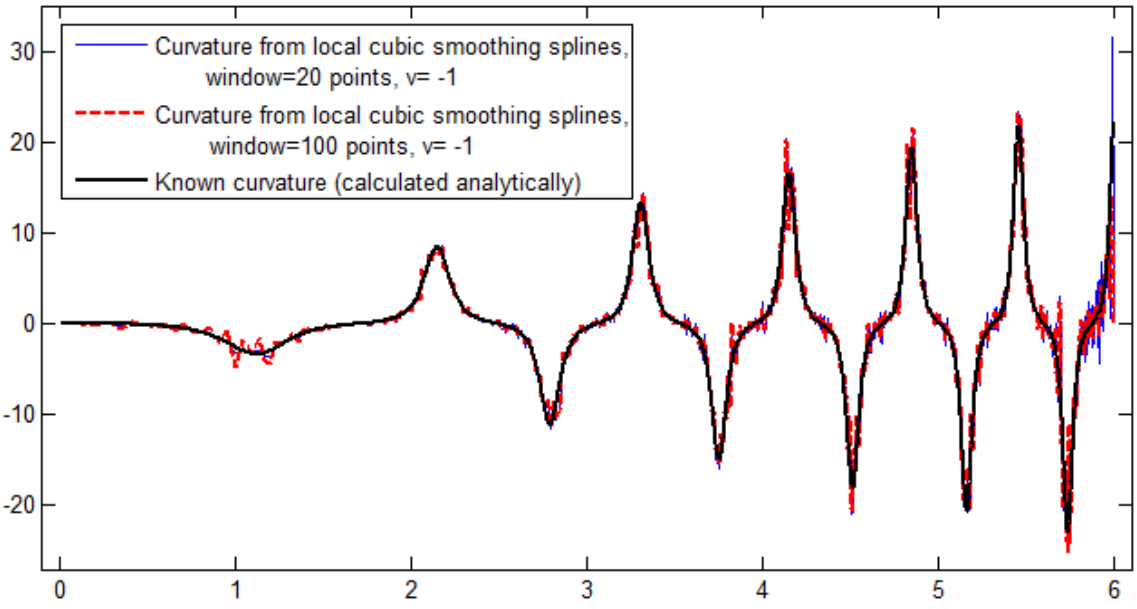

Figure 3.18: *Curvature from overlapping splines.*

(after De Boor, 1978, p. 235; note that $w_j = (\delta y_i)^{-2}$ using De Boor's notation). Here, w_j is a weight indicating the relative importance of data fidelity at the j^{th} point. The literature suggests that w_j should be selected based on the inverse of the variance of y_j (Reinsch, 1967; Woodford, 1970; De Boor, 1978, p. 235); that is, if we had multiple realizations of the same data, a point with greater variability between realizations should be assigned less weight than a point whose value changed very little. For the channel centerlines, we propose a different method of weighting the points in the spline calculation. We have already observed from Figure 3.12 that the global cubic smoothing spline with $p = 0.999$ quite effectively estimates the curvature of the chirp at low frequencies; its primary shortcoming is that it underestimates the curvature at high frequencies by oversmoothing or "cutting corners" on the chirp. Our solution to this problem is to weight the local extrema of the chirp more heavily at the high frequencies (Figure 3.19), incentivizing the spline to remain near these key points while preserving its desirable smoothing ability in the low-frequency regions. The outcome of using this method on the decaying chirp signal is shown in Figure 3.20 and 3.21. The weighted smoothing spline effectively smooths the data at all regions of the curve and produces a very good estimate of the function's known curvature, so this is the method we select for smoothing the channel centerlines.

To smooth the channel centerlines, we implement this method as follows. We select a starting value for p based on the average spacing of the abscissa along the full channel, and we initially give all points an equal weight of $w^{(1)} = 1$. Then the channel centerline points, along with the left and right banks for a sense of scale, are plotted in a graphical user interface in MATLAB. We manually select individual points or spans of points at the high-curvature portions of the centerline and assign weights of $w^{(2)} = 5$ or $w^{(3)} = 25$ depending on our perception of the likelihood of oversmoothing in that region. We perform the interpolation parametrically, using the cumulative Euclidean distance between the points as an estimate for the independent variable, arc length. After creating the piecewise-polynomial form of the smoothing splines for x and y using `csaps`, we plot the smoothed centerline and visually examine it at high magnification to assess the goodness of fit. If the smoothing spline is

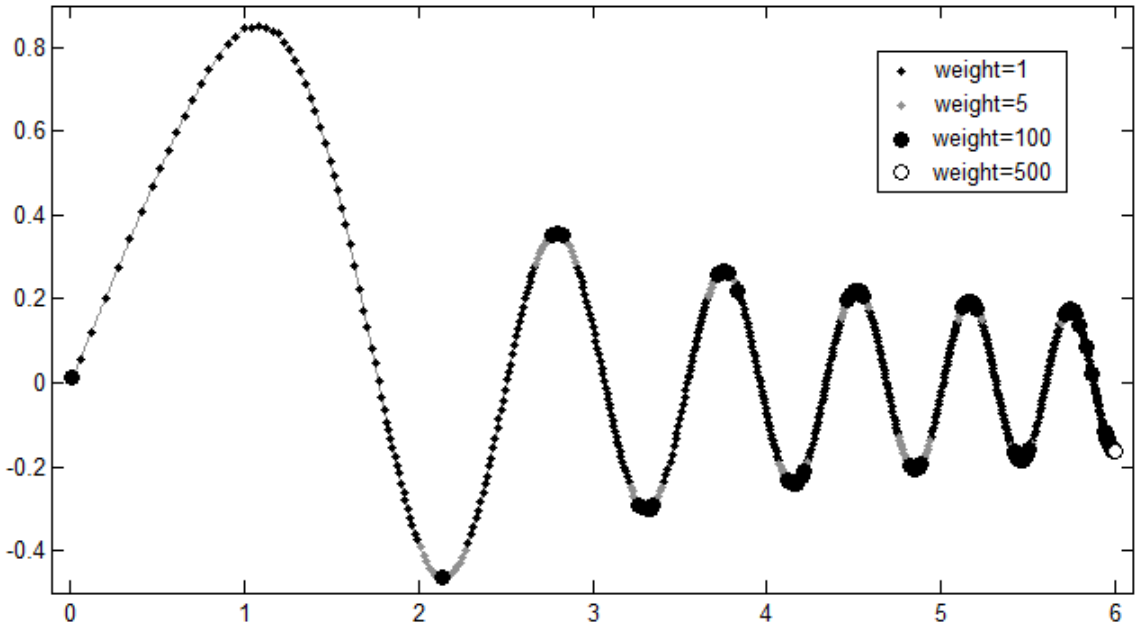

Figure 3.19: *Weights used to calculated weighted cubic smoothing spline.*

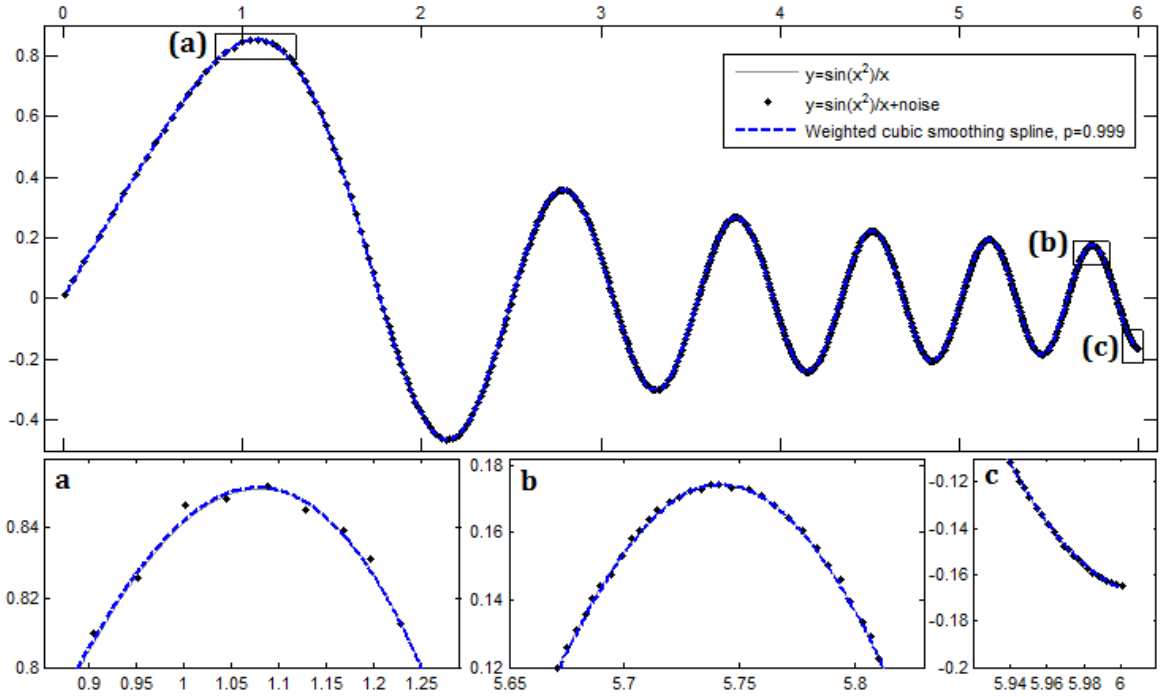

Figure 3.20: *Results from weighted cubic smoothing spline with* $p = 0.999$.

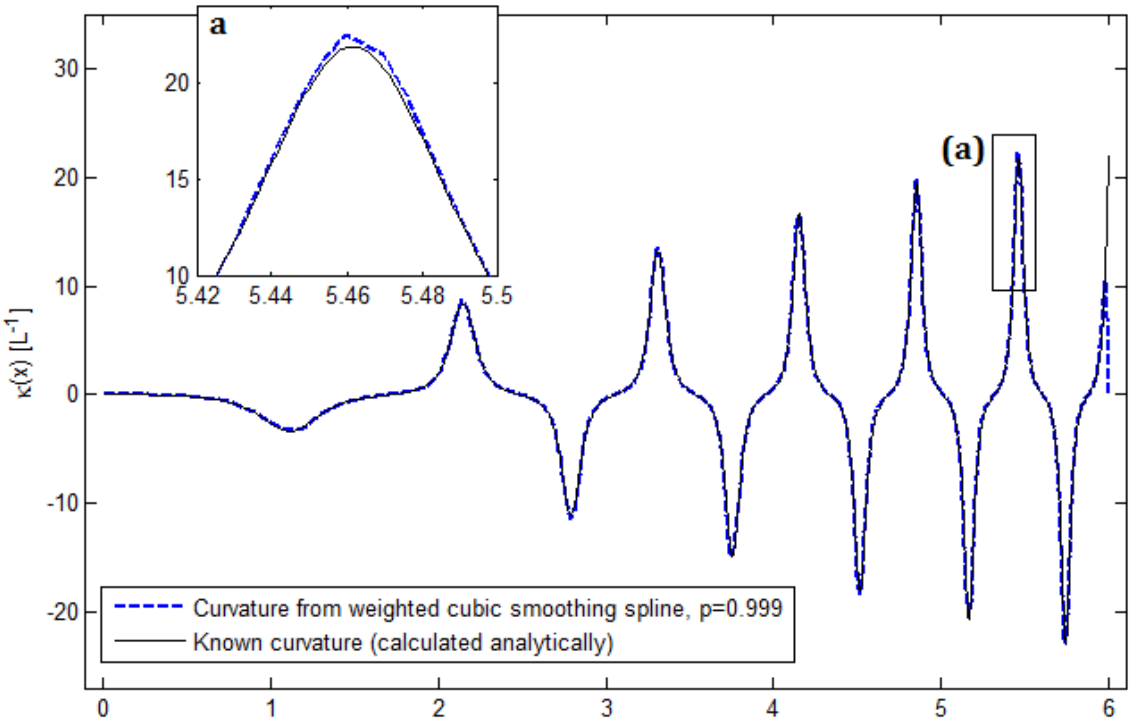

Figure 3.21: *Curvature produced by weighted cubic smoothing spline with* $p = 0.999$.

a poor fit for the entire channel, we recalculate the spline using the existing weights but a lower or higher value of p for more or less smoothing, respectively. If the smoothing spline represents certain portions of the channel well but performs poorly in others, we modify the ratios $w^{(1)}$:$w^{(2)}$, $w^{(1)}$:$w^{(3)}$, and/or $w^{(2)}$:$w^{(3)}$ and again recalculate the spline[2]. On occasion, we also find it necessary to introduce additional weights, as in the case shown in Figure 3.19. We continue making modifications in this manner until the channel's centerline is well represented by the smoothing spline.

Using the final selction of splines, we quadruple the sampling density and calculate x, y, curvature, dx/ds, and dy/ds at each point along the centerline. We replace our initial estimate of cumulative arc length with new values obtained by recalculating the Euclidean distance between the smoothed and densely-sampled points. Other studies (*e.g.*, Güneralp

[2]Observe that increasing or decreasing the average value of $\{w_j\}_{j=1:n}$ has the effect of changing the balance between the error term and the smoothness term in Equation (3.2). It is possible to correct for this by increasing or decreasing the value of p to maintain the original balance. However, in practice we have found this effect to be negligible on the overall behavior of the smoothing spline.

and Rhoads, 2008) have instead used Simpson's rule to calculate the integral form of the arc-length equation. However, our sampled points are so close together that the error introduced by the straight-line approximation is minimal.

3.5 Measuring Channel Widths

Given that a primary goal of this research was to quantify the funnel shape observed at tidal channel mouths, our next task was to measure the width of the channel at equal increments along the centerline. Interestingly, we found that the very idea of "channel width" is not without ambiguity. Pavelsky and Smith (2008) define river flow width as "the shortest cross-sectional distance from water's edge to water's edge, orthogonal to the river channel"; this definition could easily be extended to bankfull width considering that we have already determined the position of the banks. Davies and Woodroffe (2010) define channel width as "the length of a straight-line segment contained within the channel which is almost[3] normal to the centerline". As defining channel width as distance normal to the centerline is conceptually straightforward and simple to implement, we developed a MATLAB algorithm to calculate channel widths under this definition. To run the algorithm, the user manually estimates the maximum width W_{max} of the channel in Google Earth and inputs this value into the MATLAB function. Then, for each point on the centerline, MATLAB creates a line segment of length $2W_{max}$[4] that is centered at the centerline point and has slope $-\frac{dx}{dy} = -\frac{dx/ds}{dy/ds}$.

[3]The word "almost" refers to the fact that these authors define the normal at a point as a line perpendicular to the secant line formed by connecting two centerline points located one shortest-width up and down the channel from the centerline point in question.

[4]In practice, we found that the computation time for this function is significantly reduced if the constraint on the line segment is relaxed such that its length be *greater than* or equal to $2W_{max}$. This allows us to use the triangle inequality rather than the Pythagorean Theorem to find appropriate endpoints for the line. To elaborate, given the coordinates of the centerline point (x_c, y_c) and the slope S of the tangent line to the centerline at that point, we seek the coordinates $(x_{e,L}, y_{e,L})$ of the left endpoint and the coordinates $(x_{e,R}, y_{e,R})$ of the right endpoint of a line segment of length $2W_{max}$ centered at (x_c, y_c) and normal to the tangent. To find $x_{e,L}$, $y_{e,L}$, $x_{e,R}$, and $y_{e,R}$ we must solve the following system of equations: (1) $(x_{e,L} - x_{e,R})^2 + (y_{e,L} - y_{e,R})^2 = (2W_{max})^2$, (2) $\frac{y_{e,L} - y_c}{x_{e,L} - x_c} = -S^{-1}$, (3) $\frac{y_{e,R} - y_c}{x_{e,R} - x_c} = -S^{-1}$, and (4) $\frac{y_{e,L} - y_{e,R}}{xe,L - xe,R} = -S^{-1}$. Note that the first equation is nonlinear. In contrast, if we require only that the line segment's length exceed or equal $2W_{max}$, we simply must find the equation of the line containing the segment: $y - y_c = -S^{-1}(x - x_c)$. Provided that the line is not vertical, the triangle inequality guarantees that substituting $x = W_{max}$ and $x = -W_{max}$ into this equation will produce values of $(x_{e,R}, y_{e,R})$ and $(x_{e,L}, y_{e,L})$ defining a line segment of length greater than or equal to $2W_{max}$. If the line is vertical, we simply let $x_{e,L} = x_{e,R} = x_c$, and $|y_{e,L}| = |y_{e,R}| = W_{max}$. Note that this

The algorithm next calculates all intersections of the left half of the line segment with the left bank of the channel and the right half of the line segment with the right bank of the channel. If one or both intersections do not exist, which is possible only near the enpoints of the channel, that point is eliminated from the centerline. In highly sinuous portions of the channel, as well as in portions of the channel that are much narrower than $2W_{max}$, multiple intersections may exist. If this occurs, the Euclidean distance from the relevant centerline point to each intersection point is calculated; the intersection point corresponding to the shortest distance from the center of the channel is the point that we seek. Finally, the width of the channel corresponding to that point along the centerline is calculated as the Euclidean distance between the normal line's left and right bank intersection points.

Defining the channel width as the intersection of the normal to the centerline with the left and the right banks of the channel works well for reaches of the channel with low to moderate curvature. However, we observe that in very tight meanders, the normal to the centerline often does not intersect the point bar as expected (Figure 3.22). Depending on the value of W_{max} relative to the local width and geometry of the channel, this may result in no intersections of the normal segment with the bank of interest, producing an empty width value, or an intersection with the bank some distance down the channel, producing a spuriously large width value.

Having seen that the normal to the centerline does not, in fact, always measure the shortest distance across the channel–or even a distance reasonably *close* to the shortest distance across the channel–we reconsidered how we might redefine "channel width" to better capture the variable of interest. Rather than attempting to measure the width directly, we considered the possibility of a channel width definition based on measured half-widths along the channel. For each point $P_{C,i}$ on the centerline, we used the MATLAB function `knnsearch` to locate the nearest point $P_{L,i}$ on the left bank and the nearest point $P_{R,i}$ on the right bank. We then computed the half-width as the average of the Euclidean distances $d(P_{C,i}, P_{L,i})$ and $d(P_{C,i}, P_{R,i})$. By definition of the medial axis transform, these two distances should be

modification does not conceptually alter the rest of the algorithm as presented in the text.

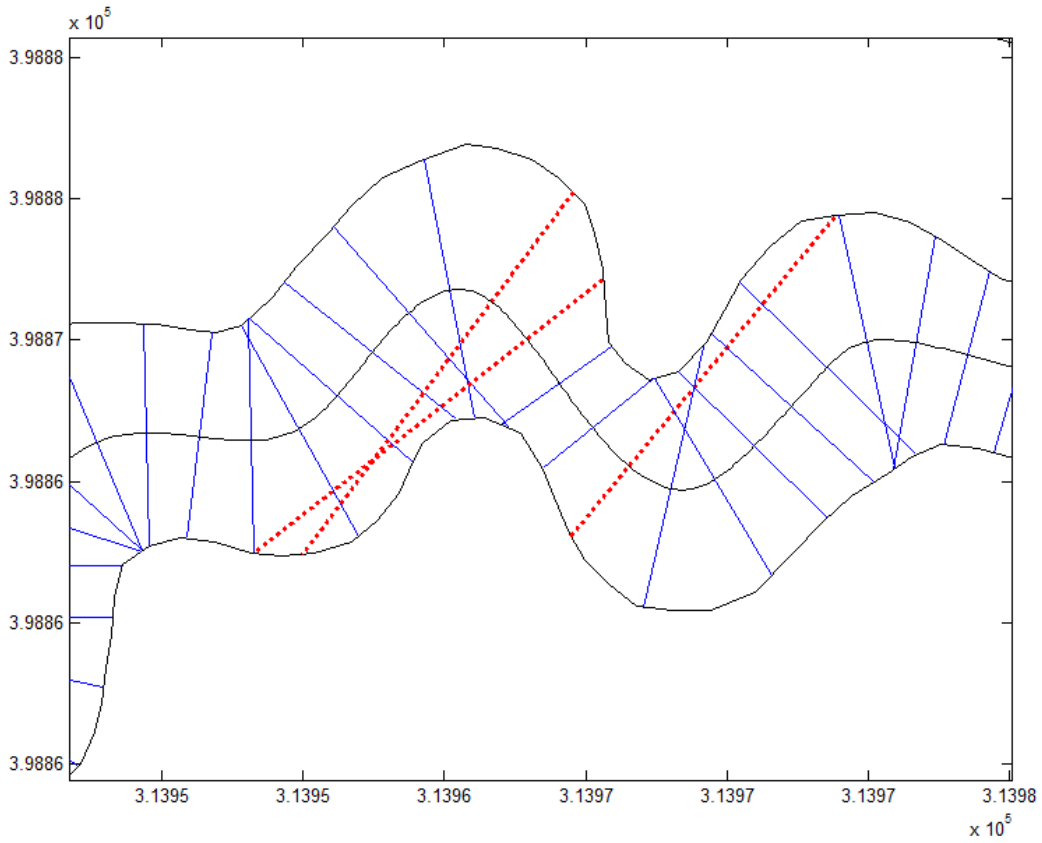

Figure 3.22: *A portion of Channel 102 showing the intersection of every 10th width segment with the left and right banks. Observe that the dashed segments miss the inner (point bar) bank of the meander and intersect the bank at some distance down or upstream, producing spuriously large width measurements at these points.*

equal, but the smoothing procedure described in the previous section may introduce some variability.

This algorithm for measuring channel width performs well in channels of fairly uniform width, but it fails to produce reasonable values in reaches undergoing rapid width changes (Figure 3.23). As we do not require $P_{L,i}$, $P_{C,i}$, and $P_{R,i}$ to be collinear, the nearest point on a given bank may be some distance upstream or downstream from the centerline point of interest. This is particularly problematic within the funnel-shaped tidal channel mouths, where the two width segments always form a pronounced "V" shape that opens upstream. Consequently, we find that defining the half-width of the channel as the average of the shortest distance to each bank results in an underestimate of the quantity of interest.

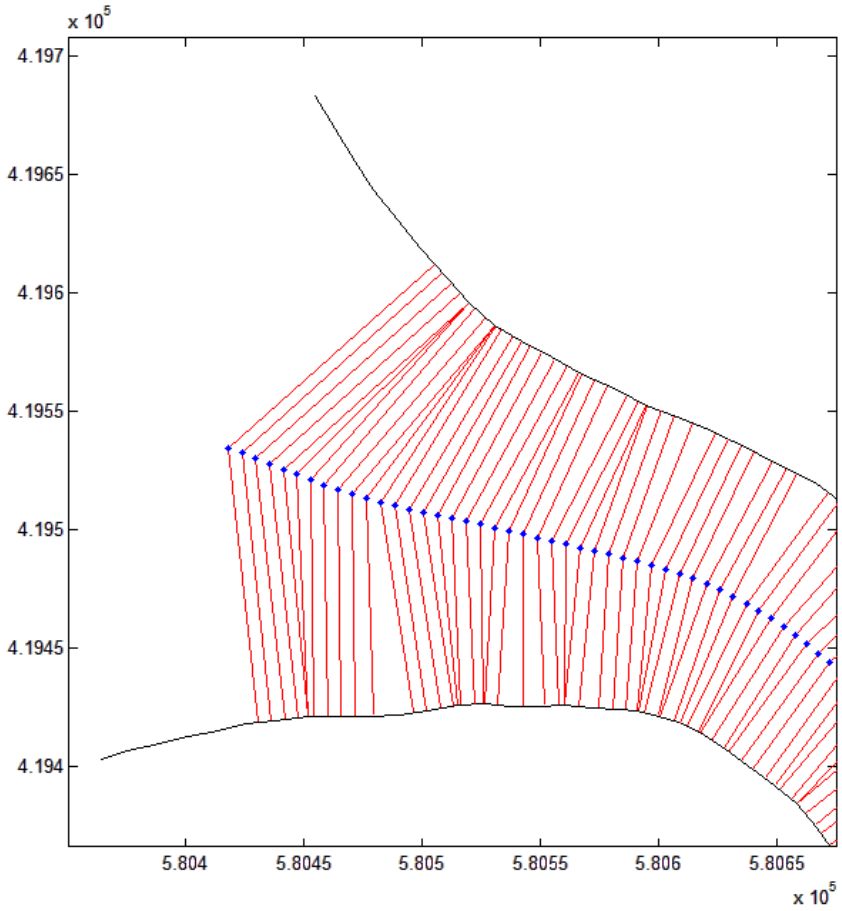

Figure 3.23: *The mouth of Channel 119 with line segments connecting the centerline points to the nearest points on the left and right bank. The width of the channel is clearly underestimated where the channel is rapidly changing in width.*

Based on our observations of the previous two algorithms, we propose a third definition for channel width: the width of the channel at a given point on the centerline $P_{C,i}$ is the shortest cross-channel distance such that $P_{L,i}$, $P_{C,i}$, and $P_{R,i}$ are collinear. In a channel with zero curvature and perfectly uniform banks, this is equivalent to the distance across the channel orthogonal to the centerline. Moreover, this definition allows us to correct for situations in which the normal to the centerline does not intersect the point bar, as in Figure 3.22. In the strictest sense, producing measurements under this definition would require us to rotate a line segment centered at $P_{C,i}$ through a full 180°to ensure that the shortest distance is measured. In practice, however, we observe that the erroneously long normal segments need only be rotated by a small angle to minimize the channel width. Hence our algorithm

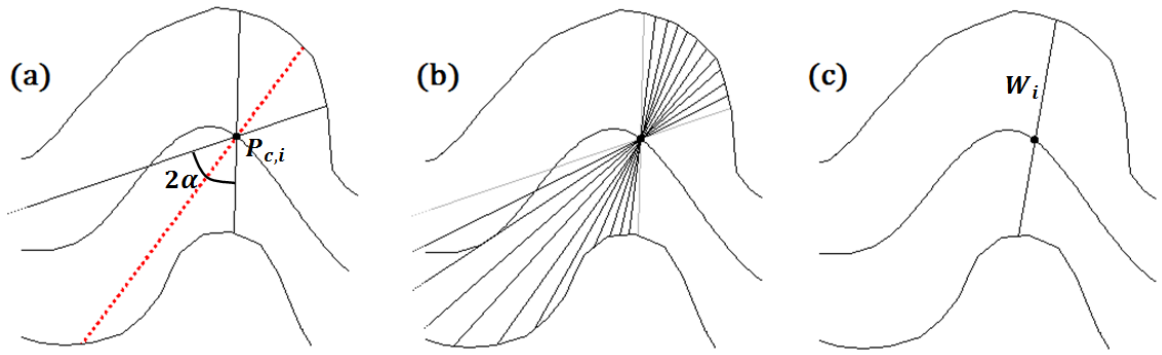

Figure 3.24: *Algorithm for calculating the width of the channel. (a) For each point $P_{C,i}$ along the centerline, we create a search window of angle 2α bisected by the normal to the centerline (dashed line). (b) We rotate a line segment through 1° increments through the search window and calculate the length of the segment at these $2\alpha+1$ points. For readability, not all segments are shown. (c) The minimum-length segment within the search window is the width W_i of the channel at $P_{C,i}$.*

calculates widths as follows (Figure 3.24): we define a search angle α by which the width segment is allowed to deviate from the normal to the channel. Next, for each point along the centerline, we construct a line segment of length $2W_{max}$ containing that point. The segment is rotated about the centerline point through an angle 2α bisected by the normal to the centerline, and the distance between the points at which the segment intersects the banks is calculated at each 1°increment. We then select the minimum of these $2\alpha + 1$ distance measurements as the width of the channel at that point.

A significant drawback of this method is that it is computationally intensive, requiring over an hour to run on a laptop PC (3 GB RAM, 1.5 GHz dual-core processor) for a moderate-length channel (about 5000 centerline points) with $\alpha = 40°$. To decrease the time required to compute channel widths, we first computed the width normal to the centerline at each point. Any points at the beginning or end of the channel for which the normal line did not intersect both banks were thrown out by default. We then selected a subset of points to recalculate using the 2α-window search in the following manner. We computed a trendline for the width data as a function of distance along the channel using linear least squares. We also computed an exponential fit to the data by log-transforming the widths and determined which fit was a better model for the width data based on the R^2 value for each. We next compared the

residual at each data point to the distribution of the residuals; any width with a residual exceeding two standard deviations from the mean residual was marked for recalculation. If there were any points in the middle of the channel for which a width was not found (due to the normal segment missing the point bar and then being too short to reach the bank farther downchannel), they were also added to the list of points to recalculate. Having observed that the erroneous widths tend to occur in clusters, we also automatically recalculated the widths at the 16 points immediately before and after any point meeting the criterion for recalculation. Finally, we recalculated the width at each of these points by searching for the shortest distance across the channel within an $\alpha = 40°$-window.

The last step in our width analysis is to resample our data such that it is equally spaced in arc-length along the channel. From the set of all measured widths along the channel, we select the smallest and divide by eight to determine the final sampling interval in s. We then use linear interpolation of $x(s)$, $y(s)$, $\kappa(s)$, and $W(s)$ to approximate their values at equal spacing. Because we began with 8 points per local width of the channel and then quadrupled the number of points when we created the splines, this final step usually entails downsampling the number of points. The outcome is a set of equally-spaced points (within error) suitable for standard spectral analysis methods.

3.6 Selecting Inflection Points

The final method requiring explanation is our procedure for selecting the inflection points. We initially developed the following algorithm to select the inflection points automatically. We begin with three different models for the width of the channel with respect to arc length: (1) a linear change in width, modeled by $W(s) = As + W_0$; (2) an exponential change in width, modeled by $W(s) = W_0 e^{-s/L_b}$; and (3) a variation on the exponential model in which the width asymptotically approaches a positive constant, that is, $W(s) = (W_0 - W_\infty)e^{-s/L_b} + W_\infty$. Here, $W(s)$ is the width of the channel at s, and L_b is the arc length required for the channel's width to decrease by a factor of e. A, W_0, and W_∞ are fitted parameters referring to the rate of width decrease in meters per meter, the

predicted width of the channel at $s = 0$, and the predicted width of the channel at $s = \infty$, respectively. We find the parameters for the first model using linear least squares. For the second model, we use the nonlinear least squares method described by Davies and Woodroffe (2010). Similarly, we use nonlinear least squares to find the parameters of best fit for model three. Following Davies and Woodroffe (2010), we calculate the R^2 value for each model; whichever model gives the highest R^2 value is the one we will use for our inflection point calculations. An example of a fitted trendline is shown in Figure 3.25(a).

The next step is to normalize the curvature along the channel by the local width; this is necessary because of the observed increase in curvature amplitude upchannel. We multiply each curvature value by the predicted local width, as given by the best-fitting width trendline at that point (Figure 3.25(b)). Finally, we find the average curvature magnitude along the channel and select a percentage of the average as a threshold for meandering. We then evaluate each segment of channel defined by two inflection points (*i.e.*, locations where $\kappa = 0$). If the channel exceeds the threshold curvature value between those two inflection points, we determine that the inflection points are "real"; if not, the inflection points defining that segment of channel are eliminated (Figure 3.25(c) and (d)).

We tested this algorithm with threshold values ranging between 25% and 60%, but we were unable to identify a value that performed well for all channels. In certain locations, the algorithm preserved inflection points that the human eye would likely identify as noise; in other locations, the algorithm deleted "real" inflection points defining what a human viewer would likely identify as a meander (Figure 3.26). Consequently, we found it necessary to manually select the inflection points to keep for each channel. We used the shape of the banks as the primary criterion for which inflection points to keep. If both banks displayed the same sense of curvature as the channel centerline, the half-meander was designated as real. If the apparent meander occurred due to irregularity on only one bank, the inflection points defining that meander were eliminated. By applying this criterion, our goal was to standardize the inflection point selection process; however, we acknowledge that manual inflection point selection introduces the risk biasing the data based on the viewer's idea of

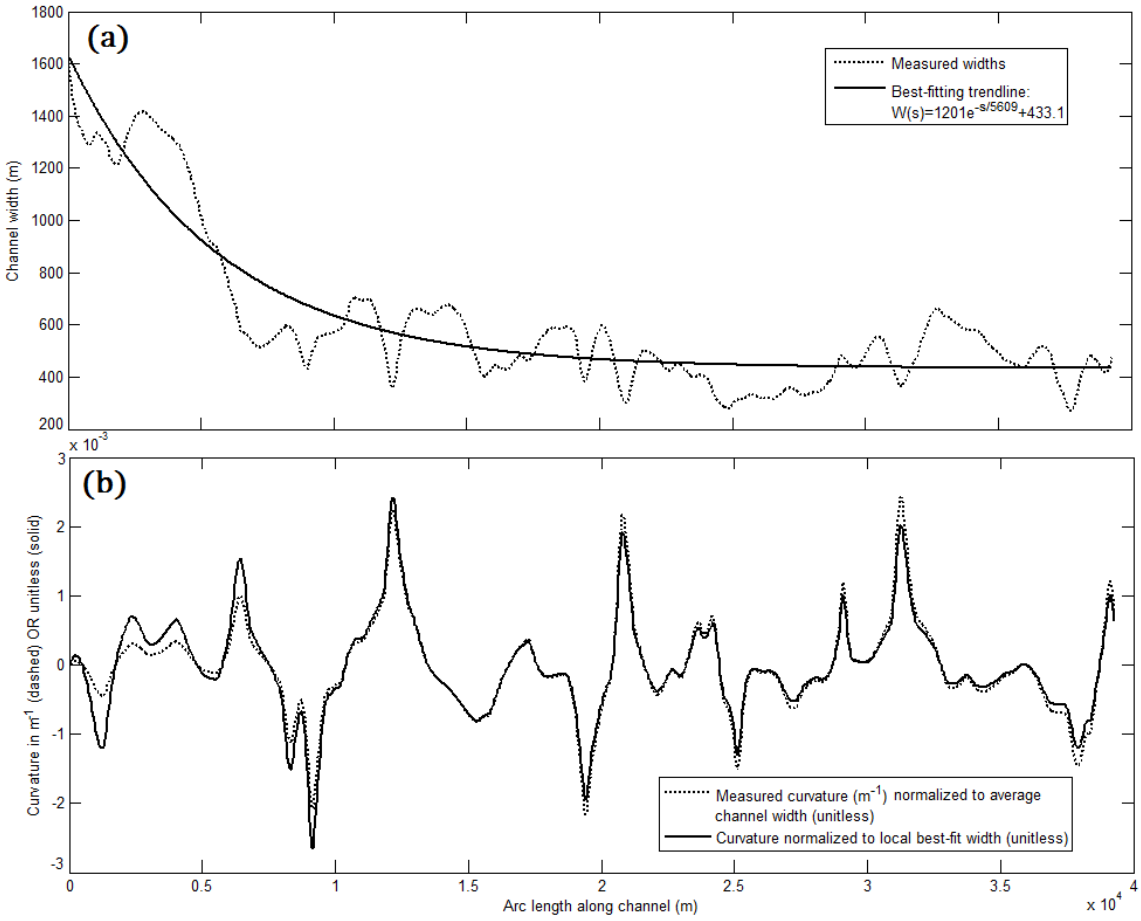

Figure 3.25: *Algorithm for finding the inflection points. Channel 32 is used as an example of a channel in which this algoritm performed well. (a) We find the best-fitting trendline through the channel's measured widths; (b) the curvature series is multiplied by the trendline, thus normalizing the curvature to the local best-fit width of the channel; (c) we set the "meander threshold" as 40% of the mean curvature magnitude. Two consecutive inflection points define a half meander if the curvature between those two inflection points exceeds the threshold curvature magnitude. If the curvature does not exceed the threshold, the inflection points are not considered–see inset; (d) planform map of Channel 32 showing the initial set of inflection points and the final selection of inflection points.*

what a "meander" should look like. We hope to revisit these methods in the future with the goal of creating a more robust automated process for selecting inflection points along a channel.

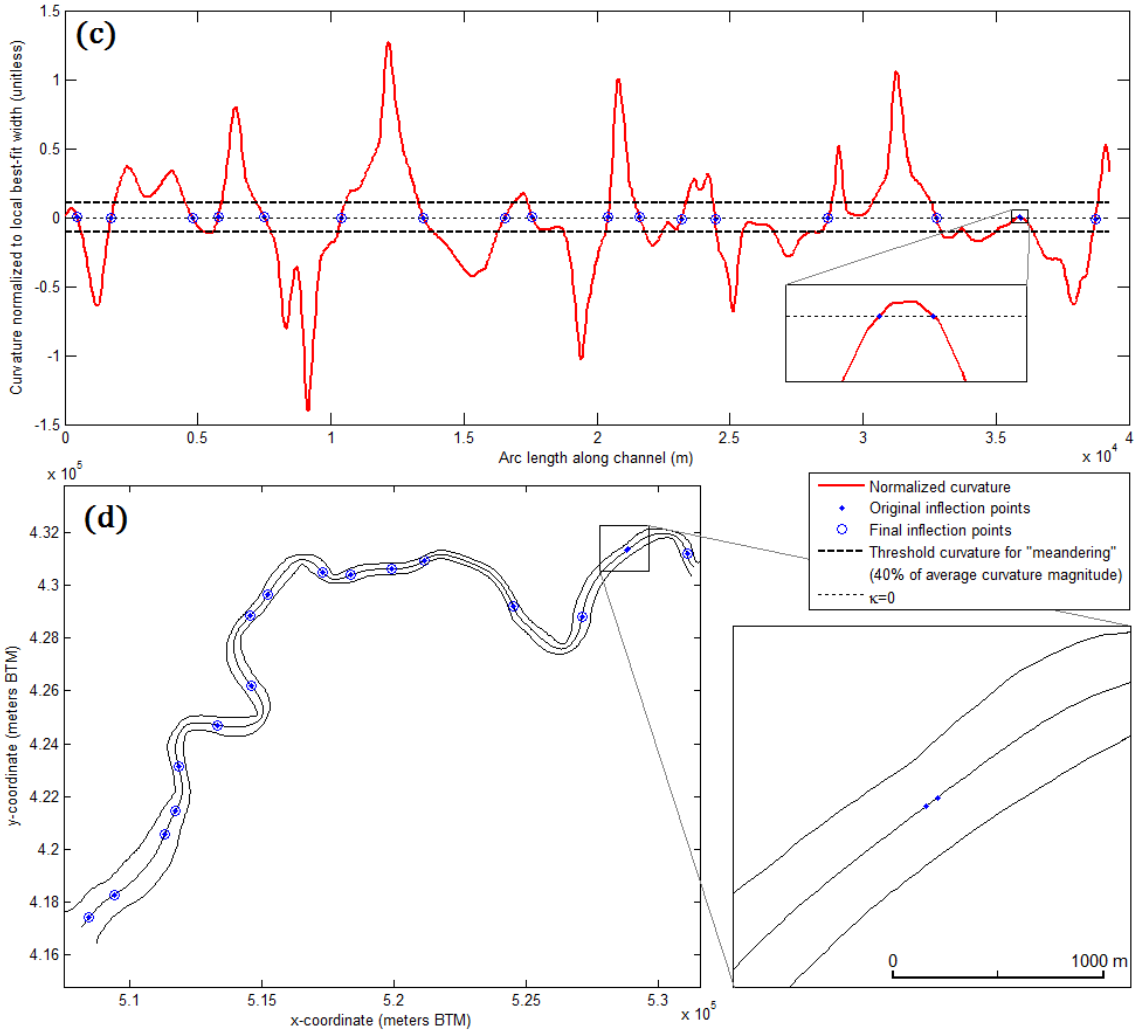

Continuation of Figure 3.25.

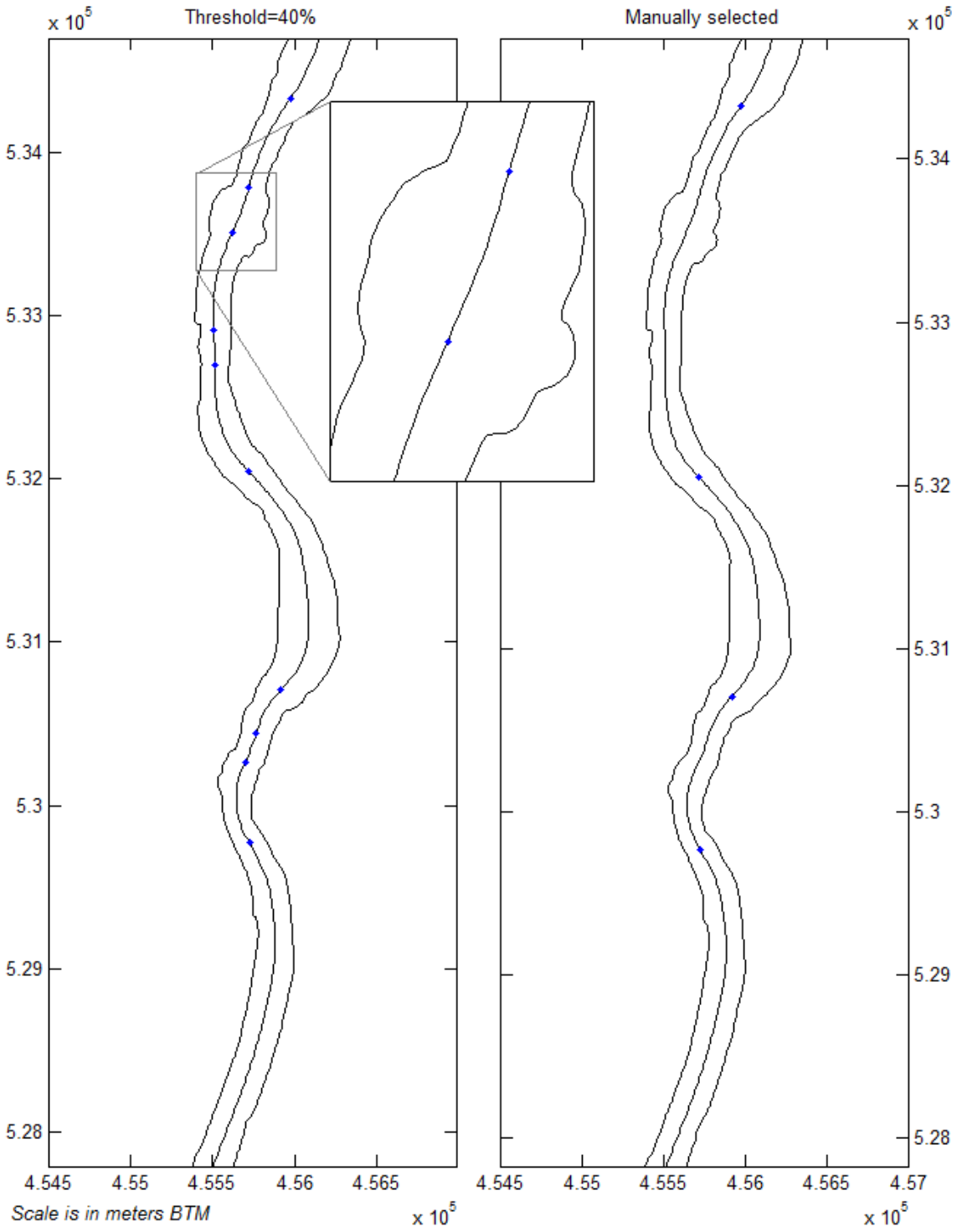

Figure 3.26: *Example of automatic versus manual inflection point selection for a portion of Channel 19. The automatic algorithm retains several half-meanders which the author eliminated based on the shape of the banks. In the inset, the left bank has the opposite sense of curvature as the centerline, leading to the author's conclusion that the automatically-identified half meander should be deleted.*

Bibliography

Abad, J.D., Frias, C.E., Buscaglia, G.C., and Garcia, M.H., 2013, Modulation of the flow structure by progressive bedforms in the Kinoshita meandering channel: *Earth Surface Processes and Landforms*, v. 38, p. 1612-1622. doi: 10.1002/esp.3460.

Abad, J.D., and Garcia, M.H., 2009, Experiments in a high-amplitude Kinoshita meandering channel: 1. Implications of bend orientation on mean and turbulent flow structure: *Water Resources Research*, v. 45, 19 p. doi: 10.1029/2008WR007016.

Angeles, G.R., Perillo, G.M.E., Piccolo, M.C., and Pierini, J.O., 2004, Fractal analysis of tidal channels in the Bahía Blanca Estuary (Argentina): *Geomorphology*, v. 57, p. 263-274. doi: 10.1016/S0169-555X(03)000106-5.

Ahnert, F., 1960, Estuarine meanders in the Chesapeake Bay area: *Geographical Review*, v. 50, p. 390-401.

Ahnert, K., and Abel, M., 2007, Numerical differentiation of experimental data: Local versus global methods: *Computer Physics Communications*, v. 177, p. 764-774. doi: 10/1016/j.cpc.2007.03.009.

Allen, J.R.L., 2000, Morphodynamics of Holocene salt marshes: A review sketch from the Atlantic and southern North Sea coasts of Europe: *Quaternary Science Reviews*, v. 19, p. 1155-1231. doi: 10.1016/S0277-3791(99)00034-7.

Allison, M.A., 1998a, Geological framework and environmental status of the Ganges- Brahmaputra Delta: *Journal of Coastal Research*, v. 14, p. 826-836.

Allison, M.A., 1998b, Historical changes in the Ganges-Brahmaputra delta front: *Journal of Coastal Research*, v. 14, p. 1269-1275.

Allison, M.A., and Kepple, E.B., 2001, Modern sediment supply to the lower delta plain of the Ganges-Brahmaputra River in Bangladesh: *Geo-Marine Letters*, v. 21, p. 66-74. doi: 10.1007/s003670100069.

Allison, M.A., Khan, S.R., Goodbred, Jr., S.L., and Kuehl, S.A., 2003, Stratigraphic evolution of the late Holocene Ganges-Brahmaputra lower delta plain: *Sedimentary Geology*, v. 155, p. 317-342. doi: 10.1016/S0037-0738(02)00185-9.

Aurenhammer, F., 1991, Voronoi diagrams–a survey of a fundamental geometric data struc-

ture: *ACM Computing Surveys*, v. 23, p. 345-405.

Aurenhammer, F., Klein, R., and Lee, D.T., 2013, *Voronoi Diagrams and Delaunay Triangulations*: Hackensack, NJ, World Scientific Publishing Co. Pte. Ltd., 337 p.

Baker, V.R., 2013, Sinuous Rivers: *PNAS*, v. 110, p. 8321-8322. doi: 10.1073/pnas.1306619110.

Barak, P., 1995, Smoothing and differentiation by an adaptive-degree polynomial filter: *Analytical Chemistry*, v. 67, p. 2758-2762. doi: 10.1021/ac00113a006.

Barton, D.C., 1928, Meandering in tidal streams: *Journal of Geology*, v. 36, p. 615-629.

Barua, D.K., 1990, Suspended sediment movement in the estuary of the Ganges- Brahmaputra-Meghna river system: *Marine Geology*, v. 91, p. 243-253. doi: 10.1016/0025-3227(90)90039-M.

Barwis, J.H., 1978, Sedimentology of some South Carolina tidal-creek point bars, and a comparison with their fluvial counterparts, *in* Miall, A.D. (ed.), *Memoir–Canadian Society of Petroleum Geologists*, issue 5: Calgary, Alberta, Canada, Canadian Society of Petroleum Geologists, p. 129-160.

Benker, S.C., Langford, R.P., and Pavlis, T.L., 2011, Positional accuracy of the Google Earth terrain model derived from stratigraphic unconformities in the Big Bend region, Texas, USA: *Geocarto International*, v. 26, p. 291-303. doi: 10.1080/10106049.2011.568125.

Bharati, L., and Jayakody, P., 2011, Hydrological impacts of inflow and land-use changes in the Gorai River catchment, Bangladesh: *Water International*, v. 36, p. 357-369. doi: 10.1080/02508060.2011.586200.

Blondeaux, P., and Seminara, G., 1985, A unified bar-bend theory of river meanders: *Journal of Fluid Mechanics*, v. 157, p. 449-470. doi: 10.1017/S0022112085002440.

Blum, H., 1967, A transformation for extracting new descriptors of shape, *in* Whaten-Dunn, W. (ed.), *Models for the Perception of Speech and Visual Form*: Cambridge, MA, MIT Press, p. 362-380.

Bradie, B., 2005, *A Friendly Introduction to Numerical Analysis*: Upper Saddle River, NJ, Pearson Education, 976 p.

Brandt, J.W., 1994, Convergence and continuity criteria for discrete approximations of the continuous planar skeleton: *CVGIP: Image Understanding*, v. 59, p. 116-124. doi: 10.1006/ciun.1994.1007.

Bridges, P.H., and Leeder, M.R., 1976, Sedimentary models for intertidal mudflat channels with examples from the Solway Firth, Scotland: *Sedimentology*, v. 23, p. 533-552. doi: 10.1111/j.1365-3091.1976.tb00066.x.

Bromba, M.U.A., and Zlegler, H., 1981, Application hints for Savitzky-Golay digital smoothing filters: *Analytical Chemistry*, v. 53, p. 1583-1586.

Browne, M., Mayer, N., and Cutmore, T.R.H., 2007, A multiscale polynomial filter for adaptive smoothing: *Digital Signal Processing*, v. 17, p. 69-75. doi: 10.1016/j.dsp.2006.01.

006.

Burningham, H., 2008, Contrasting geomorphic response to structural control: The Loughros estuaries, northwest Ireland: *Geomorphology*, v. 97, p. 300-320. doi: 10.1016/j.geomorph.2007.08.009.

Campbell, M.R., 1927, Meaning of meanders in tidal streams: *Geological Society of America Bulletin*, v. 38, p. 537-556. doi: 10.1130/GSAB-38-537.

Camporeale, C., Perona, P., Porporato, A., and Ridolfi, L., 2007, Hierarchy of models for meandering rivers and related morphodynamic processes: *Reviews of Geophysics*, v. 45, 28 p. doi: 10.1029/2005RG000185.

Charlton, R., 2008, *Fundamentals of Fluvial Geomorphology*: London, Routledge, 234 p.

Chatterjee, M., Shankar, D., Sen, G.K., Sanyal, P., Sundar, D., Michael, G.S., Chatterjee, A., Amol, P., Mukherjee, D., Suprit, K., Mukherjee, A., Vijith, V., Chatterjee, S., Basu, A., Das, M., Chakraborti, S., Kalla, A., Kanta Misra, S., Mukhopadhyay, S., Mandal, G., and Sarkar, K., 2013, Tidal variations in the Sundarbans estuarine system, India: *Journal of Earth System Science*, v. 122, p. 899-933. doi: 10.1007/s12040-013-0314-y.

Cleveringa, J., and Oost, A.P., 1999, The fractal geometry of tidal-channel systems in the Dutch Wadden Sea: *Geologie en Mijnbouw*, v. 78, p. 21-30. doi: 10.1023/A:10037790 15372.

Coco, G., Zhou, Z., van Maanen, B., Olabarrieta, M., Tinoco, R., and Townend, I., 2013, Morphodynamics of tidal networks: Advances and challenges: *Marine Geology*, v. 346, p. 1-16. doi: 10.1016/j.margeo.2013.08.005.

Coleman, J.M., 1969, Brahmaputra River: Channel processes and sedimentation: *Sedimentary Geology*, v. 3, p. 129-239. doi: 10.1016/0037-0738(69)90010-4.

Coleman, J.M., Huh, O.K., and Braud, Jr., D., 2008, Wetland loss in world deltas: *Journal of Coastal Research*, v. 24, p. 1-14.

Constantine, J.A., and Dunne, T., 2008, Meander cutoff and the controls on the production of oxbow lakes: *Geology*, v. 36, p. 23-26.

D'Alpaos, A., Lanzoni, S., Mudd, S.M., and Fagherazzi, S., 2006, Modeling the influence of hydroperiod and vegetation on the cross-sectional formation of tidal channels: *Estuarine, Coastal, and Shelf Science*, v. 69, p. 311-324. doi: 10.1016/j.ecss.2006.05.002.

Dalrymple, R.W., and Choi, K., 2007, Morphologic and facies trends through the fluvial-marine transition in tide-dominated depositional systems: A schematic framework for environmental and sequence-stratigraphic interpretation: *Earth-Science Reviews*, v. 81, p. 135-174. doi: 10.1016/j.earscierev.2006.10.002.

Dalrymple, R.W., Mackay, D.A., Ichaso, A.A., and Choi, K.S., 2012, Processes, morphodynamics, and facies of tide-dominated estuaries, *in* Davis, Jr., R.A., and Dalrymple, R.W. (eds.), *Principles of Tidal Sedimentology*: New York, Springer Science and Business Media, p. 79-108. doi: 10.1007/978-94-007-0123-6_5.

Dalrymple, R.W., Zaitlin, B.A., and Boyd, R., 1992, Estuarine facies models: Conceptual basis and stratigraphic implications: *Journal of Sedimentary Petrology*, v. 62., p. 1130-1146.

Davies, G., 2011, *Downstream changes in the cross-sectional shape of tidal channels*: Wollongong, Australia, University of Wollongong, Ph.D. thesis, 404 p.

Davies, G., and Woodroffe, C.D., 2010, Tidal estuary width convergence: Theory and form in North Australian estuaries: *Earth Surface Processes and Landforms*, v. 35, p. 737-749. doi: 10.1002/esp.1864.

De, C., 2009, Sundarban delta complex: *Indian Journal of Geosciences*, v. 63, p. 397-428.

De Boor, C., 1978, *A Practical Guide to Splines*: New York, Springer-Verlag, 392 p.

Dietrich, W.E., Smith, J.D., and Dunne, T., 1979, Flow and sediment transport in a sand bedded meander: *Journal of Geology*, v. 87, p. 305-315. doi: 10.1086/628419.

Douglas, D.H., and Peucker, T.K., 1973, Algorithms for the reduction of the number of points required to represent a digitized line or its caricature: *Canadian Cartographer*, v. 10, p. 112-122.

Dury, G.H., 1971, Channel characteristics in a meandering tidal channel: *Geografiska Annaler*, v. 53A, p. 188-197.

Eilers, P.H.C., 2003, A perfect smoother: *Analytical Chemistry*, v. 75, p. 3631-3636.

Eisma, D., 1998, *Intertidal Deposits: River Mouths, Tidal Flats, and Coastal Lagoons*: Boca Raton, FL, CRC Press, 525 p.

Ensign, S.H., Doyle, M.W., and Piehler, M.F., 2013, The effect of tide on the hydrology and morphology of a freshwater river: *Earth Surface Processes and Landforms*, v. 38, p. 655-660. doi: 10.1002/esp.3392.

Ericson, J.P., Vörösmarty, C.J., Dingman, S.L., Ward, G.L., and Meybeck, M., 2006, Effective sea-level rise and deltas: Causes of change and human dimension implications: *Global and Planetary Change*, v. 50, p. 63-82. doi: 10.1016/j.gloplacha.2005.07.004.

Fagherazzi, S., 2008, Self-organization of tidal deltas: *PNAS*, v. 105, p. 18,692-18,695. doi: 10.1073/pnas0806668105.

Fagherazzi, S., Bortoluzzi, A., Dietrich, W.E., Adami, A., Lanzoni, S., Marani, M., and Rinaldo, A., 1999, Tidal networks: 1. Automatic network extraction and preliminary scaling features from digital terrain maps: *Water Resources Research*, v. 35, p. 3891-3904. doi: 10.1029/1999WR900236.

Fagherazzi, S., and Furbish, D.J., 2001, On the shape and widening of salt marsh creeks: *Journal of Geophysical Research*, v. 106(C1), p. 991-1003.

Fagherazzi, S., Gabet, E.J., and Furbish, D.J., 2004, The effect of bidirectional flow on tidal channel planforms: *Earth Surface Processes and Landforms*, v. 29, p. 295-309. doi: 10.1002/esp.1016.

Fagherazzi, S., and Sun, T., 2004, A stochastic model for the formation of channel networks in tidal marshes: *Geophysical Research Letters*, v. 31, 4 p., L21503. doi: 10.1029/2004GL020965.

Farr, T.G., Rosen, P.A., Caro, E., Crippen, R., Duren, R., Hensley, S., Kobrick, M., Paller, M., Rodriguez, E., Roth, L., Seal, D., Shaffer, S., Shimada, J., Umland, J., Werner, M., Oskin, M., Burbank, D., and Alsdorf, D., 2007, The shuttle radar topography mission: *Reviews of Geophysics*, v. 45, 33 p., RG2004. doi: 10.1029/2005RG000183.

Ferguson, R.I., 1975, Meander irregularity and wavelength estimation: *Journal of Hydrology*, v. 26, p. 315-333. doi: 10.1016/0022-1694(75)90012-8.

Ferguson, R.I., 1976, Disturbed periodic model for river meanders: *Earth Surface Processes*, v. 1, p. 337-347. doi: 10.1002/esp.3290010403.

Ferguson, R.I., 1979, River meanders: Regular or random?, *in* Wrigley, N. (ed.), *Statistical Applications in the Spatial Sciences*: London, Pion, p. 228-241.

Fisher, G.B., Amos, C.B., Bookhagen, B., Burbank, D.W., and Godard, V., 2012, Channel widths, landslides, faults, and beyond: The new world order of high-spatial resolution Google Earth imagery in the study of earth surface processes: *Geological Society of America Special Papers*, v. 492, p. 1-22.

Food and Agriculture Organization of the United Nations, 2007, *The World's Mangroves, 1980-2005: A Thematic Study in the Framework of the Global Forest Resource Assessment 2005 (FAO Forestry Paper 153)*: Rome, United Nations, 77 p.

Frascati, A., and Lanzoni, S., 2009, Morphodynamic regime and long-term evolution of meandering rivers: *Journal of Geophysical Research*, v. 114, 12 p., F02002. doi: 10.1029/2008JF001101.

Friedkin, J.F., 1945, *A Laboratory Study of the Meandering of Alluvial Rivers*: Vicksburg, MS, U.S. Army Corps of Engineers, 114 p.

Friedrichs, C.T., and Aubrey, D.G., 1994, Tidal propagation in strongly convergent channels: *Journal of Geophysical Research*, v. 99 (C2), p. 3321-3336.

Gani, R., and Alam, M., 2003, Sedimentation and basin-fill history of the Neogene clastic succession exposed in the southeastern fold belt of the Bengal Basin, Bangladesh: A high-resolution sequence stratigraphic approach: *Sedimentary Geology*, v. 155, p. 227-270. doi: 10.1016/S0037-0738(02)00182-3.

Gao, S., and Collins, M., 1994, Tidal inlet equilibrium, in relation to cross-sectional area and sediment transport patterns: *Estuarine, Coastal, and Shelf Science*, v. 38, p. 157-172. doi: 10.1006/ecss.1994.1010.

Gardner, L.R., and Bohn, M., 1980, Geomorphic and hydraulic evolution of tidal creeks on a subsiding beach ridge plain, North Inlet, S.C.: *Marine Geology*, v. 34, p. M91-M97. doi: 10.1016/0025-3227(80)90067-5.

Ghosh, A.K., and Scheidegger, A.E., 1971, A study of natural wiggly lines in hydrology:

Journal of Hydrology, v. 13, p. 101-126. doi: 10.1016/0022-1694(71)90209-5.

Ghulam Kibria, A.M.M., 1972, A short note on the fluvial morphology of the Brahmaputra River in Bangladesh, *in* Mukherjee, A., Biswas, B.R., Kurien, T.K., and Chandak, G.J. (eds.), *Miscellaneous Publication No. 46: Proceedings of the Seminar on Fluvial Processes and Geomorphology of the Brahmaputra Basin: A Collection of Papers Presented at the Seminar Held on October 5-6, 1972, in Calcutta*: Calcutta, Geological Survey of India, p. 11-20.

Goodbred, Jr., S.L., and Kuehl, S.A., 1999, Holocene and modern sediment budgets for the Ganges-Brahmaputra river system: Evidence for highstand dispersal to flood-plain, shelf, and deep-sea depocenters: *Geology*, v. 27, p. 559-562.

Goodbred, Jr., S.L., and Kuehl, S.A., 2000, The significance of large sediment supply, active tectonism, and eustasy on margin sequence development: Late Quaternary stratigraphy and evolution of the Ganges-Brahmaputra delta: *Sedimentary Geology*, v. 133, p. 227-248. doi: 10.1016/S0037-0738(00)00041-5.

Gorry, P.A., 1991, General least-squares smoothing and differentiation of nonuniformly spaced data by the convolution method: *Analytical Chemistry*, v. 63, p. 534-536. doi: 10.1021/ac00205a007.

Green, P.J., and Silverman, B.W., 1994, *Nonparametric Regression and Generalized Linear Models: A Roughness Penalty Approach*: Boca Raton, FL, CRC Press, 184 p.

Guccione, M.J., 1983, Causes of channel variations, Red River, Arkansas, *in* Elliott, C.M. (ed.), 1984, *River Meandering: Proceedings of the Conference Rivers '83*: New York, American Society of Civil Engineers, p. 101-112.

Güneralp, İ, Abad, J.D., Zolezzi, G., and Hooke, J., 2012, Advances and challenges in meandering channels research: *Geomorphology*, v. 163-164, p. 1-9. doi: 10.1016/j.geomorph.2012.04.011.

Güneralp, İ, and Marston, R.A., 2012, Process-form linkages in meander morphodynamics: Bridging theoretical modeling and real-world complexity: *Progress in Physical Geography*, v. 36, p. 718-746. doi: 10.1177/0309133312451989.

Güneralp, İ, and Rhoads, B.L., 2008, Continuous characterization of the planform geometry and curvature of meandering rivers: *Geographical Analysis*, v.40, p. 1-25. doi:10.1111/j.0016-7363.2007.00711.x.

Gutierrez, R.R., and Abad, J.D., 2014, On the analysis of the medium term planform dynamics of meandering rivers: *Water Resources Research*, v. 50, 20 p. doi: 10.1002/2012WR013358.

Gutierrez, R.R., Abad, J.D., Choi, M., and Montoro, H., 2014, Characterization of confluences in free meandering rivers of the Amazon basin: *Geomorphology*, v. 220, p. 1-14. doi: 10.1016/j.geomorph.2014.05.011.

Hack, J.T., 1957, *Studies of longitudnial stream profiles in Virginia and Maryland* (USGS Professional Paper 294-B): Washington, D.C., United States Government Printing Of-

fice, 52 p.

Hossain, M.A., Gan, T.W., and Baki, A.B.M., 2013, Assessing morphological changes of the Ganges River using satellite images: *Quaternary International*, v. 304, p. 142-155. doi: 10.1016/j.quaint.2013.03.028.

Howard, A.D., and Hemberger, A.T., 1991, Multivariate characterization of meandering: *Geomorphology*, v. 4, p. 161-186.

Howard, A.D., and Knutson, T.R., 1984, Sufficient conditions for river meandering: A simulation approach: *Water Resources Research*, v. 20, p. 1659-1667. doi: 10.1029/WR020i01 1p01659.

Hughes, Z.J., 2012, Tidal channels on tidal flats and marshes, *in* Davis, Jr., R.A., and Dalrymple, R.W. (eds.), *Principles of Tidal Sedimentology*: New York, Springer Science and Business Media, p. 269-301. doi: 10.1007/978-94-007-0123-6_11.

Iftekhar, M.S., and Saenger, P., 2008, Vegetation dynamics in the Bangladesh Sundarbans mangroves: A review of forest inventories: *Wetlands Ecology and Management*, v. 16, p. 291-312. doi: 10.1007/s11273-007-9063-5.

Ikeda, S., Parker, G., and Sawai, K., 1981, Bend theory of river meanders. Part 1. Linear development: *Journal of Fluid Mechanics*, v. 112, p. 363-377. doi: 10.1017/S0022112081 000451.

Jakubowska, M., and Kubiak, W.W., 2004, Adaptive-degree polynomial filter for voltammetric signals: *Analytica Chimica Acta*, v. 512, p. 241-250. doi: 10.1016/j.aca.2004. 03.007.

Johannesson, H., and Parker, G., 1989, Linear theory of river meanders, *in* Ikeda, S., and Parker, G. (eds.) *River Meandering, Water Resources Monograph*, v. 12: Washington, D.C., American Geophysical Union, p. 181-214.

Johnson, D., 1929, Meanders in tidal streams: A review and discussion: *Geographical Review*, v. 19, p. 135-139.

Kleinhans, M.G., Schuurman, F., Bakx, W., and Markies, H., 2009, Meandering channel dynamics in highly cohesive sediment on an intertidal mud flat in the Westerschelde Estuary, the Netherlands: *Geomorphology*, v. 105, p. 261-276. doi: 10.1016/j.geomorph. 2008.10.005.

Knighton, D., 1984, *Fluvial Forms and Processes*: London, Edward Arnold Ltd., 218 p.

Knighton, A.D., Woodroffe, C.D., and Mills, K., 1992, The evolution of tidal creek networks, Mary River, northern Australia: *Earth Surface Processes and Landforms*, v. 17, p. 167-190. doi: 10.1002/esp.3290170205.

Kopsick, P.R., 1983, Dimensions of modern and relict meander loops of selected rivers in Kansas and Nebraska, *in* Elliott, C.M. (ed.), 1984, *River Meandering: Proceedings of the Conference Rivers '83*: New York, American Society of Civil Engineers, p. 138-146.

Kuehl, S.A., Allison, M.A., Goodbred, S.L., and Kudrass, H., 2005, The Ganges-Brahmaputra

Delta, *in* Gosian, L., and Bhattacharya, J. (eds.), 2005, *SEPM Special Publication no. 83: River Deltas–Concepts, Models, and Examples*: Tulsa, OK, SEPM Society for Sedimentary Geology, p. 413-434.

Kumar, B., Gopinath, G., and Chandran, M., 2014, River sinuosity in a humid tropical river basin, south west coast of India: *Arabian Journal of Geosciences*, v. 7, p. 1763-1772. doi: 10.1007/s12517-013-0864-y.

Lal, R., Fifield, L.K., Tims, S.G., Wasson, R.J., and Howe, D., 2012, A study of soil formation rates using ^{10}Be in the wet-dry tropics of northern Australia: *EPJ Web of Conferences*, v. 35, 5 p. doi: 10.1051/epjconf/20123501001.

Langbein, W.B., 1963, The hydraulic geometry of a shallow estuary: *Bulletin of the International Association of Scientific Hydrology*, v. 8, p. 84–94.

Langbein, W.B., and Leopold, L.B., 1966, *River Meanders—Theory of Minimum Variance* (Geological Survey Professional Paper 422-H): Washington, D.C., United States Government Printing Office, 21 p.

Lanzoni, S., and Seminara, G., 1998, On tide propagation in strongly convergent estuaries: *Journal of Geophysical Research*, v. 103 (C13), p. 30,793-30,812.

Lanzoni, S., and Seminara, G., 2002, Long-term evolution and morphodynamic equilibrium of tidal channels: *Journal of Geophysical Research*, v. 107 (C1), 13 p. doi: 10.1029/2000JC000468.

Lazarus, E.D., and Constantine, J.A., 2013, Generic theory for channel sinuosity: *PNAS*, v. 110, p. 8447-8452. doi: 10.1073/pnas.1214074110.

Lee, D.T., 1982, Medial axis transform of a planar shape: *IEEE Transactions on Pattern Analysis and Machine Intelligence*, v. PAMI-4, p. 363-369.

Legleiter, C.J., and Kyriakidis, P.C., 2006, Forward and inverse transformations between Cartesian and channel-fitted coordinate systems for meandering rivers: *Mathematical Geology*, v. 38, p. 927-958.

Leopold, L.B., and Langbein, W.B., 1966, River meanders: *Scientific American*, v. 214, p. 60-70. doi: 10.1038/scientificamerican0666-60.

Leopold, L.B., and Maddock, Jr., T., 1953, *The Hydraulic Geometry of Stream Channels and Some Physiographic Implications* (USGS Professional Paper 252): Washington, D.C., United States Government Printing Office, 64 p.

Leopold, L.B., and Wolman, M.G., 1957, *River Channel Patterns: Braided, Meandering, and Straight* (USGS Professional Paper 282-B): Washington, D.C., United States Government Printing Office, 51 p.

Leopold, L.B., and Wolman, M.G., 1960, River meanders: *Bulletin of the Geological Society of America*, v. 71, p. 769-794. doi: 10.1130/0016-7606.

Leopold, L.B., Wolman, M.G., and Miller, J.P., 1964, *Fluvial Processes in Geomorphology*: San Francisco, W.H. Freeman and Company, 522 p.

Lisle, R.J., 2006, Google Earth: A new geological resource: *Geology Today*, v. 22, p. 29-32. doi: 10.1111/j.1365-2451.2006.00546.x.

Luo, J., Ying, K., He, P., and Bai, J., 2005, Properties of Savitzky-Golay digital differentiators: *Digital Signal Processing*, v. 15, p. 122-136. doi: 10.1016/j.dsp.2004.09.008.

Marani, M., Lanzoni, S., and Zandolin, D., 2002, Tidal meanders: *Water Resources Research*, v. 38, 14 p. doi: 10.1029/2001WR000404.

Mariethoz, G., Comunian, A., Irarrazaval, I., and Renard, P., 2014, Analog-based meandering channel simulation: *Water Resources Research*, v. 50, p. 836-854, doi: 10.1002/2013WR013730.

Mariotti, G., and Fagherazzi, S., 2013, A two-point dynamic model for the coupled evolution of channels and tidal flats: *Journal of Geophysical Research–Earth Surface*, v. 118, p. 1387-1399. doi: 10.1002/jgrf.20070.

The MathWorks, Inc., 2014, `csaps` [Cubic smoothing spline] documentation: *MatLab Documentation Center Website*. Retrieved June 19, 2014, from http://www.mathworks.com/help/curvefit/csaps.html.

Matthes, G.H., 1941, Basic aspects of stream meanders: *American Geophysical Union Transactions*, v. 22, p. 632-636.

McAllister, M., and Snoeyink, J., 2000, Medial axis generalization of river networks: *Cartography and Geographic Information Science*, v. 27, p. 129-138. doi: 10.1559/152304000783547966.

Mikhailova, M.V., 2013, Processes of seawater intrusion into river mouths: *Water Resources*, v. 40, p. 483-498. doi: 10.1134/S0097807813050059.

Ministry of Irrigation, Water Development and Flood Control Flood Plan Coordination Organization, 1992, *Flood Action Plan 19, Technical Note 1: Bangladesh Transverse Mercator Projection*: Arlington, VA, Irrigation Support Project for Asia and the Near East, 3 p. Retrieved January 19, 2014, from http://www.cegisbd.com/pdf/.

Mirza, M.M.Q., 1997, Hydrological changes in the Ganges system in Bangladesh in the post-Farakka period: *Hydrological Sciences Journal*, v. 42, p. 613-631. doi: 10.1080/02626669709492062.

Mohammed, N.Z., Ghazi, A., and Mustafa, H.E., 2013, Positional accuracy testing of Google Earth: *International Journal of Multidisciplinary Sciences and Engineering*, v. 4, p. 6-9.

Morgan, J.P., and McIntire, W.G., 1959, Quaternary geology of the Bengal Basin, East Pakistan and India: *Geological Society of America Bulletin*, v. 70, p. 319-342. doi: 10.1130/0016-7606.

Mostafavi, M.A., Gold, C., and Dakowicz, M., 2003, Delete and insert operations in Voronoi/Delaunay methods and applications: *Computers and Geosciences*, v. 29, p. 523-530. doi: 10.1016/S0098-3004(03)00017-7.

Motta, D., Abad, J.D., Langendoen, E.J., and García, M.H., 2012a, The effects of floodplain soil heterogeneity on meander planform shape: *Water Resources Research*, v. 48, 17 p. doi: 10.1029/2011WR011601.

Motta, D., Abad, J.D., Langendoen, E.J., and Garcia, M.H., 2012b, A simplified 2D model for meander migration with physically-based bank evolution: *Geomorphology*, v. 163, p. 10-25. doi: 10.1016/j.geomorph.2011.06.036.

Movshovitz-Hadar, N., and Shmukler, A., 1998, River meandering and a mathematical model of this phenomenon: *Aleh, The Israel High-School Math Teacher Journal*, issue 25, 23 p. Retrieved July 28, 2014, from http://www.academia.edu/2619483/The_Mathematics_of_River_Meanders.

Myrick, R.M., and Leopold, L.B., 1963, *Hydraulic geometry of a small tidal estuary* (USGS Professional Paper 422-B), p. 12-18.

Nittrauer, J.A., Mohrig, D., Allison, M.A., and Peyret, A.P.B., 2011, The lowermost Mississippi River: A mixed bedrock-alluvial channel: *Sedimentology*, v. 58, p. 1914-1934. doi: 10.1111/j.1365-3091.2011.01245.x.

Nott, J.F., 2003, The urban geology of Darwin, Australia: *Quaternary International*, v. 103, p. 83-90. doi: 10.1016/S1040-6182(02)00143-X.

Novakowski, K.I., Torres, R., Gardner, R., and Voulgaris, G., 2004, Geomorphic analysis of tidal creek networks: *Water Resources Research*, v. 40, 13 p. doi: 10.1029/2003WR002722.

O'Brien, M.P., 1931, Estuary tidal prisms related to entrance areas: *Civil Engineering*, v. 1, p. 738-739.

Okabe, A., Boots, B., Sugihara, K., and Chiu, S.N., 2000, *Spatial Tessellations: Concepts and Applications of Voronoi Diagrams* (2nd ed.): New York, John Wiley I& Sons, Ltd., 671 p.

Parker, G., 2004, *1D Sediment Transport Dynamics with Applications to Rivers and Turbidity Currents* [eBook]. Retrieved March 4, 2014, from http://hydrolab.illinois.edu/people/parkerg//default.asp.

Parker, G., Diplas, P., and Akiyama, J., 1983, Meander bends of high amplitude: *Journal of Hydraulic Engineering*, v. 109, p. 1323-1337. doi: 10.1061/(ASCE)0733-9429(1983)109:10(1323).

Passalacqua, P., Lanzoni, S., Paola, C., and Rinaldo, A., 2013, Geomorphic signatures of deltaic processes and vegetation: The Ganges-Brahmaputra-Jamuna case study: *Journal of Geophysical Research: Earth Surface*, v. 118, 12 p. doi: 10.1002/jgrf.20128.

Pavelsky, T.M., and Smith, L.C., 2008, RivWidth: A software tool for the calculation of river widths from remotely sensed imagery: *IEEE Geoscience and Remote Sensing Letters*, v. 5, p. 70-73. doi: 10.1109/LGRS.2007.908305.

Persits, F.M., Wandrey, C.J., Milici, R.C., and Manwar, A., 2001, Geological map of Bangladesh: *U.S. Geological Survey Open File Report 97-470H*, scale 1:1,000,000.

Pestrong, R., 1965, The development of drainage patterns on tidal marshes: *Stanford University Publications—Geological Sciences*, v. 10, 87 p.

Petrovszki, J., Szekely, B., and Timar, G., 2012, A systematic overview of the coincidences of river sinuosity changes and tectonically active structures in the Pannonian Basin: *Global and Planetary Change*, v. 98-99, p. 109-121. doi: 10.1016/j.gloplacha.2012.08.005.

Pickering, J.L., Goodbred, S.L., Reitz, M.D., Hartzog, T.R., Mondal, D.R., and Hossain, M.S., in press, Late Quaternary sedimentary record and Holocene channel avulsions of the Jamuna and Old Brahmaputra River valleys in the upper Bengal delta plain: *Geomorphology*, 14 p. doi: 10.1016/j.geomorph.2013.09.021.

Pillsbury, G.B., 1939, *Tidal Hydraulics*: Washington, D.C., United States Government Printing Office, 283 p.

Quraishy, M.S., 1944, Origin of curves in rivers: *Current Science*, v. 13, p. 36-39.

Rahman, A.F., Dragoni, D., and El-Masri, B., 2011, Response of the Sundarbans coastline to sea level rise and decreased sediment flow: A remote sensing assessment: *Remote Sensing of Environment*, v. 115, p. 3121-3128. doi: 10.1016/j.rse.2011.06.019

Rahman, M.J.J., Faupl, P., and Alam, M.M., 2009, Depositional facies of the subsurface Neogene Surma Group in the Sylhet Trough of the Bengal Basin, Bangladesh: Record of tidal sedimentation: *International Journal of Earth Science*, v. 98, p. 1971-1980. doi: 10.1007/s00531-008-0347-7.

Redfield, A.C., 1965, Ontogeny of a salt marsh estuary: *Science*, v. 147, p. 50-55.

Reinsch, C.H., 1967, Smoothing by spline functions: *Numerische Mathematik*, v. 10, p. 177-183. doi: 10.1007/BF02162161.

Riley, S.J., 1972, A comparison of morphometric measures of bankfull: *Journal of Hydrology*, v. 17, p. 23-31. doi: 10.1016/0022-1694(72)90064-9.

Rinaldo, A., Fagherazzi, S., Lanzoni, S., Marani, M., and Dietrich, W.E., 1999, Tidal networks. 2. Watershed delineation and comparative network morphology: *Water Resources Research*, v. 35, p. 3905-3917. doi: 10.1029/1999WR900237.

Rodríguez, E., Morris, C.S., Belz, J.E., Chapin, E.C., Martin, J.M., Daffer, W., and Hansley, S., 2005, *An assessment of the SRTM topographic products, Technical Report JPL D-31639*: Pasadena, Jet Propulsion Laboratory, 143 p.

Rosensaft, M., 1995, A method for removing roughness on digitized lines: *Computers and Geosciences*, v. 21, p. 841-849. doi: 10.1016/0098-3004(95)00019-5.

Saalfeld, A., 1999, Topologically consistent line simplification with the Douglas-Peucker algorithm: *Cartography and Geographic Information Science*, v. 26, p. 7-18. doi: 10.1559/152304099782484901.

Salinas-Castillo, W.E., and Paredes-Hernández, C.U., 2013, Horizontal and vertical accuracy of Google Earth: Comment on 'Positional accuracy of the Google Earth terrain model derived from stratigraphic unconformities in the Big Bend region, Texas, USA' by

S.C. Benker, R.P. Langford and T.L. Pavlis: *Geocarto International*, n.v., 5 p. doi: 10.1080/10106049.2013.821176.

Sarker, M.H., and Thorne, C.R., 2006, Morphological response of the Brahmaputra-Padma-Lower Meghna river system to the Assam earthquake of 1950, *in* Sambrook Smith, G.H. (ed.), *Braided Rivers: Processes, Deposits, Ecology, and Management*: Oxford, Blackwell Publishers, p. 289-310.

Savenije, H.H.G., 2005, *Salinity and Tides in Alluvial Estuaries*: Amsterdam, Elsevier, 208 p.

Savitzky, A., and Golay, M.J.E., 1964, Smoothing and differentiation of data by simplified least squares procedures: *Analytical Chemistry*, v. 36, p. 1627-1639. doi: 10.1021/ac50214a047.

Schafer, R.W., 2011, What *is* a Savitzky-Golay Filter?: *IEEE Signal Processing Magazine*, v. 28, p. 111-117. doi: 10.1109/MSP.2011.941097.

Schumm, S.A., 1967, Meander wavelength of alluvial rivers: *Science*, v. 157, p. 1549-1550. doi: 10.1126/science.157.3796.1549.

Semeniuk, V., 1981, Long-term erosion of the tidal flats King Sound, northwestern Australia: *Marine Geology*, v. 43, p. 21-48. doi: 10.1016/0025-3327(81)90127-4.

Semeniuk, V., 1993, The Pilbara Coast: A riverine coastal plain in a tropical arid setting, northwestern Australia: *Sedimentary Geology*, v. 83, p. 235-256.

Shahid, S., and Khairulmaini, O.S., 2009, Spatio-temporal variability of rainfall over Bangladesh during the time period 1969-2003: *Asia-Pacific Journal of Atmospheric Sciences*, v. 45, p. 375-389.

Shaked, D., and Bruckstein, A.M., 1998, Pruning medial axes: *Computer Vision and Image Understanding*, v. 69, p. 156-169. doi: 10.1006/cviu.1997.0598.

Shaw, J.B., Wolinsky, M.A., Paola, C., and Voller, V.R., 2008, An imaged-based method for shoreline mapping on complex coasts: *Geophysical Research Letters*, v. 35, 5 p. doi: 10.1029/2008GL033963.

Shreve, R.L., 1974, Variation of mainstream length with basin area in river networks: *Water Resources Research*, v. 10, p. 1167-1177. doi: 10.1029/WR010i006p01167.

Shri, R.S., and Chugh, M.A., 1961, Tides in Hooghly River: *International Association of Scientific Hydrology Bulletin*, v. 6, p. 10-26.

Small, C., Steckler, M., Seeber, L., Akhter, S.H., Goodbred, S., Mia, B., and Imam, B., 2009, Spectroscopy of sediments in the Ganges-Brahmaputra delta: Spectral effects of moisture, grain size, and lithology: *Remote Sensing of Environment*, v. 113, p. 342-361. doi: 10.1016/j.rse.2008.10.009.

Smith, R.J., 2009, Use and misuse of reduced major axis for line-fitting: *American Journal of Physical Anthropology*, v. 140, p. 476-486. doi: 10.1002/ajpa.21090.

Snyder, J.P., 1987, *Map Projections—A Working Manual (U.S. Geological Survey Profes-*

sional Paper 1395): Washington, D.C., United States Government Printing Office, 383 p.

Solari, L., Seminara, G., Lanzoni, S., Marani, M., and Rinaldo, A., 2002, Sand bars in tidal channels, Part 2. Tidal meanders: *Journal of Fluid Mechanics*, v. 451, p. 203-238. doi: 10.1017/S0022112001006565.

Strahler, A.N., 1952, Hypsometric (area-altitude) analysis of erosional topography: *Geological Society of America Bulletin*, v. 63, p. 1117-1142.

Thakur, T.R., and Scheidegger, A.E., 1970, Chain model of river meanders: *Journal of Hydrology*, v. 12, p. 25-47. doi: 10.1016/0022-1694(70)90030-2.

U.S. Defense Mapping Agency, 1991, Raimangal River to Elephant Point: *United States of America Defense Mapping Agency Navigational Chart #63330*, 9th edition, scale 1:300,000.

U.S. Defense Mapping Agency, 1994, Devi River to Pusur River: *United States of America Defense Mapping Agency Navigational Chart #63320*, 8th edition, scale 1:300,000.

Urban, M.A., and Rhoads, B.L., 2003, Catastrophic human-induced change in stream-channel planform and geometry in an agricultural watershed, Illinois, USA: *Annals of the Association of American Geographers*, v. 93, p. 783-796. doi: 10.1111/j.1467-8306.2003.09304001.x.

Vignoli, G., 2004, *Modelling the morphodynamics of tidal channels*: Trento, Italy, University of Trento, Ph.D. dissertation, 153 p.

Vlaswinkel, B.M., and Cantelli, A., 2011, Geometrical characteristics and evolution of a tidal channel network in experimental setting: *Earth Surface Processes and Landforms*, v. 36, p. 739-752. doi: 10.1002/esp.2099.

Wahba, G., 1990, *Spline Models for Observational Data*: Philadelphia, Society for Industrial and Applied Mathematics, 161 p.

Whiting, P.J., and Dietrich, W.E., 1993, Experimental constraints on bar migration through bends: Implications for meander wavelength selection: *Water Resources Research*, v. 29, p. 1091-1102. doi: 10.1029/92WR02356.

Williams, G.P., 1978, Bank-full discharge of rivers: *Water Resources Research*, v. 14, p. 1141-1154. doi: 10.1029/WR014i006p01141.

Williams, G.P., 1986, River meanders and channel size: *Journal of Hydrology*, v. 88, p. 147-164. doi: 10.1016/0022-1694(86)90202-7.

Williams, P.B., Orr, M.K., and Garrity, N.J., 2002, Hydraulic geometry: A geomorphic design tool for tidal marsh channel evolution in wetland restoration projects: *Restoration Ecology*, v. 10, p. 577-590. doi: 10.1046/j.1526-100X.2002.t01-1-02035.x.

Wolanski, E., 2007, *Estuarine Ecohydrology*: Amsterdam, Elsevier, 168 p.

Woldenberg, M.J., 1972, Relations between Horton's Laws and hydraulic geometry as applied to tidal networks: *Harvard Papers in Theoretical Geography*, v. 45, p. 1-39.

Woodford, C.H., 1970, An algorithm for data smoothing using spline functions: *BIT Numerical Mathematics*, v. 10, p. 501-510. doi: 10.1007/BF01935569.

Zolezzi, G., and Güneralp, İ, in review, Wavelet-based characterization of dominant wavelength of meandering rivers: *Geophysical Research Letters*.

Zolezzi, G., and Seminara, G., 2001, Downstream and upstream influence in river meandering. Part 1. General theory and application to overdeepening: *Journal of Fluid Mechanics*, v. 438, p. 183-211. doi: 10.1017/S002211200100427X.

Appendices

Appendix A

Data summary tables

The channel names are primarily from Google Earth; channels in the Indian Sundarbans have been cross-referenced with the chart by the U.S. Defense Mapping Agency (1994) and the map in Chatterjee *et al.* (2013) whenever possible. Channels in the eastern portion of the delta have been cross-referenced with the chart by the U.S. Defense Mapping Agency (1991), but the chart displays names only for the largest channels. As Google Earth relies partly on crowdsourcing for the addition of place-names to the imagery, accuracy is not guaranteed. We also note that the channel numbers refer only to the order in which we digitized the channels and do not have any inherent meaning. Channels labeled as nonexistent are those channels that the author has not yet finished digitizing. Channel locations are given with reference to Figure A.1.

The "Type" column refers to our classification of the channel as tidal or fluvial. If the channel is tidal, we further classify it based on the position of the mouth, its directionality, and the presence of an upstream fluvial connection. The channel types are as follows:

- Type 1: Tidal channel, has direction, meets coast, has upstream connection
- Type 2: Tidal channel, has direction, doesn't meet coast, has upstream connection
- Type 3: Channel crosses between tidal and fluvial, or its nature is ambiguous. We did not include these channels in our analysis.

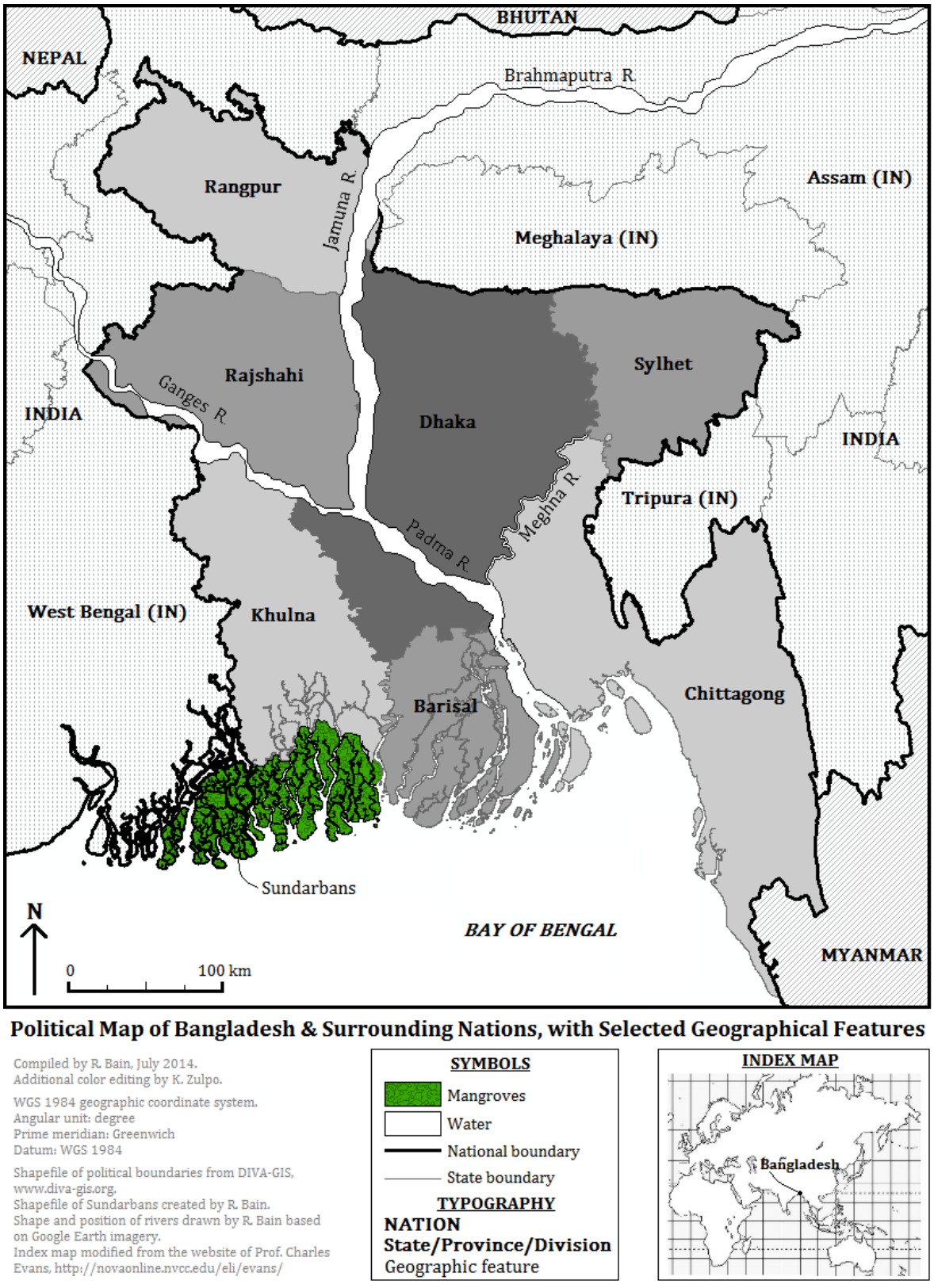

Figure A.1: *Map showing the geographical names of places referenced in the data summary table.*

- Type 4: Fluvial channel located south of Ganges River. These are generally distributary channels.
- Type 5: Tidal channel with no clear directionality
- Type 6: Fluvial channel located north of Ganges River (west of the Padma/Meghna confluence) or north of 23.5°N latitude (east of the Padma/Meghna confluence). These are generally tributaries of the larger rivers.
- Type 7: Tidal channel, has direction, meets coast, no upstream connection
- Type 8: Tidal channel, has direction, doesn't meet coast, no upstream connection

The column labeled W_{mean} gives the average width of the channel in meters. This provides an average sense of scale for the channel, but the reader should realize that a channel may vary greatly in width along its full length, particularly in the tidal case.

The "v-value" column refers to the value of v used to calculate the smoothing parameter p for the smoothing spline (see Section 3.4.4, paragraph 2).

The "Weights" column refers to the set of weights used to construct the weighted smoothing spline (see Section 3.4.6).

Table A.1: Summary of channels used in this study.

Channel #	**Channel name**	**Type**	W_{mean} **(m)**	v**-value**	**Weights**
1	Gona Estuary, Indian Sundarbans	1	780	-4.78	1,5,10,25
2	n/a, Bangladesh Sundarbans	1	620	-4.78	1,5,10,25
3	Gosaba Estuary, Indian Sundarbans	1	1910	-4	1,5,10,25
4+4A	Harinbhanga Estuary, Indian Sundarbans	1	2220	-4.78	1,5,10,25
4B	Ganral Estuary, Indian Sundarbans	2	770	-4.78	1,5,10,25
5	Raimangal Estuary, Bangladesh/India border (in Sundarbans)	1	2080	-4.78	1,5,10,25
6	n/a, Bangladesh Sundarbans	1	930	-4.78	1,5,25,50
7A	n/a, Bangladesh Sundarbans	2	290	-4.78	1,5,10,100
7+7B	Malancha River, Bangladesh Sundarbans	1	1010	-4.78	1,5,10,100
8	n/a, Indian Sundarbans	2	600	-4.78	1,5,10,25
9	Ichamati River, Bangladesh/ India border north of Sundarbans	2	540	-4.78	1,5,10,25
10	Bol River, Bangladesh Sundarbans	2	850	-4.78	1,5,10,25
11	n/a, Bangladesh Sundarbans	2	160	-4.78	1,5,10,25
12	n/a, Bangladesh Sundarbans	2	290	-4.78	1,5,10,25
13+13A	Betmar *Gang*[1], Bangladesh Sundarbans	1	600	-4.78	1,5,10,100
13B	Betmar Gang, Bangladesh Sundarbans	2	370	-4.78	1,5,10,25
14	Supoti *Khal*[2], Bangladesh Sundarbans	1	350	-5.78	1,50,100,250
15	Bhola River, Bangladesh Sundarbans	1	580	-5.78	1,50,100,250
16	Sela River, Bangladesh Sundarbans	2	600	-5	1,5,10,25
17+17A	n/a, Bangladesh Sundarbans	2	190	-4.78	1,5,10,25

Continued on next page

[1] *Gang* is the English transliteration of the Bengali word for *river*

[2] *Khal* is the English transliteration of the Bengali word for *canal*, although all of the "canals" we digitized appear to be natural.

Table A.1 – continued from previous page

Channel #	Channel name	Type	W_{mean} (m)	v-value	Weights
17B	n/a, Bangladesh Sundarbans	8	80	-5.78	1,5,50
18	n/a, Bangladesh Sundarbans	2	80	-5	1,50,100,250
19	Gorai River[3] (coast to Khulna), Bangladesh Sundarbans and Khulna Division, Bangladesh	1 and 3[4]	1130	-6 and -4.78	1,100,200,500
19A	Gorai River (north of Khulna), Khulna Division, Bangladesh	4		-4.08	
20+20A	Arpangasia River and Kholpetua River, Bangladesh Sundarbans	2	990	-4.78	1,5,10,25
20B	Kapatakkh River, Bangladesh Sundarbans	2	610	-4.78	1,5,10,25
21	n/a, Bangladesh Sundarbans	2	430	-4.78	1,5,25,125
22	n/a, Bangladesh Sundarbans	2	270	-4.78	1,5,25,50
23	n/a, Bangladesh Sundarbans	2	210	-4.78	1,5,10,25,50
Channel 24 does not exist.					
25	n/a, Bangladesh Sundarbans	2	90	-4.78	1,5,25,50
26	n/a, Bangladesh Sundarbans	2	200	-5.17	1,5,25,50
27	Balaswar River and Katcha River, Barisal Division, Bangladesh	1	2180	-4.78	1,5,10,50
27A	Kaliganga River, Barisal Division and Khulna Division, Bangladesh	3	3200	-4.78	1,5,10,25
27B	Sandha River, Barisal Division, Bangladesh	3	5600	-4.78	1,5,25
28	Bishkhali River, Barisal Division, Bangladesh	1	9790	-4.78	1,5,25,50
29	Baleswar River, Barisal Division,	1	1370	-4.78	1,5,10,25,50

Continued on next page

[3]The U.S. Defense Mapping Agency (1991) labels the coastal reach of the Gorai River as the Pussur River.
[4]The change in channel type occurs at inflection point #11.

Table A.1 – continued from previous page

Channel #	Channel name	Type	W_{mean} (m)	v-value	Weights
	Bangladesh				
30	Bighai River, Barisal Division, Bangladesh	3	280	-5.78	1,50,100,250,500
Channel 31 does not exist.					
32	Andarmanick River, Barisal Division, Bangladesh	1	600	-4.78	1,5,10,25,50
33	n/a, Bangladesh Sundarbans	2	220	-5	1,5,10,25,50
34	Rai River, Khulna Division, Bangladesh	2	330	-4.78	1,5,25,50
35	n/a, Bangladesh Sundarbans	2	60	-5.78	1,50,100,250,500
36	n/a, Bangladesh Sundarbans	2	360	-4.78	1,5,10,25,50
37	n/a, Bangladesh Sundarbans	2	140	-5.78	1,50,100,250,500
38	n/a, Bangladesh Sundarbans	5	90	-4.78	1,5,25,50
39	n/a, Bangladesh Sundarbans	2	100	-5	1,5,25,50
40	n/a, Bangladesh Sundarbans	1	230	-6.78	1,50,100,250,500
41	n/a, Bangladesh Sundarbans	2	100	-5.78	1,50,100,250,500
42	Hooghly River and Bhagitarhi River, West Bengal, India	3 and 4[5]	540	-5.78	1,50,100,250,500
43	Arial Khan River, Barisal Division, Bangladesh	4	380	-5.78	1,50,100,250,500
44	Kangsa River downstream of Jaria, Dhaka Division, Bangladesh	6	150	-5.78	1,5,100,200
44A	Kangsa River upstream of Jaria, Dhaka Division, Bangladesh	6	90	-5.78	1,5,100,200
45+45A	Surma River downstream of Kalaruka, Sylhet Division, Bangladesh	6	230	-5.78	1,5,10,100,200
45Aa	Surma River upstream of Kalaruka,	6	160	-5.08	1,5,100,200

Continued on next page

[5]The change in channel type occurs at inflection point #53.

Table A.1 – continued from previous page

Channel #	Channel name	Type	W_{mean} (m)	v-value	Weights
	Sylhet Division, Bangladesh				
45Ab	Goyain Nadi (Surma tributary), Sylhet Division, Bangladesh	6	120	-5.08	1,5,100,200
46	Bangali River, Rajshahi Division, Bangladesh	6	270	-4.78	1,5,25,50
Channel 47 does not exist.					
Channel 48 does not exist.					
49	Jalangi River, West Bengal, India	4	100	-5.78	1,5,100,200
50	n/a, Urirchar Island, Chittagong Division, Bangladesh	2	70	-4.78 and -3.78	1,5,25,50
51	n/a, Bangladesh Sundarbans	1	120	-3.78	1,5,25,50
52	n/a, Dublar Char, Bangladesh Sundarbans	1	50	-5.08	1,5,25,50
53	n/a, Bangladesh Sundarbans	8	30	-3.78	1,5,25,50
54	Kotka Khal, Bangladesh Sundarbans	1	160	-4.08	1,5,25,50
55	n/a, Bangladesh Sundarbans	2	30	-4.78	1,5,25,50
56	n/a, Bangladesh Sundarbans	2	70	-4.78	1,5,25,50
57	n/a, Bangladesh Sundarbans	5	80	-5.78	1,5,100,200
58	n/a, Bangladesh Sundarbans	2	130	-3.78	1,5,25,50
59	n/a, Bangladesh Sundarbans	8	40	-3.78	1,5,10,25,50
60	n/a, Bangladesh Sundarbans	5	50	-4.78	1,5,10,25,50
61	n/a, Bangladesh Sundarbans	8	40	-4.78	1,5,25,50
62	Betmar Gang upstream of Bara Showla Khal, Bangladesh Sundarbans	2	300	-4.78	1,5,50,100
63	n/a, Bangladesh Sundarbans	2	100	-3.78	1,5,10,100,200
64	Sutarkhali River, Bangladesh Sundarbans	2	230	-4.78	1,5,25,50
65	n/a, Bangladesh Sundarbans	8	180	-4.78	1,5,10,100,200
66	Kobadak River, Khulna Division,	3	230	-3.78	1,5,25,50

Continued on next page

Table A.1 – continued from previous page

Channel #	Channel name	Type	W_{mean} (m)	v-value	Weights
	Bangladesh				
67	n/a, Khulna Division, Bangladesh	2	400	-3.78	1,5,10,25,50
68	n/a, Khulna Division, Bangladesh	3	310	-3.78	1,5,10,25,50
69	n/a, Indian Sundarbans	2	170	-4.08	1,5,25,50
70	Kobadak River upstream of Paikgachha Bridge, Khulna Division, Bangladesh	3	210	-4.78	1,5,100,200
71	Datta River, West Bengal, India	2	610	-4.78	1,5,50,100
72	Dansa River, West Bengal, India	3	440	-3.78	1,5,10,25
73	Matla River, Indian Sundarbans	2	1500	-4.78	1,5,25,50
74	Saptamukhi Estuary, Indian Sundarbans	1	830	-3.78	1,5,10,25,50
75	n/a, West Bengal, India	1	550	-3.78	1,5,10,25,50
76	n/a, West Bengal, India	2	280	-3.78	1,5,25,50
77	Matla River, West Bengal, India	2	270	-4.78	1,5,25,50
78	n/a, West Bengal, India	2	290	-4.78	1,5,10,100,200
79	n/a, Indian Sundarbans	2	170	-4.78	1,5,100,200
80	n/a, Indian Sundarbans	8	2.5	-2.78	1,5,25,50
81	n/a, Indian Sundarbans	2	80	-3.78	1,5,25,50
82	n/a, Indian Sundarbans	8	20	-3.78	1,5,25,50
83	Bhangaduni River, Indian Sundarbans	1	620	-4.78	1,5,50,100
84	n/a, Indian Sundarbans	1	400	-4.78	1,5,25,50
85	n/a, Indian Sundarbans	5	70	-5.08	1,5,10,25,50
Channel 86 does not exist.					
87	n/a, Barisal Division, Bangladesh	3	70	-5.08	1,10,20,100,200
88	n/a, West Bengal, India	8	40	-3.78	1,10,25,50
89	n/a, West Bengal, India	8	30	-3.78	1,5,10,25,50
90	Kharibari Haroya Khal, West Bengal,	3	40	-3.78	1,5,10,25,50

Continued on next page

Table A.1 – continued from previous page

Channel #	Channel name	Type	W_{mean} (m)	v-value	Weights
	India				
91	n/a, Barisal Division, Bangladesh	2	160	-4.78	1,25,50,125,250
92	n/a, Barisal Division, Bangladesh	8	50	-4.78	1,10,25,125,250
93	Khasiakhali River, Khulna Division Bangladesh	3	360	-4.08	1,10,50,100
94	n/a, Indian Sundarbans	8	30	-3.78	1,5,10,25,50
95	Piyali River, West Bengal, India	8	100	-4.30	1,5,10,25,50
96	Mani River, West Bengal, India	8	130	-5.08	1,50,250,500
97	n/a, Barisal Division, Bangladesh	2	180	-4.78	$1{,}1 \times 10^3$,2×10^3, 5×10^3,1×10^4
98	n/a, Barisal Division, Bangladesh	2	60	-3.78	1,5,10,25,50
99	n/a, Bangladesh Sundarbans	8	30	-3.78	1,5,10,25,50
100	n/a, Indian Sundarbans	5	570	-4	1,10,25,50
101	Pitt's Creek, West Bengal, India	1	620	-3.78	1,5,25,50
102	n/a, West Bengal, India	8	6.7	-2.78	1,5,25,50
103	n/a, Indian Sundarbans	7	110	-3.78	1,5,10,25,50
104	n/a, Barisal Division, Bangladesh	8	3.5	-3.08	1,5,10,25,50
105	n/a, Barisal Division, Bangladesh	8	3.3	-3.08	1,5,10,25,50
106	n/a, Barisal Division, Bangladesh	8	2.3	-2.78	1,5,25,50
107	n/a, Barisal Division, Bangladesh	8	5.4	-2.78	1,5,10,25,50
108	n/a, Chittagong Division, Bangladesh	7	2.9	-2.78	1,5,10,25,50
109	n/a, Chittagong Division, Bangladesh	7	9.2	-2.78	1,5,25,50
110	n/a, Chittagong Division, Bangladesh	7	9.7	-3	1,5,25,50
111	n/a, Chittagong Division, Bangladesh	7	9.6	-2.78	1,5,10,25,50
112	n/a, Chittagong Division, Bangladesh	8	8.5	-2.78	1,5,25,50
113	n/a, Chittagong Division, Bangladesh	8	7.9	-2.78	1,5,25,50
114	n/a, Chittagong Division, Bangladesh	8	6.9	-2.78	1,5,10,25,50
115	n/a, Chittagong Division, Bangladesh	8	4.1	-2.78	1,5,10,25,50

Continued on next page

Table A.1 – continued from previous page

Channel #	Channel name	Type	W_{mean} (m)	v-value	Weights
116	n/a, Chittagong Division, Bangladesh	8	4.7	-2.78	1,5,10,25,50
117	n/a, Chittagong Division, Bangladesh	8	8.0	-2.78	1,5,10,25,50
118	n/a, Chittagong Division, Bangladesh	8	6.2	-2.78	1,5,10,25,50
119	n/a, Nizam Char, Barisal/Chittagong border	7	60	-2.78	1,5,10,25,50
120	n/a, Chittagong Division, Bangladesh	8	20	-3.78	1,5,10,25,50
121	n/a, Bangladesh Sundarbans	2	120	-4.78	1,5,10,25,50
122	Katakal River tributary, Tripura, India	6	30	-3.78	1,5,25
123	Amjur River tributary, Assam, India	6	11	-3.78	1,5,25
124	Madhura River, Assam, India	6	52	-3.78	1,5,25

Appendix B

Details on the sine-generated curve

The sine-generated curve was first introduced by Langbein and Leopold (1966) as a deterministic model for meander geometries. A sine-generated curve is frequently defined by its direction function

$$\theta = \omega \sin \frac{2\pi s}{L_f} \tag{B.1}$$

where θ is the angle the curve makes with the horizontal axis. Alternately, the curve can me represented by its curvature function:

$$\kappa(s) = \frac{d\theta}{ds} = \frac{2\pi\omega}{L_f} \cos \frac{2\pi s}{L_f}. \tag{B.2}$$

It is less common to see the equation of a sine-generated curve with respect to its x and y coordinates, but we find that this is an informative method for understanding the properties of the curve. Using basic trigonometry and integrating Equation B.1 (see Movshovitz-Hadar and Shmukler, 1998, for details), we obtain:

$$x(s) = \int_0^s \cos\theta(t)dt + K_1 = \int_0^s \cos\left(\omega \sin \frac{2\pi t}{L_f}\right) dt + K_1 \tag{B.3}$$

$$y(s) = \int_0^s \sin\theta(t)dt + K_2 = \int_0^s \sin\left(\omega \sin \frac{2\pi t}{L_f}\right) dt + K_2. \tag{B.4}$$

Note that the constants of integration K_1 and K_2 produce a rigid shift of the curve in the x and y directions, respectively, and do not change the inherent shape of the "channel". For simplicity, we will assume that $K_1 = K_2 = 0$.

Using simple formulae from elementary calculus, we can now verify several important properties of the sine-generated curve. We will first show that the curvature function is, indeed, given by Equation B.2. By the Fundamental Theorem of Calculus,

$$\frac{dx}{ds} = \cos\left(\omega\sin\frac{2\pi s}{L_f}\right) \qquad \text{and} \qquad \frac{dy}{ds} = \sin\left(\omega\sin\frac{2\pi s}{L_f}\right). \tag{B.5}$$

Taking the second derivatives with respect to s gives us

$$\frac{d^2x}{ds^2} = -\frac{2\pi\omega}{L_f}\sin\left(\omega\sin\frac{2\pi s}{L_f}\right)\cdot\cos\left(\frac{2\pi s}{L_f}\right) \tag{B.6}$$

$$\frac{d^2y}{ds^2} = \frac{2\pi\omega}{L_f}\cos\left(\omega\sin\frac{2\pi s}{L_f}\right)\cdot\cos\left(\frac{2\pi s}{L_f}\right). \tag{B.7}$$

Substituting the appropriate expressions into the curvature equation then gives us

$$\begin{aligned}
\kappa(s) &= \frac{\frac{dx}{ds}\frac{d^2y}{ds^2} - \frac{dy}{ds}\frac{d^2x}{ds^2}}{\left(\left(\frac{dx}{ds}\right)^2 + \left(\frac{dy}{ds}\right)^2\right)^{3/2}} \\
&= \frac{\frac{2\pi\omega}{L_f}\cos^2\left(\omega\sin\frac{2\pi s}{L_f}\right)\cdot\cos\left(\frac{2\pi s}{L_f}\right) + \frac{2\pi\omega}{L_f}\sin^2\left(\omega\sin\frac{2\pi s}{L_f}\right)\cdot\cos\left(\frac{2\pi s}{L_f}\right)}{\left(\cos^2\left(\omega\sin\frac{2\pi s}{L_f}\right) + \sin^2\left(\omega\sin\frac{2\pi s}{L_f}\right)\right)^{3/2}} \\
&= \frac{\frac{2\pi\omega}{L_f}\cos\left(\frac{2\pi s}{L_f}\right)\left[\cos^2\left(\omega\sin\frac{2\pi s}{L_f}\right) + \sin^2\left(\omega\sin\frac{2\pi s}{L_f}\right)\right]}{\left(\cos^2\left(\omega\sin\frac{2\pi s}{L_f}\right) + \sin^2\left(\omega\sin\frac{2\pi s}{L_f}\right)\right)^{3/2}}
\end{aligned}$$

which, due to the trigonometric identity $\sin^2\phi + \cos^2\phi = 1$, reduces to

$$\kappa(s) = \frac{2\pi\omega}{L_f}\cos\left(\frac{2\pi s}{L_f}\right). \tag{B.8}$$

We will now show that the sine-generated curve is parameterized with respect to arc length, rendering future complicated arc-length calculations unnecessary. The arc length

formula for a parametric curve is

$$\mathcal{L} = \int_a^b \sqrt{\left(\frac{dx}{ds}\right)^2 + \left(\frac{dy}{ds}\right)^2} ds. \tag{B.9}$$

Substituting from Equation B.5, we obtain:

$$\begin{aligned}
\mathcal{L} &= \int_a^b \sqrt{\left(\cos\left(\omega \sin \frac{2\pi s}{L_f}\right)\right)^2 + \left(\sin\left(\omega \sin \frac{2\pi s}{L_f}\right)\right)^2} ds \\
&= \int_a^b \sqrt{1} ds \\
&= s\Big|_a^b \\
&= b - a.
\end{aligned}$$

This demonstrates that the intrinsic parameter s in the sine-generated curve equations is simply equal to the arc length along the curve.

We can also apply the ideas presented above to more general cases. Suppose that we are given a curvature function $\kappa^*(s)$. Obtaining a plot of a function with these curvature values is a simple matter of integrating once (to obtain the direction function $\theta(s)$) and substituting the direction function into the equations for x and y (which amounts to a second integration). The function that we obtain will be unique up to a rigid motion (translation or rotation) in space as a consequence of the four constants of integration produced by integrating a set of two parametric equations two times, which we will ignore here. For example, suppose $\kappa^*(s) = s$. The direction function is then given by $\theta^*(s) = \frac{s^2}{2}$, and the equations for x and y are

$$x^*(s) = \int_0^s \cos\theta(t) dt = \int_0^s \cos\left(\frac{t^2}{2}\right) dt \tag{B.10}$$

$$y^*(s) = \int_0^s \sin\theta(t) dt = \int_0^s \sin\left(\frac{t^2}{2}\right) dt. \tag{B.11}$$

The curve is still conveniently parameterized with respect to arc length. Although Equations B.10 and B.11 cannot be solved analytically, it is not difficult to attain a numerical solution

in MATLAB. This was the method by which we obtained Figures 1.1 and 1.2.